UC Santa Barbara
UC Santa Barbara Electronic Theses and Dissertations

Title
Separation, Filtration, and Clogging of Dilute Suspensions in Confined Flows

Permalink
https://escholarship.org/uc/item/9ff5p096

Author
Dincau, Brian Michael

Publication Date
2022

Peer reviewed|Thesis/dissertation

eScholarship.org Powered by the California Digital Library
University of California

University of California
Santa Barbara

Separation, Filtration, and Clogging of Dilute Suspensions in Confined Flows

A dissertation submitted in partial satisfaction
of the requirements for the degree

Doctor of Philosophy
in
Mechanical Engineering

by

Brian Michael Dincau

Committee in charge:

Professor Emilie Dressaire, Co-Chair
Professor Alban Sauret, Co-Chair
Professor Arturo Keller
Professor Eckart Meiburg

June 2022

The Dissertation of Brian Michael Dincau is approved.

Professor Eckart Meiburg

Professor Arturo Keller

Professor Alban Sauret, Committee Co-Chair

Professor Emilie Dressaire, Committee Co-Chair

June 2022

Separation, Filtration, and Clogging of Dilute Suspensions in Confined Flows

Copyright © 2022

by

Brian Michael Dincau

Dedication

This thesis is dedicated to life-long holistic growth.

It's funny — as researchers we're often expected to continually pursue deeper and deeper knowledge within a specific field. However, I am not a fan of overspecialization. Humans posses incredible adaptability and are extremely efficient learners. It's one of the few ways in which we still remain functionally distinct from artificial intelligence. Not to mention, life's more fun when learning new things.

Similar to how many athletes cross train to in order to develop muscles and reflexes that their primary sport under-utilizes, healthy adults can cross-train their brain to develop new motor skills and logical pathways that literally transform how we perceive and navigate the world. This is the essence of learning. We are self-re-configurable, capable of continual growth and maturation. The skills and experiences we gain do not stand alone in a vacuum. Rather, they begin to overlap and reinforce each other as the lines blur, making it easier to learn new skills as we concurrently make sense of the world and the self.

Throughout my PhD, the following poem, originally a lyric from a favorite song, has helped to center my perspective and balance the opposing forces of acceptance and defiance:

A feeling we may never truly achieve or understand.
Always yearning for something that may not really exist,
Something you can't see,
You can't feel,
But when you find it,
You will know what it is, to truly feel complete.
In this ever changing world,
We are the ones who must adapt.
Like cogs in a continuous wheel within our own lives,
All with our own individual traits and identities which make us all unique.
We are hybrids.
Together we are strong,
We are the keys, the strings, the voices in our own heads,
But only by our actions can we really change,
And it's only by these actions that we can be defined as truly being instrumental.
So take a moment.
Reflect on every move, every decision,
And when you realize that calming sensation,
Even through the hurt and the pain,
And the fact that it can all be taken away in the blink of an eye.
That is the moment you realise,
You're in control.

- Andy Duguid, *C.H.I.C.*

Acknowledgements

There are many people that I wish to acknowledge as contributors to my growth and success throughout my PhD program at UCSB.

I thank my parents, Mike and Dorine, and my brother, Steven, for supporting me throughout this long journey. Quitting my well-paying job to return to school full-time was initially a very difficult decision. What if I made the wrong choice and simply set myself back in life? But their strength and pride helped reassure me that I was headed in the right direction.

I thank my inspiring partner Amanda, who has helped me learn to swim with the chaos, rather than against it.

I thank both of my advisors, Alban and Emilie, for taking me in as their first student at UCSB and always pushing me to achieve my potential.

I thank both Connor and Ethan, two undergraduate assistants who helped run experiments and process data for some of my projects. Their help was invaluable, especially with all of the complications that COVID brought to research.

I would also like to acknowledge the support I received from the UCSB Nanofab and the Microfluidics Lab at CNSI. I used their facilities to fabricate wafer molds and microfluidic devices which were essential in my research.

Finally, I thank all of the UCSB supporting staff and custodial services. This campus is a beautiful, inspiring, and functional space that remains so due to your hard work.

Curriculum Vitæ

Brian Michael Dincau

Education

2022	Ph.D. in Mechanical Engineering University of California, Santa Barbara
2018	M.S. in Mechanical Engineering Washington State University, Vancouver
2012	B.S. in Mechanical Engineering, Minor in Technology Management University of California, Davis

Primary Publications

BM Dincau, Y Lee, JH Kim, WH Yeo. Recent advances in nanoparticle concentration and their application in viral detection using integrated sensors. *Sensors*. 2017.

BM Dincau, A Aghilinejad, T Hammersley, X Chen, JH Kim. Deterministic lateral displacement (DLD) in the high Reynolds number regime: high-throughput and dynamic separation characteristics. *Microfluidics and Nanofluidics*. 2018.

BM Dincau, A Aghilinejad, X Chen, SY Moon, JH Kim. Vortex-free high-Reynolds deterministic lateral displacement (DLD) via airfoil pillars. *Microfluidics and Nanofluidics*. 2018.

BM Dincau, MZ Bazant, E Dressaire, A Sauret. Capillary sorting of particles by dip coating. *Physical Review Applied*. 2019.

BM Dincau, E Dressaire, A Sauret. Pulsatile flow in microfluidic systems. *Small*. 2020.

BM Dincau, E Mai, Q Magdelaine, JA Lee, MZ Bazant, A Sauret. Entrainment of particles during the withdrawal of a fibre from a dilute suspension. *Journal of Fluid Mechanics*. 2020

BM Dincau, C Tang, E Dressaire, A Sauret. Clog mitigation in a microfluidic array via pulsatile flows. *Soft Matter*. 2022.

Honors and Awards

Outstanding Teaching Assistant Award, Mechanical Engineering (UCSB 2022)
The 2nd Place Annual Student Speaker Award for ENGR 230 (UCSB 2020)
Lindau Laureate Meeting 2020 Nominee, University of California (UCSB 2019)
Best Teaching Assistant Award, Mechanical Engineering (UCSB 2019)
The 1st Place Award for Podium Presentation, Annual Research Showcase (WSU 2018)
Nanoengineering for Energy and Sustainability Poster Presentation Award (ASME 2017)
The 2nd Place Award for Podium Presentation, Annual Research Showcase (WSU 2017)
$7.5 Million Regional Sales Excellence Award (CaptiveAire 2016)
UC Regents Scholarship and Regent Scholars Honors Program (UC Davis 2008-2012)
Robert C Byrd Scholarship (UC Davis 2008-2012)
Engineering Deans List (UC Davis 2008-2012)
Meritorious Valedictorian (Quartz Hill High School 2008)
International Baccalaureate Diploma Recipient (Quartz Hill High School 2008)

Abstract

Separation, Filtration, and Clogging of Dilute Suspensions in Confined Flows

by

Brian Michael Dincau

Suspensions, whether natural or engineered, are encountered in nearly all physical systems involving flow. For various reasons, they are crucially important in manufacturing, water resource management, and medicine. As a result, many scientists are actively working to understand suspension flows. How do particles modify the flow? How can we separate the discrete and continuous phases? How do suspensions behave in complex or confined flows? In this thesis work, I address these questions using two different experimental platforms.

In the first half, I focus on capillary suspension flows, utilizing a dip coating platform. Dip-coating is a manufacturing technique used to apply thin films and specialized coatings to a variety of wares. When suspensions are involved, the thickness of the stagnation point below the dip-coating meniscus determines whether or not suspended particles will be entrained during the dip-coating process. For a planar substrate, we control this thickness by varying the dip-coating withdraw speed and viscosity of the suspension. Here, we extend this understanding to cylindrical substrates, and show that their curvature can be used as an additional parameter to control particle entertainment. We also demonstrate how to use these controls to separate large and small particles from a bidisperse suspension.

While dip-coating provides a low-maintenance clogging-free environment, due to it's lack of solid confinement, most other suspension systems do not posses this luxury. Indeed, clogging is a major challenge in many applications, ranging from pharmaceuticals

to irrigation, resulting in a growing desire for versatile and robust clog prevention techniques. Ideally these techniques should be preventative, rather than restorative, and should avoid changing the suspension itself. Thus, in the second half of this work, I probe the relationship between clogging and hydrodynamics, specifically how a pulsatile flow environment yields different clogging dynamics than a steady flow environment. I provide a primer on pulsatile flows in microfluidic systems, which highlights various applications of pulsatile flows as well as techniques for generating them. Then I present a study which systematically characterizes the mechanisms for clog mitigation in a pulsatile environment, which depend on both the pulsatile amplitude and frequency.

Contents

Chapter 1

Introduction

1.1 What is a Suspension?

A *suspension* is a heterogeneous mixture of two phases —a *continuous phase* and a *discrete phase*. The continuous phase is always a fluid, such as water or air, while the discrete phase is comprised of individual particles which are carried by the continuous phase. Generally, when describing a suspension, the discrete phase is named first, while the continuous phase is named second. For example, a dust storm could be described as a suspension of dust-in-air, while a mud slide could be described as a suspension of sediment-in-water.

In addition to solid particles, suspensions can also contain fluid particles as the discrete phase. One such example are suspensions of water droplets-in-air, which includes clouds and fog. An *emulsion* is a specific class of suspensions in which two immiscible fluids are combined, such as the oil-in-vinegar emulsions that serve as a base for many salad dressings. Given this broad classification, it becomes apparent that suspensions are found everywhere. Suspension flows comprised of sediment, water, and air shape the planet through erosion. Suspensions flow through us in the form of blood, comprised

of cells and large molecules suspended in plasma, which provides the necessary mechanisms for macroscopic animals to live and grow. Suspension flows can become incredibly complex, but for the remainder of this work, I will focus on the most-studied case of solid-in-liquid suspensions.

Due to their ubiquity, suspension flows have been a major topic of scientific interest for quite some time. A key parameter in describing any suspension is the volume fraction ϕ, which is defined as the (volume of the discrete phase) / (volume of the suspension) and ranges from $0 < \phi < 1$. Though in practice, $\phi_{max} \leq 0.7$, due to the maximum packing fraction of spherical particles. The volume fraction is critical for understanding how a suspension will flow. Equally important is the dynamic viscosity μ of the continuous phase. For low volume fraction suspensions ($\phi \leq 0.03$) the viscosity of the suspension is approximately equivalent to the viscosity of the continuous phase. As the volume fraction increases, so does the viscosity of the suspension [1]. For suspensions with $\phi \sim 0.5$, the suspension viscosity can become over ten times the viscosity of the continuous phase. As suspensions approach their maximum volume fraction, their viscosity rapidly approaches infinity and they lose their ability to flow.

In addition to modifying the viscosity of the continuous phase, the presence of particles can alter the viscous response of a suspension. Depending on the size, shape, and chemistry of the discrete phase, suspensions can be Newtonian or non-Newtonian. Newtonian fluids have a viscosity which is independent of the shear rate, while non-Newtonian fluids do not have a constant viscosity. This gives rise to complex suspensions, which can be shear-thinning, shear-thickening, or to even behave as solids until a minimum yield stress is reached [2]. Generally, all of these complexities can be mitigated with a sufficiently low volume fraction. Thus, for the remainder of this work, I focus on dilute suspensions with $\phi \leq 0.01$ having a Newtonian continuous phase.

Regardless of the volume fraction, suspensions can still behave in complicated ways

under the effects of confinement. For dilute suspensions of neutrally buoyant particles, their free-flow closely mirrors the flow of a pure liquid. However, when a suspension must pass through a small tube or other geometric constriction, the effects of heterogeneity become more apparent. For example, blood flowing through the heart and large blood vessels appears relatively homogeneous with an even dispersion of blood cells, which are about $6 - 8\,\mu$m in diameter. The flow profiles measured in large blood vessels are quite similar to the flow profile of a pure fluid with the equivalent properties. However, when blood flows through capillaries, which are $5 - 10\,\mu$m in diameter, the blood cells deform and line up in single-file, yielding a distinctly different flow profile than a pure fluid [3]. This is one result of confinement, which arises when the geometric lengthscale of a confinement, such as the diameter of a capillary, becomes comparable to the size of suspended particles, such as blood cells in this example.

For the first major section of this work, I focus on the *soft confinement* of a suspension by a capillary interface. I call it soft, because the confining geometry is a deformable liquid-air interface. Using a dip coating platform, I investigate how the flow of a suspension from a bulk reservoir into a thin film can result in separation of the discrete and continuous phases, similar to the reorganization of blood cells under confinement.

For the second section, I focus on the more traditional case of *hard confinement* commonly found in pipe flows or flows through porous media, in which the confining geometry is not deformable. In these experiments, I center the discussion around the phenomenon of clogging —when discrete particles stop flowing, due to confinement, and restrict the motion of the continuous phase.

Throughout this work, I reference my own published works as standalone sections that address the technical details of their corresponding topic (and my PhD overall). In between these works, I provide some conversational background and transitional information in order to understand how they are all related to one another.

1.2 Permissions and Attributions

1. The content of chapter 2.2 is the result of a collaboration with Alban Sauret, Ethan Mai, Quentin Magdelaine, Martin Bazant, and J. Alex Lee and has previously appeared in the *Journal of Fluid Mechanics*. DOI: https://doi.org/10.1017/jfm.2020.643

2. The content of chapter 2.3 is the result of a collaboration with Emilie Dressaire, Alban Sauret, and Ethan Mai and has previously appeared in *Physical Review Applied*. DOI: https://doi.org/10.1103/PhysRevApplied.12.011001

3. The content of chapter 3.1 is the result of a collaboration with Emilie Dressaire and Alban Sauret and is currently under review for publication in *Physics Today*.

4. The content of chapter 3.2 is the result of a collaboration with Emilie Dressaire and Alban Sauret and has previously appeared in *Small*.
   DOI: https://doi.org/10.1002/smll.201904032

5. The content of chapter 4.1 is the result of a collaboration with Emilie Dressaire, Alban Sauret, and Connor Tang and has previously appeared in *Soft Matter*. DOI: https://doi.org/10.1039/D2SM00013J

Chapter 2

Capillary Phase Separation via Dip Coating

2.1 Introduction to Dip Coating

Dip coating is a technique used to deposit thin films onto a substrate, dating as far back as $\sim$ 500 B.C. when this process was first used to repeatedly dip a wick into a reservoir of fat or wax to create candles. Today, dip coating is heavily used across a variety of industries, due to its combination of high-throughput potential, high repeatability, and low operating cost. Dip coating can be used to add functionality in the form of a coating, such as adding textured grip to a tool. In other applications, the coating itself is the final product when peeled off of the substrate, which is how latex and nitrile gloves are made.

During the dip coating process, the thickness of the coating film can be precisely controlled by the speed at which the substrate is withdrawn. This is a key aspect which showcases the versatility of dip coating. For very thin films, a slow withdraw is used. For thicker films, a faster withdraw or multiple coatings can be used.

This process becomes more complicated when the reservoir contains a suspension,

rather than a pure liquid, due to the confinement imposed at the dip coating meniscus. At slow enough withdraw speeds, the thickness of the coating film can be comparable to the average particles size in the suspension. If the coating film becomes too thin, then particles may remain in the bath without transferring to the substrate. This can be useful for some applications in which only a pure liquid coating is desired. On the other hand, this also implies that there is a minimum coating thickness for any given suspension, if both the discrete and continuous phase are desired in the coating at their original volume fraction.

This phenomenon of conditional particle entrainment has been investigated experimentally, analytically, and computationally for a flat substrate [4, 5, 6, 7]. In this case, there are three parameters which determine whether or not particles will be entrained: (1) The particle radius; (2) The capillary length of the suspension, which is a ratio of two forces: surface tension and gravitational acceleration; (3) The capillary number of the dip coating system, which is also a ratio of two forces: viscous drag and surface tension. To give context to these parameters, viscous drag is the force that pulls the suspension up with the substrate during the coating process. Gravitational acceleration is the force that pulls in the opposite direction, due to the weight of the suspension. Surface tension governs the curvature of the dip-coating meniscus, which is approximately where particles are either entrained or recirculated into the reservoir.

The next simplest geometry for a substrate, one which is commonly used but only recently studied with respect to particle entrainment, is a cylinder. For large cylindrical substrates with radii much larger than suspended particles, they behave like a flat plate. However, for thin cylinders or fibers with radii comparable to the size of suspended particles, an additional parameter must be considered: the Goucher number, which is a ratio of two lengthscales, the capillary length of the suspension (defined above) and the radius of the cylindrical substrate.

2.2 Particle Entrainment for Cylindrical Substrates

The following study provides detail to the brief summary presented above, in which the dependence on the fiber radius is systematically investigated through a series of experiments combined with numerical simulations. The study is comprised of 4 primary components:

1. First, the dependence of film thickness on fiber radius is investigated for a pure liquid. An explicit expression is derived, which agrees well with experimental measurements of film thickness when the Capillary number is small ($Ca << 1$) and the film thickness h remains much smaller than the substrate radius R ($h << R$).

2. With an understanding of the expected film thickness, we perform a series of experiments to determine the entrainment threshold for particles in a suspension, as a function of particle radius, substrate radius, withdraw velocity, and suspension viscosity. We find that as substrate radius increases, the entrainment threshold approaches that expected for a flat plate. However, for a small substrate radius, entrainment occurs at a much higher velocity when compared to a flat plate.

3. The next step in understanding this process is determining the thickness at the stagnation point, as well as the location of the stagnation point below the meniscus. This thickness is determined by solving for the surface velocity along the meniscus and finding the point at which this velocity vanishes to zero when applying the thin film limit $h << R$. At low Ca, the result is the same for a fiber as it is for a flat plate. The thickness at the stagnation point is approximately three times the thickness of the substrate coating, or $h^* \approx 3h$. The location of the stagnation point is determined through numerical simulation, and the resulting streamlines agree well with the thickness approximation above.

4. Finally, the threshold Capillary number for particle entertainment Ca^* is formalized as a function of the particle radius a, the substrate radius R, and the Goucher number Go. As Go$\rightarrow \infty$, *i.e.* the radius of the substrate is much larger than the capillary length of the suspension, the resulting threshold agrees well with previous cases for a flat plate. As Go$\rightarrow 0$, *i.e.* the radius of the substrate is much smaller than the capillary length of the suspensions, we obtain the new expression in which the threshold capillary number follows a simple power law function of the particle radius:

$$Ca^* = 0.645 \left[\frac{\alpha\, a}{3\, R}\right]^{3/2}. \tag{2.1}$$

2.2.1 Abstract

A fiber withdrawn from a bath of a dilute particulate suspension exhibits different coating regimes depending on the physical properties of the fluid, the withdrawal speed, the particle sizes, and the radius of the fiber. Our experiments indicate that only the liquid without particles is entrained for thin coating films. Beyond a threshold capillary number, the fiber is coated by a liquid film with entrained particles. We systematically characterize the role of the capillary number, the particle size, and the fiber radius on the threshold speed for particle entrainment. We discuss the boundary between these two regimes and show that the thickness of the liquid film at the stagnation point controls the entrainment process. The radius of the fiber provides a new degree of control in capillary filtering, allowing greater control over the size of the particles entrained in the film.

2.2.2 Introduction

Many industrial processes involve coating a substrate with a liquid film [6, 8]. Dip coating is a common method, where a substrate is withdrawn from a liquid bath at a controlled velocity U to deposit a thin layer of liquid of thickness h [9, 10]. For a Newtonian liquid of dynamic viscosity μ, density ρ and surface tension γ, the entrainment of the liquid film is governed by the balance between viscous and capillary forces, whose ratio is measured by the capillary number $\mathrm{Ca} = \mu U/\gamma$. In the 2D situation, where a plate is withdrawn from a liquid bath, [11] and [12] derived an expression for the film thickness for capillary number $\mathrm{Ca} < 10^{-2}$, $h = 0.94\,\ell_c\,\mathrm{Ca}^{2/3}$, where h is the thickness of the coating film and $\ell_c = \sqrt{\gamma/(\rho\,g)}$ is the capillary length.

Although most studies of dip coating have considered homogeneous fluids, various processes involve thin-film of suspensions containing particles. In industrial processes, this situation is involved in coating slurries on fibers for manufacturing of particle coated fiber

additives and fabrics [13, 14, 15, 16], *e.g.* containing optical coatings or "smart" particles or devices, but also for functional or smart fabrics and flexible detection/transmission devices, and as an alternate approach to achieve "multi-material fibers" [17]. Besides, dip coating can also be used for the filtration and sorting of particles [18]. In some situations, the particle size becomes comparable to the thickness of the liquid film, and interfacial effects occur. While the effective viscosity $\mu(\phi)$ of a suspension, where ϕ denotes the volume fraction, can be obtained with classical rheological approaches [19, 20, 21], interfacial effects can lead to unexpected observations, where the effective bulk rheology of the suspension fails to capture the flow dynamics. For instance, the presence of particles modify the pinch-off of suspension drops [22, 23], the quasi-static break-up of a liquid bridge [24, 25, 26], the stability of jets [27, 28, 29], the fragmentation processes of particle-laden thin films [30], but also the contact line dynamics [31]. Besides, during the dip-coating of a plate the presence of particles leads to different coating regimes [32, 33, 7, 4]. For non-Brownian particles, at small capillary numbers corresponding to thin films, only the liquid is entrained while the particles remain trapped in the liquid bath. When the withdrawal velocity satisfies $U > U^*$, where U^* corresponds to the velocity threshold for individual particle entrainment, isolated particles are observed in the liquid film. This regime corresponds to capillary number Ca larger than $Ca^* \simeq 0.24(a/\ell_c)^{3/4}$, for a plate, where a denotes the particle radius. For intermediate capillary numbers, which depends on the volume fraction of the suspension and the withdrawal length, clusters form in the meniscus before being entrained on the plate [5]. A fundamental feature of dip coating flows is the presence of a stagnation point S^*, which separates the flow in two regions: a region that continues into the coating film, and a recirculation flow region into the liquid bath [see Fig. 2.1(a)]. On a flat plate, the thickness of the liquid film at the stagnation point of the dynamic meniscus, h^*, controls the entrainment of wetted particles [33]. Furthermore, recent experiments on a 2D plate have demonstrated that individual

particles are entrained if the radius of the particle a satisfies the condition $\alpha\, a \leq h^*$, where α is a prefactor ($\alpha \simeq 1.1 \pm 0.1$) accounts for the complex shape of the meniscus around the particle. The existence of the different regimes have led to a new method of capillary filtration [18]. Yet, this filtration is limited by the threshold for entrainment, which can only be controlled through the capillary length and the capillary number for planar substrate, thus limiting the range of particle sizes that can be filtered.

In this paper, we demonstrate that this limitation can be overcome by modifying the geometry of the substrate. Indeed, dip-coating with fibers exhibits a new length scale: the radius of the fiber, $R < \ell_c$. The relevant parameter in this situation thus becomes the Goucher number $\mathrm{Go} = R/\ell_c$, which compares the ratio of the vertical curvature, set by ℓ_c, and the azimuthal curvature set by the radius of the fiber R [34]. Note that one could also use the Bond number Bo defined as $\mathrm{Bo} = \mathrm{Go}^{1/2}$. For $Go \ll 1$, the thickness of the film is no longer governed by the capillary length ℓ_c but by the radius of the fiber only [35, 9]. We aim to describe how the particle entrainment threshold is modified by the cylindrical geometry. We consider experimentally a fiber withdrawn from a dilute particulate suspension. We begin by describing our experimental approach in Section 2. We then characterize the coating thickness in Section 3, where we highlight the role of the fiber geometry. Particle entrainment is characterized in Section 4, where we propose a theoretical explanation based on the thickness of the liquid film at the stagnation point, which controls the entrainment of particles in the coating film. Our theoretical model captures the experimental data and predicts the particle entrainment threshold for fiber substrates.

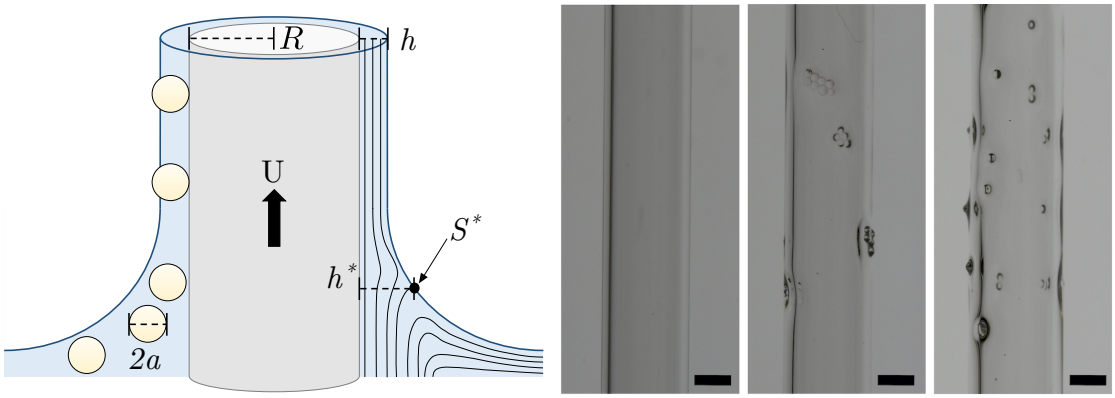

Figure 2.1: (a) Sketch of the experimental set-up. A fiber of radius R is withdrawn from a suspension of particles of diameter $2\,a$ at a velocity U. (b) Examples of images obtained after the withdrawal of a fiber of radius $R = 1.2\,\text{mm}$ from a suspension of $250\,\mu\text{m}$ particles dispersed in AP 100. The velocity U increases from left to right, which highlight three regimes: (i) no particle entrainment at low velocity, (ii) cluster entrainment just above the threshold, and (iii) mostly single particle entrainment well above the threshold. Scale bars are 1 mm.

2.2.3 Experimental methods

The experimental setup is shown in Fig. 2.1(a). It consists of withdrawing a glass fiber (Vitrocom) of radius $R \in [125,\, 1200]\,\mu\text{m}$ at a velocity $U \in [0.01,\, 10]\,\text{mm}\,\text{s}^{-1}$ from a bath of liquid containing a dilute suspension of spherical non-Brownian particles. The fiber is mounted in a fixed position to avoid any vibrations that would modify the film thickness, while a reservoir sits on a motorized linear translation stage (NRT150/M with a BSC201 controller, Thorlabs) beneath the fiber. The withdrawal dynamics are recorded using a digital camera (Nikon D7200) with a macro lens (AF-S VR Micro-Nikkor 200 mm f/4 lens). The fiber is back-lit with an LED panel (Phlox) mounted behind the container.

The suspensions are comprised of polystyrene particles (PS - Micro-Beads, Dynoseeds) of radius $a = [20,\, 40,\, 70,\, 125,\, 250]\,\mu\text{m}$ and density $\rho_p = 1056 \pm 2\,\text{kg}\,\text{m}^{-3}$. The particles are dispersed in a Newtonian fluid by mechanical stirring, ensuring a homogeneous suspension. We consider three different silicone oils : AP 100, AR 200 and AP 1000 (Sigma-Aldrich). The physical properties of these fluids have been measured in a previous study

[7]. The different silicone oils are of respective viscosity $\mu_{\mathrm{AP100}} = 0.132\,\mathrm{Pa}\cdot\mathrm{s}$, $\mu_{\mathrm{AR200}} = 0.243\,\mathrm{Pa}\cdot\mathrm{s}$ and $\mu_{\mathrm{AP1000}} = 1.42\,\mathrm{Pa}\cdot\mathrm{s}$ (measured with an Anton Paar MCR 501 rheometer and a plate/plate geometry) and density $\rho_{\mathrm{AP100}} = 1062\,\mathrm{kg.m^{-3}}$, $\rho_{\mathrm{AR200}} = 1046\,\mathrm{kg.m^{-3}}$ and $\rho_{\mathrm{AP1000}} = 1087\,\mathrm{kg.m^{-3}}$ (measured with glass densimeters from VWR), at 20°C. The interfacial tension of the silicone oils used in this study is $\gamma = 21 \pm 1\,\mathrm{mN.m^{-1}}$ [7]. The volume fraction of the suspension, defined as the volume of particles V_p divided by the total volume $V_{tot} = V_p + V_f$ is denoted $\phi = V_p/V_{tot}$ and remains smaller than 0.25% in all the experiments such that the viscosity of the dilute suspension is equal to the viscosity of the interstitial fluid at first order in the volume fraction ϕ and the particles can be considered as isolated. Indeed, for volume fraction $\phi \leq 0.25\%$, the viscosity of the suspension can be obtained using the first linear correction in volume fraction to the viscosity $\mu(\phi) = \mu_0\,(1 + 5\phi/2)$, where μ_0 is the viscosity of the interstitial fluid [21]. In the present case, the maximum difference in viscosity is for the $250\,\mu$m particles and is equal to 0.63%. Between two experiments the suspension was thoroughly mixed and over the timescale of an experiment. The densities are matched within 3% to reduce sedimentation. For all practical purposes the suspensions can be considered as neutrally buoyant as confirmed by our observation over the timescale of an experiment, typically between a few seconds to a few minutes [5].

To determine the entrainment threshold of particles, we start the experiment with a low withdrawal velocity U, where no particles are entrained in the meniscus and only liquid coats the fiber, [left picture in Fig. 2.1(b)] while stirring in between each trial. We then increase the withdrawal speed incrementally until we observe the first particles coating the fibers [middle picture in Fig. 2.1(b)]. As we are working at a small volume fraction ϕ, there is limited formation of clusters of particles. Further, from the velocity threshold U^*, we observe that the number of particles entrained increases with increasing the velocity [right picture in Fig. 2.1(b)]. The particle entrainment threshold is deter-

mined as the average of the last withdrawal speed where no particles are entrained and the first withdrawal speed where individual particles are entrained. The uncertainty on the estimate is the difference between these two velocities.

2.2.4 Liquid film thickness

Before considering the entrainment of particles, we first analyze the particle-free liquid film thickness entrained on withdrawn fibers. The thickness of the film coating a fiber withdrawn from a liquid bath has been less considered than the 2D configuration, *i.e.* a plate [10]. The main difference associated with the cylindrical geometry is that the film thickness now depends on the ratio between the fiber radius R and the capillary length ℓ_c, captured through the Goucher number $\mathrm{Go} = R/\ell_c$. We performed systematic experiments measuring the entrained film thickness versus withdrawal speed varying the fiber radius (Fig. 2.2a) and viscosity (Fig. 2.2b). Thanks to the cylindrical geometry, the film thickness can be determined by direct visualization of the edge of the fiber coated by the liquid. The processing is performed with ImageJ and a custom-made Matlab code.

Fig. 2.2(a) shows that the film thickness increases both with the capillary number and the fiber radius (fiber radii correspond to $\mathrm{Go} = 0.09$, 0.19 and 0.42). Both Fig. 2.2(a) and (b) show that the the capillary number dependence is captured by the well-known power law $h/R \propto \mathrm{Ca}^{2/3}$. The fiber radius R on the left hand side of this expression approximates the meniscus curvature far from the fiber where viscous effects become negligible, and is more generally expressed in terms of the static matching curvature κ_∞. [11] first showed that by matching the flowing film curvature, in the lubrication approximation, to the limiting static curvature κ_∞ results in the well-known relation

$$h\,\kappa_\infty = 1.34\,\mathrm{Ca}^{2/3}. \tag{2.2}$$

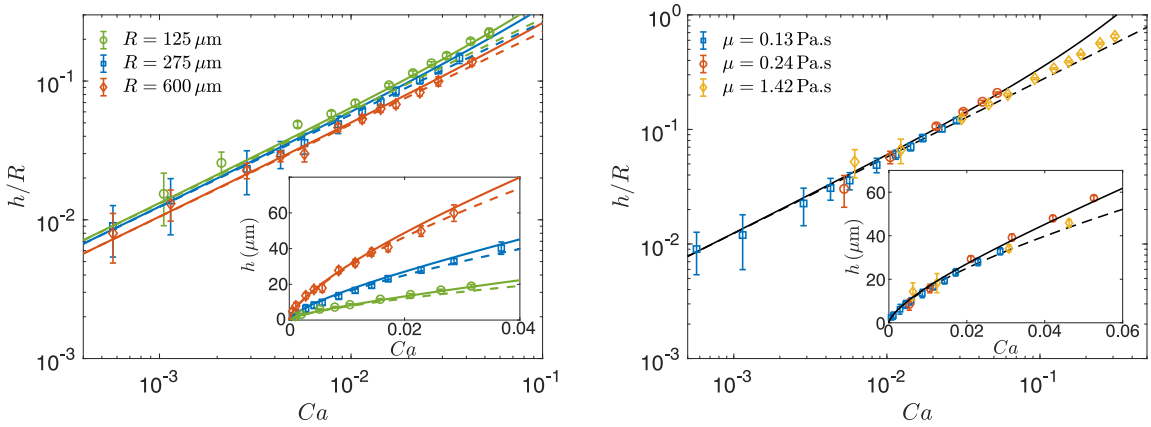

Figure 2.2: Dimensionless liquid film thickness h/R with (a) AP100 silicone oil ($\mu = 0.132\,\text{Pa}\cdot\text{s}$) and different fiber radii R corresponding to Go = 0.09, 0.19 and 0.42; (b) fiber radius $R = 275\,\mu$m (Go = 0.19) and different silicone oils. In both figures, the insets report the liquid film thickness h, the symbols are the experimental measurements, the solid lines are the corresponding theoretical predictions given by the implicit system of equations 2.4(a)-(b), and the dashed lines show the explicit expression provided by Eq. (2.6).

More specifically, [11] proposed to solve the meniscus drag out problem by breaking the meniscus into 3 regions: fully developed, transition, and static. In the fully developed region they argued that the film profile is exponential (solving equations in the appropriate limit), so the curvature is also exponential. In the static region they argued the curvature is that of a static meniscus, and approximated it to be constant, i.e., the curvature is parabolic. In the transition region, they numerically integrated the lubrication equations from the exponential boundary condition at the fully developed boundary up to far enough away to match the constant condition. Thus, the matching curvature is the presumed curvature of the meniscus when it is nearly static. [36] later showed the same result in cylindrical geometry where the static curvature is set by the radius, in the context of long slender bubbles in tubes. For fiber withdrawal and entrainment, the approximation $\kappa_\infty = 1/R$ is valid in the limits of very thin fibers, where the azimuthal curvature dominates over the planar curvature, Go $<<$ 1, and thin films where the film

surface radius is small compared to fiber radius, $h << R$. This last condition is sometimes less precisely expressed as $\mathrm{Ca} << 1$, and thus for vanishingly thin films entrained on vanishingly small fibers the coating thickness is $h/R \approx 1.34\mathrm{Ca}^{2/3}$ [9].

[35] attempted to account for the planar curvature and non-vanishing film thickness, ultimately developing a semi-empirical expression for the matching curvature

$$\kappa_\infty \approx \frac{1}{\ell_c}\left[\frac{\sqrt{2}}{2\,\mathrm{Go}\,s_0} + \frac{1.79\,(\mathrm{Go}\,s_0)^{0.85}}{1+1.79\,(\mathrm{Go}\,s_0)^{0.85}}\right] \tag{2.3}$$

where $s_0 = 1 + h/R$. Note that the limit $s_0 \to 1$ corresponds to $h \ll R$. In the limit of infinite radius $\mathrm{Go} \to \infty$, the expression clearly reduces to the flat plate curvature $\kappa_\infty \to 1/\ell_c$. In the opposite limit, the curvature expression reduces not to the fiber radius itself, but the radius of the fully developed entrained film $h + R$; the further limit of thin films ($s_0 \to 1$) clearly leads to $\kappa_\infty \to 1/R$.

Eq. 2.3 and Eq. 2.2 together result in the implicit relation between the dimensionless film thickness and capillary and Goucher numbers:

$$\frac{h}{R} = 1 + \frac{T\,\mathrm{Ca}^{1/2}}{\mathrm{Go}}, \tag{2.4a}$$

$$\text{and} \quad T = 0.944\,\mathrm{Ca}^{1/6}\left[\frac{1.79\,\mathrm{Go}^{0.85}\,(h/R)^{0.85}}{1+1.79\,\mathrm{Go}^{0.85}\,(h/R)^{0.85}} + \frac{0.71}{\mathrm{Go}\,(h/R)}\right]^{-1}. \tag{2.4b}$$

Resolution of this system leads to the solid curves in Fig. 2.2, which compare favorably with all experiments as it captures all the important trends: with respect to the capillary number Ca and with respect to the Goucher number Go. Fig. 2.2(b) shows that the predictions of Eq. 2.4(a)-(b) (solid curve) departs from the simple power law dependence (dashed line) at moderate values of capillary number, reflecting departure from the thin film limit. The small discrepancy in the film thickness could also be due to the drainage of the film as observed for 2D plate [37]. For small capillary number and within uncertainty,

the experiments do not exhibit a departure from the simple power law (dashed line) that Eqs. (2.4) exhibits, suggesting that some simpler limit may suffice to describe them. Retaining the finite Goucher number dependence but invoking the thin film limit ($s_0 \to 1$) in Eq. 2.3 results in the simplified matching curvature expression:

$$\kappa_\infty \approx \frac{\sqrt{2}}{\ell_c}\left[\frac{\sqrt{2}}{2\,\mathrm{Go}} + \frac{1.79\,\mathrm{Go}^{0.85}}{1+1.79\,\mathrm{Go}^{0.85}}\right]. \tag{2.5}$$

In this limit, Eq. 2.4 affords explicit expression of the dimensionless film thickness h/R in terms of the capillary number and Goucher number:

$$\frac{h}{R} = \frac{1.34\,\mathrm{Ca}^{2/3}}{1+2.53\,\mathrm{Go}^{1.85}/[1+1.79\,\mathrm{Go}^{0.85}]}. \tag{2.6}$$

In particular, Eq. 2.6 retains the simple power law dependence on Ca while accounting for finite fiber radius. Its predictions are represented by the dashed curves in Fig. 2.2, which appear to capture both of the relevant dependences in capillary and Goucher numbers while retaining a convenient simplicity. Therefore, the forthcoming analysis of particle entrainment will be based on Eq. 2.6.

2.2.5 Experimental results

We perform a systematic study varying the particle radius a, the fiber radius R, and the viscosity of the interstitial fluid μ. Here the capillary length is of the same order for all silicone oils considered and equal to $\ell_c \simeq 1.4\,\mathrm{mm}$. Examples of experimental observations are reported in Fig. 2.3. For a given fiber and particle radii, there is a threshold velocity U^* below which only a liquid film coats the fiber, and the particles remain trapped in the liquid bath. Beyond this threshold, particles start to cover the fiber. Therefore, three regimes are observed, similar to the 2D situation with the withdrawal

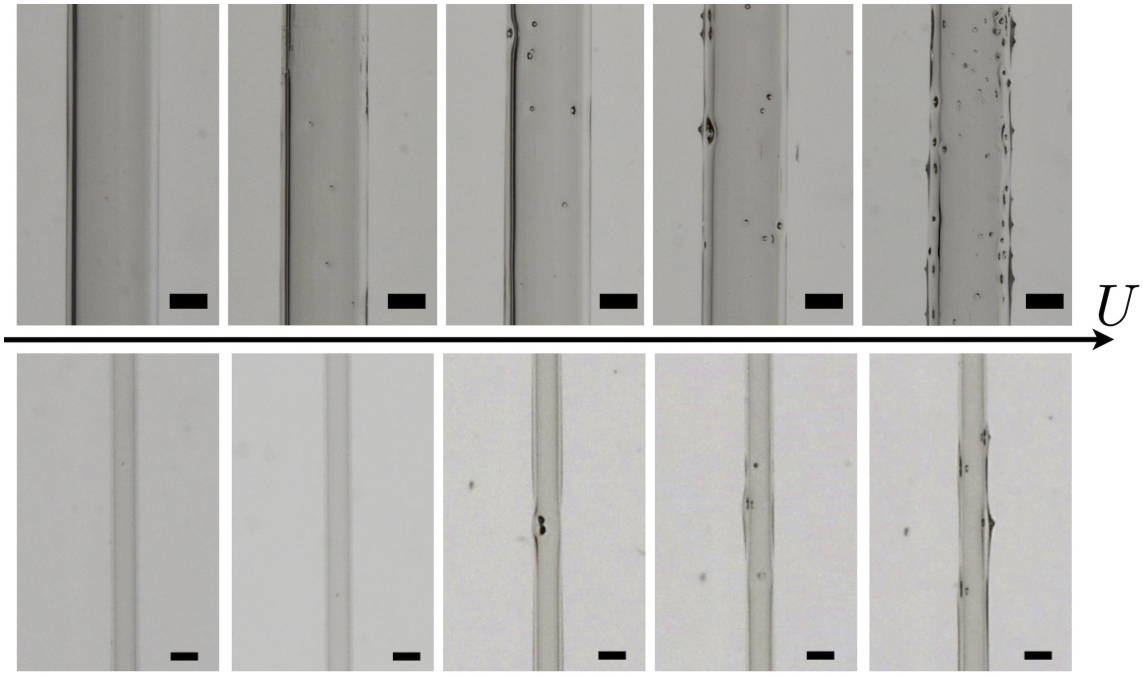

Figure 2.3: Examples of fibers after their withdrawal from a suspension. Top pictures: $a = 70\,\mu$m particles dispersed in AP 100, for a fiber of radius $R = 1.2\,$mm and increasing velocities $U = 0.5$, 1, 3, 5, $7\,\mathrm{mm\,s^{-1}}$ (from left to right). Scale bars are 1 mm. Bottom pictures: $a = 70\,\mu$m particles dispersed in AP 1000 for a fiber of radius $R = 0.55\,$mm and increasing velocities of $U = 1$, 2, 3, 4, $5\,\mathrm{mm\,s^{-1}}$. Scale bars are $500\,\mu$m.

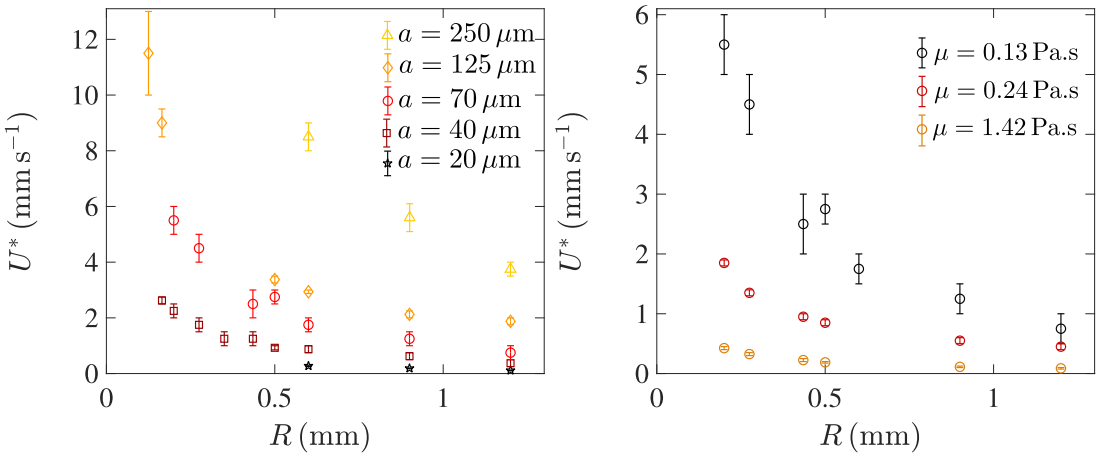

Figure 2.4: Withdrawal velocity threshold U^* for particle entrainement in the coating film as a function of the radius of the fiber R for various (a) particle radii a dispersed in the silicone oil AP 100 and (b) different viscosity of the interstitial fluid for particles of radius $a = 70\,\mu$m dispersed in silicone oils.

of a plate [5]: a coating film (i) without particles as shown in the left picture in Fig. 2.1(b), (ii) with clusters of particles formed in the meniscus and entrained in the coating film, visible on the middle picture in Fig. 2.1(b) and (iii) with individual particles as reported in the right picture in Fig. 2.1(b). The different regimes are clearly visible in Fig. 2.1(b) where the volume fraction is slightly higher that what we considered for the systematic measurements of the entrainment threshold. As shown by [5], the entrainment of clusters depends on the probability of forming a cluster of large enough size in the meniscus, whereas the entrainment of individual particles only requires that they be in close enough proximity to the fiber and overcome the resistive capillary force induced by the air-liquid meniscus. Therefore, at very small volume fraction, the range of existence of the cluster regime is very limited and make it easier to estimate the entrainment threshold. For this reason, we consider only dilute suspensions in this work making it easier to focus on the threshold velocity U^* for isolated particle entrainment.

The entrainment threshold U^* increases with the radius of the particles a for a given fiber diameter and is not influenced by inertial effects. Indeed, the maximum value

of the Reynolds number, defined as $\mathrm{Re} = \rho\, h\, U/\mu$, is obtained for the thicker films corresponding to $\rho \simeq 1060\,\mathrm{kg.m^{-3}}$, $h \sim 50\,\mu\mathrm{m}$, $U \sim 10^{-2}\,\mathrm{m.s^{-1}}$ and $\mu = 0.132\,\mathrm{Pa}\cdot\mathrm{s}$, and satisfies $Re < 10^{-2}$. We can thus consider that we are always in a viscous regime where $\mathrm{Re} \ll 1$. The threshold is directly related to the thickness of the coating fluid on the fiber, which increases with the speed of withdrawal. Therefore, the entrainment of larger particles on a fiber of radius R requires a larger withdrawal speed. The experimental trend observed here for the influence of the particle size is similar to the trend reported for 2D plates [5].

The main difference brought by the cylindrical geometry is that the particle entrainment threshold not only depends on the size of the particles a and the viscosity of the interstitial fluid μ but also on the radius of the fiber R. For fibers of different radii and the same interstitial fluid and particle size, Fig. 2.4(a) illustrates that the entrainment of particles does not occur at the same threshold velocity. The entrainment of particles in the liquid film occurs at a larger withdrawal speed for the smaller fibers. Therefore, the influence of the fiber radius provides a new degree of control of the entrainment threshold. We should also emphasize that when the diameter of the particle $2\,a$ becomes of the same order than the radius of the fiber R, the entrainment of particles will be difficult to achieve. Indeed, a coating film of the order of the particle radius would require much higher capillary number in this regime and our model for the coating film thickness would not be valid anymore.

The influence of the viscosity is similar to the 2D situation, as illustrated in Fig. 2.4(b). Higher fluid viscosity is associated with larger capillary numbers, $\mathrm{Ca} = \mu\, U/\gamma$. For a constant withdrawal velocity and a fixed surface tension, the coating film thickness thus increases with the viscosity, and the entrainment threshold increases when decreasing the viscosity of the fluid at a fixed R.

Our experiments demonstrate that the larger the size of the fiber, the smaller the

particle entrainment threshold. This effect can only be explained by considering the dependence of the film thickness on the fiber radius.

2.2.6 Stagnation point

The thickness at the stagnation point, h^* (see Fig. 2.1), has been derived in the 2D situation, *i.e.*, for a plate exiting a liquid bath [33] but has not been reported in the fiber configuration to the best of our knowledge.

We consider the withdrawal of a fiber of radius $R \ll \ell_c$. We use the cylindrical coordinates r and z (radial and along the axis of the fiber) and denote p the pressure and $\boldsymbol{u} = (u_r, u_\theta, u_z)$ the fluid velocity in these coordinates. In our experimental situation, we do not have surfactants, which could otherwise modify the interfacial tension and introduce Marangoni effects [38]. Zero normal velocity and zero normal and tangential stress balance boundary conditions need to be satisfied at the air-liquid interface, at $r = R + h(z)$. At the surface of the fiber, the no-slip boundary condition is $u_z(r = R) = 0$. Dip coating dynamics on a substrate lead to thin film, we thus use the standard lubrication equations. The velocity in the direction normal to the fiber u_r is negligible compared to the velocity along the fiber u_z. The pressure p is obtained from the Laplace equation in the axisymmetric meniscus. We define the position of the free surface of the liquid film as $\xi(z) = R + h(z)$. The pressure in the thin film approximation ($\mathrm{d}_z\xi \ll 1$) is $p = \gamma\,[1/\xi - \mathrm{d}^2\xi/\mathrm{d}z^2]$. Using the boundary conditions, we obtain the velocity field:

$$\frac{u_z}{U} = 1 - \frac{1}{4\,\mathrm{Ca}}\left(\frac{\mathrm{d}^3\xi}{\mathrm{d}z^3} + \frac{1}{\xi^2}\,\frac{\mathrm{d}\xi}{\mathrm{d}z}\right)\left[r^2 - R^2 - 2\,\xi^2 \ln\left(\frac{r}{R}\right)\right]. \tag{2.7}$$

The corresponding flow rate Q is constant and given by

$$\frac{Q}{U\,\pi\,R^2} = \left(\frac{\xi^2}{R^2} - 1\right) - \frac{R^2}{\mathrm{Ca}}\left(\frac{\mathrm{d}^3\xi}{\mathrm{d}z^3} + \frac{1}{\xi^2}\,\frac{\mathrm{d}\xi}{\mathrm{d}z}\right)\mathcal{F}\left(\frac{\xi}{R}\right), \tag{2.8}$$

where the function $\mathcal{F}(x)$ is defined as $\mathcal{F}(x) = 1/8 + 3\,x^4/8 - x^2/2 - x^4\ln(x)/2$. The stagnation point S^* corresponds to the location of the interface where the surface velocity vanishes. The expression of the surface velocity is obtained from Eq. (2.7) evaluated at $r = \xi$. Since the thickness of the liquid film $h(z)$ is much smaller than the radius of the fiber, $h/R \ll 1$, the surface velocity u_s, corresponding to the velocity tangential at the interface, is given by

$$\frac{u_s(z)}{U} = 1 + \frac{h^2}{2\,\mathrm{Ca}}\left(\frac{\mathrm{d}^3 h}{\mathrm{d}z^3} + \frac{1}{R^2}\,\frac{\mathrm{d}h}{\mathrm{d}z}\right). \tag{2.9}$$

The second term of this equation can be simplified by using the flow rate far from the meniscus, $Q_\infty = 2\,\pi\,U\,h\,R$. Using this expression with Eq. (2.8) allows us to simplify the expression (2.9) for the surface velocity:

$$\frac{u_s}{U} = 1 - \frac{h^2\left({\xi_\infty}^2 - \xi^2\right)}{2\,R^4\,\mathcal{F}(\xi/R)}. \tag{2.10}$$

Therefore, in the limit $h/R \ll 1$, the thickness at the stagnation point, *i.e.*, where the surface velocity vanishes, is equal to $h^* = 3\,h$. The value obtained for a fiber is thus the same as the value obtained for a 2D plate for $Ca \ll 1$ [33].

2.2.7 Numerical simulation: coating thickness and stagnation point

The comparison of this calculation to experiments is challenging as it requires visualizing the streamlines in a very narrow region. We thus rely on numerical simulations to determine the position of the stagnation point. The numerical simulations are performed with the Basilisk open-source library [1], successor of Gerris [39], using an adaptive mesh and a volume-of-fluid method to describe the two phases, liquid and air, and their

[1] www.basilisk.fr

interface. We solve the unsteady Stokes equation with a homogenous surface tension, assuming the problem to be axisymmetric and the fluids to be incompressible and Newtonian. The ratio of density and viscosity between the two phases are respectively fixed to 100 and 44.6. The surface tension and the gravity acceleration are implemented with the continuum surface force (CSF) method, as described for example by [40]. For this implementation of the gravity acceleration, the hydrostatic pressure is analytically subtracted to the mechanical pressure, leading to an effective pressure and reducing the gravity to a surface force. The numerical domain is a square, whose expansion is chosen to be around three times the capillary length. It includes part of the bath from which the fiber is redrawn. On the left side, we assume a no-slip condition of the fluids on the fiber, by imposing a homogeneous Dirichlet condition for the normal velocity and a Dirichlet condition equal to the velocity of the fiber for the tangential component. Free flow boundary conditions are assumed on the three other boundaries. Thanks to the reduced gravity formulation, these conditions are easily obtained, applying a homogeneous Dirichlet condition for the effective pressure and a homogeneous Neumann condition for the velocity field. The time step is determined by the CourantFriedrichsLewy condition conditions [40]. The simulation is initialized with a thin film on fiber linked to the bath by a meniscus. The simulation is stopped after the fiber has browsed two or three times the height of the numerical domain.

Numerically, the streamlines exhibit a clear stagnation point, as illustrated by the example in Fig. 2.5(a). The stagnation point is obtained by estimating the location where the surface velocity vanishes. At this location, the streamlines define the transition between the fluid that continues into the coating film, and the liquid that recirculates in the liquid bath. We report the evolution of the film thickness far from the meniscus h and the thickness at the stagnation point h^* for fibers associated with different Goucher numbers, Go = 0.032, 0.1, 0.5, in Fig. 2.5(b). The results of the numerical simulations

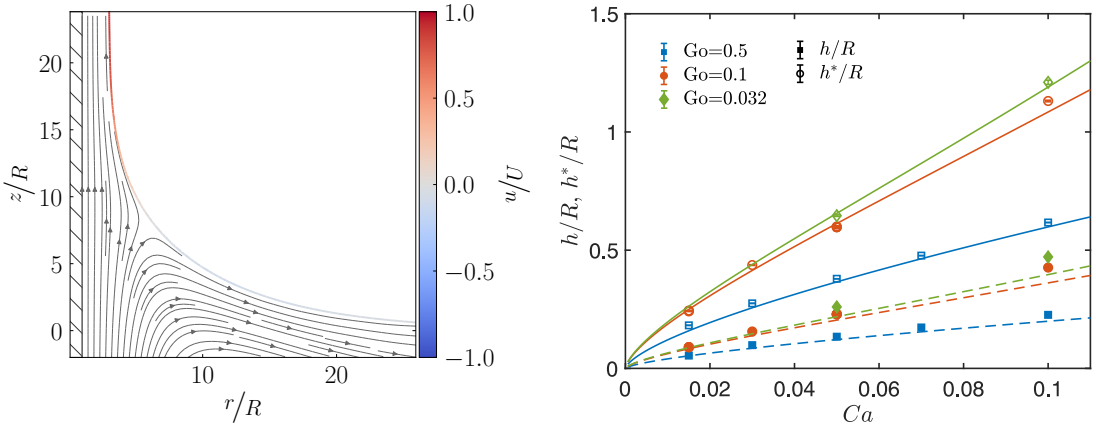

Figure 2.5: Numerical simulation of the dip coating of a fiber. (a) Examples of streamlines observed around the meniscus. The color bar indicates the dimensionless surface velocity. The stagnation point corresponds to the point where this surface velocity vanishes. (b) Evolution of the rescaled film thickness h/R (filled symbols) and the rescaled thickness at the stagnation point h^*/R (open symbols) for different values of the Goucher number Go. The dashed lines correspond to the theoretical expressions of the thickness given by Eq. (2.6) and the solid lines to the theoretical thickness at the stagnation point, $h^*/R = 3\,h/R$.

agree well (within 10%) with the theoretical prediction of the thickness at the stagnation point $h^*/R = 3\,h/R$ for a capillary number smaller than $\mathrm{Ca} < 10^{-1}$.

2.2.8 Threshold for particles entrainment

For a particle to be entrained in the coating film, the thickness at the stagnation point h^* must be larger than a fraction of the particle diameter $2\,a$, so that the viscous drag exerted on the particle overcomes the capillary resistance. The presence of the particle of the same size as the thickness at the stagnation point h^* will disturb the flow. Nevertheless, comparing h^* and the size of the particle have been shown to predict satisfactorily well the entrainment threshold [33, 5] and a similar criterion is used here. This criterion is expressed as:

$$\alpha\, a \leq h^* \quad \text{where} \quad 0 < \alpha \leq 2. \tag{2.11}$$

Experiments performed with spherical particles entrained on a 2D plate indicate that the prefactor α accounts for the complex shape of the meniscus around the particle, and reported $\alpha \simeq 1.1 \pm 0.1$. Such results are expected to hold for fibers in the limit of particle radii much smaller than the fiber radius, $a/R \ll 1$, since locally the particle sees the coating film as flat. But as the pure liquid film thickness analysis showed, the finite fiber radius must still be considered when estimating the fully developed film thickness around the fiber, and thus the thickness at the stagnation point.

We have demonstrated analytically in section 2.2.6 and confirmed through numerical simulation in section 2.2.7 that a sufficient estimate for the stagnation point thickness is $h^* = 3\,h$. From this expression of h^*, together with the criterion of Eq. (2.11) leads to a critical condition on the fully developed film thickness $h = \alpha a/3$. This film thickness can be inserted into either Eqs. (2.4) or Eq. (2.6) to obtain a relationship between particle's size a and the threshold capillary number Ca^* for entraining it.

The relationship according to the thin film limit (Eq. 2.6) is

$$\frac{\alpha\, a}{3\, R} = \frac{1.34\mathrm{Ca}^{*2/3}}{1 + 2.53\,\mathrm{Go}^{1.85}/\left[1 + 1.79\,\mathrm{Go}^{0.85}\right]}, \tag{2.12}$$

where a/R is the ratio of the particle to fiber radius. Re-arranging for the capillary number leads to:

$$\mathrm{Ca}^* \simeq 0.645 \left[\frac{\alpha\, a}{3\, R}\left(1 + \frac{2.53\,\mathrm{Go}^{1.85}}{1 + 1.79\,\mathrm{Go}^{0.85}}\right)\right]^{3/2}, \tag{2.13}$$

In the limit of vanishing Goucher number, the threshold capillary number follows a simple power law in the particle size:

$$\mathrm{Ca}^* = 0.645 \left[\frac{\alpha\, a}{3\, R}\right]^{3/2}. \tag{2.14}$$

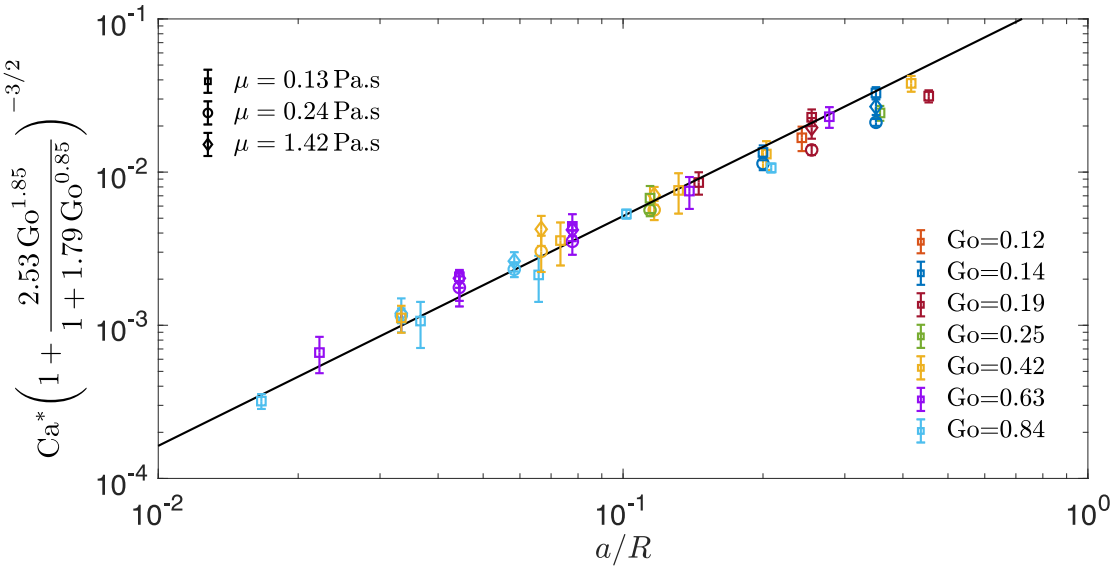

Figure 2.6: Capillary number threshold Ca^* for particles entrainement as a function of the ratio a/R for a fiber of various radii $R \in [165,\ 1200]\,\mu$m leading to Goucher number $\mathrm{Go} \in [0.12,\ 0.84]$. The solid line is the expression (2.13). The experimental results are obtained for various particle radii $a = 20\,\mu$m, $40\,\mu$m, $70\,\mu$m, $125\,\mu$m, $250\,\mu$m and viscosity of the interstitial fluid.

The Goucher number dependence and particle size depdence in Eq. (2.13) are separable such that the threshold capillary number can be rescaled by the Goucher number dependence to follow the single power law on the right hand side of Eq. (2.14).

In Fig. 2.6, we have reported the experimental results for different fiber radii, particle radii, and viscosities. The results are expressed in terms of the threshold capillary number rescaled by the term containing the Goucher number dependence to emphasize that all the data are indeed described well by the simple power law dependence $(a/R)^{3/2}$.

The solid line in Fig. 2.6 is the power law on the right hand side of (2.14) with a "best fit" value of $\alpha \sim 1.1$, which agrees well with the value obtained for a plate, $\alpha \simeq 1.1 \pm 0.1$ [5]. This agreement suggests that the criterion of Eq. (2.11) holds despite moderately large particles, *i.e.* for particle to fiber aspect ratio a/R of order 0.1, and that the influence of the cylindrical geometry of the fiber is well characterized by our approach.

In particular, the limit of Eq. (2.13) as Go $\to \infty$ reduces after some simplification to $\mathrm{Ca}^* \simeq 0.26\,(a/\ell_c)^{3/2}$, which is in agreement with previous experiments performed with a flat plate [5]. [35] emphasized that the large cylinders or flat plates regime is obtained for Goucher number Go > 3. According to equation (2.6), Go > 3 means that the azimuthal curvature contributes less than 5% deviation from the planar curvature. Therefore the expression proposed in this manuscript should be used for fibers of radius $R < 3\,\ell_c$, which corresponds to $R \sim 4.2\,\mathrm{mm}$ for the fluids considered here.

We note finally that the full finite film thickness expression of Eq. (2.4) can also be inverted for an explicit form in threshold capillary number in cases where the thin film approximation is not appropriate.

2.2.9 Conclusion

In this paper, we have characterized the entrainment of particles when withdrawing a fiber from a dilute suspension. We have shown that particles remain trapped in the liquid bath at small capillary numbers due to the capillary force exerted by the meniscus. At larger capillary numbers, individual particles can flow through the stagnation point and are entrained in the liquid film. We demonstrated that there is a strong dependence between this threshold capillary number and the fiber radius.

The results are rationalized by calculating the thickness of the film at the stagnation point for fibers. This thickness is related to the thickness of the liquid film through a prefactor $k = 3$. Using this result, and the thickness of the coating film for various Goucher number, the experimental data can be rescaled. We can, therefore, predict whether particles will be entrained in the coating film depending on the Goucher number $\mathrm{Go} = R/\ell_c$ and the capillary number Ca. Unlike the 2D situation with a plate, in which only the withdrawal rate affects the coating thickness and particle entrainment, the fiber

radius provides a new level of control and an additional design criterion for dip coating applications, in particular for size-based particle sorting [18].

2.3 Selective Separation: Dip Coating as Filtration Platform

The previous study reveals that the substrate radius is an important parameter for controlling particle entrainment when the substrate radius is comparable to or smaller than the capillary length of the suspension. This next study demonstrates a new application of dip coating: size-based separation of bidisperse suspensions. The study is comprised of two primary components:

1. First, we prepare suspensions of silicon oil and monodisperse polystyrene particles to verify the entrainment threshold for a variety of particle sizes. We do this by controlling the withdraw velocity of a planar substrate while noting the lowest velocity at which particles are entrained.

2. Next we prepare bidisperse suspensions containing two different particle sizes. We carefully choose withdraw velocities which result in entrainment of the smaller particles while leaving the larger particles in the bath, effectively filtering the suspensions by leveraging capillary confinement at the meniscus.

3. We provide evidence of high separation efficiency, and note that this technique works best for bidisperse particles having a size ratio of at least 2.5. For particle combinations with a smaller size ratio, separation becomes less efficient and requires extremely fine control of the withdraw velocity.

2.3.1 Abstract

In this Letter, we describe the capillary sorting of particles by size based on dip coating. A substrate withdrawn from a liquid bath entrains a coating whose thickness depends on the withdrawal speed and liquid properties. If the coating material contains particles, they will only be entrained when the viscous force pulling them with the substrate overcomes the opposing capillary force at the deformable meniscus. This force threshold occurs at different liquid thickness for particles of different sizes. Here, we show that this difference can be used to separate small particles from a mixed suspension through capillary filtration. In a bidisperse suspension, we observe three distinct filtration regimes. At low Capillary numbers, Ca, no particles are entrained in the liquid coating. At high Ca, all particle sizes are entrained. For a range of capillary numbers between these two extremes, only the smallest particles are entrained while the larger ones remain in the reservoir. We explain how this technique can be applied to polydisperse suspension. We also provide an estimate of the range of Capillary number to separate particles of given sizes. Combining this technique with the scalability and robustness of dip-coating makes it a promising candidate for high-throughput separation or purification of industrial and biomedical suspensions.

2.3.2 Introduction

Suspensions of particles are common throughout industrial, geophysical, and biomedical materials [41, 42, 20]. These disciplines all share a demand for scalable size-based particle separation techniques [43, 44], which can be utilized for high-volume sample analysis, preparation of highly uniform suspensions, or purification [45]. Different techniques that use particle, flow, and geometry interactions have been developed to achieve separation [46, 47]. A conventional method is direct filtration through a semi-permeable filter

or membrane [48]. This has the disadvantage of periodic filter replacement [49]. Numerous inertial microfluidic techniques have emerged, which can separate particles based on size without relying on replaceable filters, but still suffer from a relatively low per-unit throughput, with maximum reported values on the order of mL/min [50, 51, 52]. This combined with their susceptibility to clogging [53, 54, 55, 56, 57, 58, 59] has made scalability a significant challenge for microfluidic separation techniques. Different techniques that use external fields to further influence particle motion have also been developed [60, 61, 62, 63]. Despite their potential for improved efficiency, these techniques are more complicated to scale-up, and their reliance on external fields necessitates that they are system-specific, limiting the variety of suspensions they can process.

Recent work in filtration has resulted in the development of soft filtration techniques, which use a liquid interface as a tunable filter. This has been demonstrated using the liquid film on a moving bubble [64], and with free-standing liquid surfaces [65], but neither of these techniques possess the scalability required for large-scale applications. Froth floatation is a three phase separation process based on the manipulation of the difference in hydrophobicity of suspended solids. While highly scalable, this technique cannot differentiate particles based on size [66].

In this work, we introduce a new technique for size-based particle separation using a dip coating system. We show that the competition between viscous forces and surface tension at the meniscus can serve as a tunable dynamic filter, giving rise to a clog-free separation technique with promising scalability.

Dip coating is a process through which the withdrawal of a substrate from a liquid reservoir is used to deposit a uniform liquid coating [11, 12, 10]. The thickness of the coating h depends on the withdrawal speed U, the fluid viscosity η and the surface tension γ. These three parameters are combined in the Capillary number $Ca = \eta U/\gamma$, which describes the ratio of viscous to capillary forces. The coating thickness is given by

$h = 0.94\,\ell_c\,Ca^{2/3}$ according to the Landau-Levich-Derjaguin (LLD) prediction for small Ca, where $\ell_c = \sqrt{\gamma/(\rho\,g)}$ is the capillary length [11, 12]. When dip coating is used for a continuous-sheet substrate, the coating process can run indefinitely so long as the reservoir is replenished [6, 9]. This combination of scalability and robustness have made dip coating a popular technique which is appealing for filtration applications [6].

Recent results have shown that particle entrainment in dip coating of suspensions only occurs above a threshold velocity [33, 67, 7, 5]. This is due to a competition of forces at the meniscus, which forms where the substrate meets the liquid-air interface. The viscous force during withdrawal acts to pull particles with the substrate, while the capillary force opposes the deformation of the meniscus and prevents large particles from entering the coating film. Both of these forces depend on the particle size, but at different rates, resulting in a unique entrainment threshold for each size. In this paper, we demonstrate that this force balance can be leveraged to design a capillary filter, in which careful selection of the capillary number results in the filtration of smaller particles, while leaving larger particles in the reservoir. We experimentally investigate this new filtration approach and demonstrate its feasibility in separating particles from a bidisperse suspension.

2.3.3 Results and Discussion

To study how capillary filtration can be used to separate particles based on size, we work with the experimental setup illustrated in Fig. 2.7, which consists of a glass plate mounted in a fixed position above a suspension of silicone oil (AP100, Sigma Aldrich, density $\rho = 1058\,\mathrm{kg.m^{-3}}$, dynamic viscosity $\eta = 0.132\,\mathrm{Pa.s}$, surface tension $\gamma = 21\ \mathrm{mN.m^{-1}}$ at 20°C) and polystyrene microparticles (Dynoseeds, density $\rho_P \simeq 1055\,\mathrm{kg.m^{-3}}$) with diameters $2\,a = [88, 140, 240]\,\mu$m. Silicone oil provides complete wettability of the par-

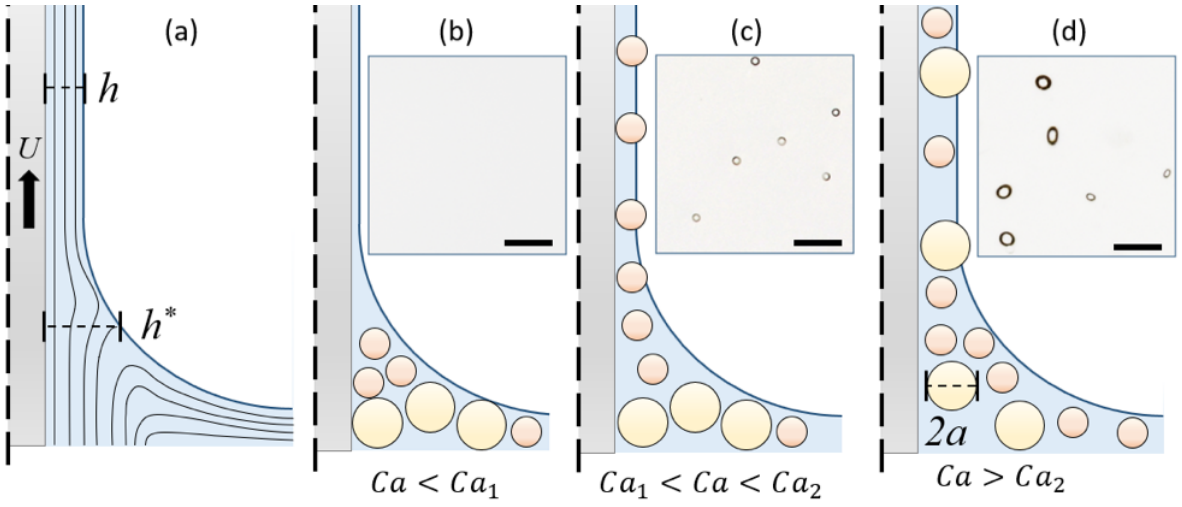

Figure 2.7: (a) Qualitative fluid streamlines, with the withdrawal speed U, film thickness h, and stagnation thickness h^*. (b)-(d) Three coating regimes for a bidisperse suspension. (b) At low Ca, no particles are entrained. (c) At intermediate Ca, only the small particles are entrained. (d) At high Ca, both small and large particles are entrained. Insets: examples of entrained films in each regime. Scale bars are 500 μm.

ticles and substrate, however it has been demonstrated that substrate wettability has little effect on the particle entrainment threshold [4]. The particles are neutrally buoyant over the time scale of an experiment. The reservoir is mounted on a movable stage controlled by a linear motor (ThorLabs NRT150). The volume fraction of the suspensions $\phi = V_p/V_T$, defined as the volume of particles V_p divided by the total volume $V_T = V_p + V_f$, is maintained at $\phi \leq 1\%$. Each trial involves a substrate withdrawal at a velocity $0.05\,\mathrm{mm.s^{-1}} < U < 1\,\mathrm{mm.s^{-1}}$. A camera (Nikon D7200) with 200 mm macro lens is used to photograph the plate after withdrawal.

During withdrawal, the plate is coated with a liquid layer of thickness $h = 0.94\,\ell_c\,Ca^{2/3}$. The thickness at the stagnation point h^* in the meniscus is given by $h^*/\ell_c = 3\,(h^*/\ell_c) - (h^*/\ell_c)^3/Ca$ and limits the size of particles that can enter the film [33, 5]. In a sense, the meniscus acts as a deformable filter, which excludes particles that are too large to pass. Therefore, tuning Ca controls the size threshold for particle entrainment. With our setup, we vary Ca by controlling the withdrawal speed U, which in turns influences

the stagnation thickness h^* and determines the maximum particle size entrained. With increasing Ca, we note qualitatively three distinct coating regimes for a bidisperse suspension. At low Ca, no particles are entrained [Fig. 2.7(b)]. For high Ca, both particle sizes are entrained [Fig. 2.7(d)]. For Ca values between these two, only the smaller particles are entrained [Fig. 2.7(c)], we note this to be the capillary filtration regime. In the following, we use our experimental setup to characterize the filtration regime first by studying monodisperse suspensions, and then bidisperse suspensions.

We begin with a series of experiments on monodisperse suspensions to estimate the range of filtration regime and the amount of particles that are filtered. In Fig. 2.8, we report results of experiments performed with a monodisperse suspension ($2\,a = 240\,\mu$m, $\phi_{240} = 0.625\%$). After each trial, we count the number of particles per unit area N_A on the plate. We also introduce N_V, the number of particles per unit volume in the bulk suspension, which is equal to the prepared volume fraction ϕ multiplied by the volume of a single spherical particle such that $N_v = 4/3\,\pi\,a^3\,\phi$. When the particles are expected to be entrained, *i.e.*, the thickness of the coating film is large enough, N_A and N_V are related through the thickness of the fluid coating h: $N_A = N_V\,h$. We plot a theoretical value of N_A/N_V based on the LLD prediction for h when the particles are not filtered (NF):

$$\left.\frac{N_A}{N_V}\right|_{NF} = 0.94\,\ell_c\,Ca^{2/3}. \tag{2.15}$$

In Fig. 2.8, we show the evolution of N_A with the Capillary number. We observe that Eq. (2.15) agrees well with the experimental results in the yellow region. Here, the viscous force that entrains the particle in the liquid film is larger than the capillary force that would keep the particle in the liquid bath corresponding to a soft filter larger than the particle size. The particle is entrained passively with the liquid, and the volume fraction in the coating film is similar to the volume fraction ϕ in the bulk suspension. For low

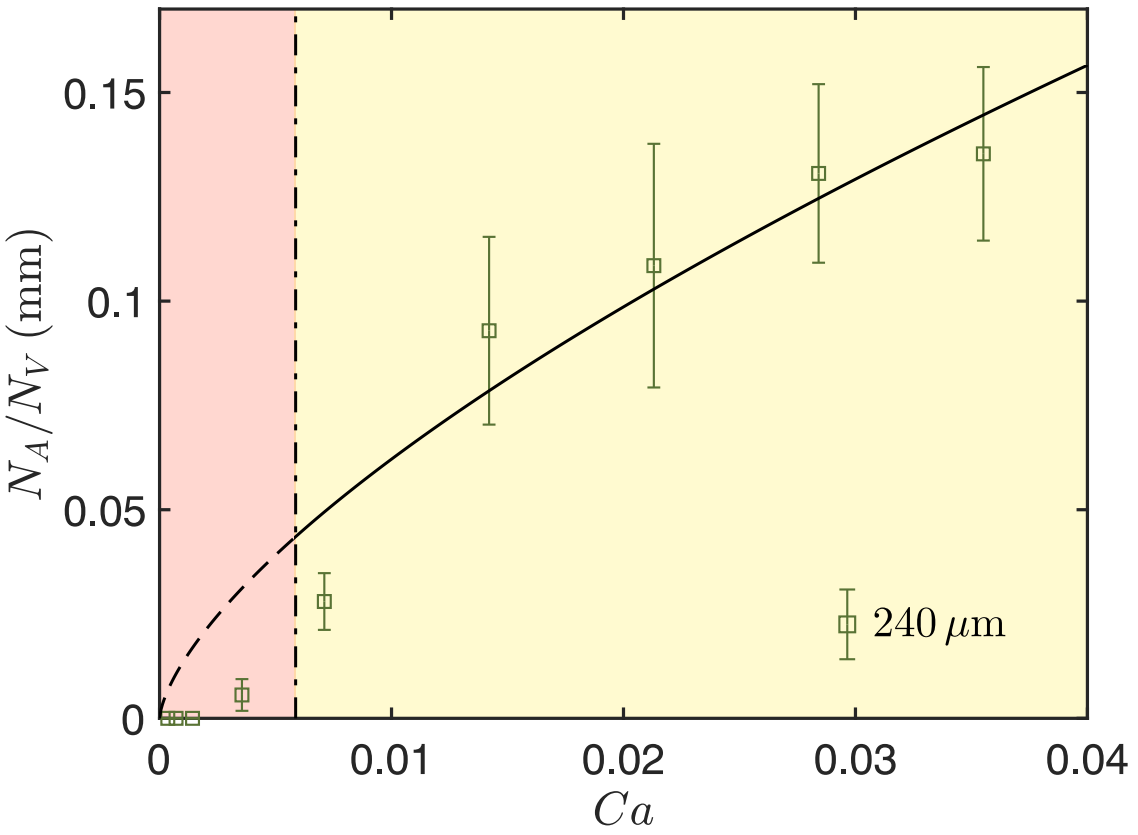

Figure 2.8: Data from a series of monodisperse filtration trials with $2\,a = 240\,\mu$m particles. Experimental measurements are shown in green. The dashed and the continuous lines indicates h as governed by the LLD law, in the region where the theory is not expected and expected to apply, respectively. At sufficiently large Ca (yellow region), particle entrainment follows the theoretical prediction based on volume of fluid entrained [Eq. (2.15)]. Below the entrainment threshold (red region) particles are excluded by capillary forces at the meniscus, resulting in a large disparity between theoretical and measured entrainment. A vertical dash-dotted line for this threshold is shown at $Ca^* = 0.24\,Bo^{3/4} \simeq 6 \times 10^{-3}$.

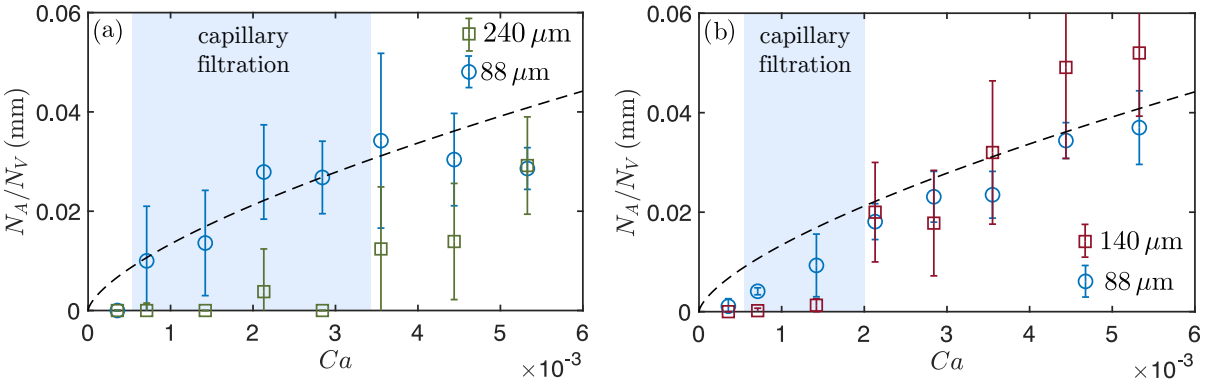

Figure 2.9: Data from two filtration experiments with bidisperse suspensions: (a) 88 μm (blue circles) and 240 μm (green squares) at $\phi_{88} = 0.09\%$ and $\phi_{240} = 0.91\%$; (b) 88 μm (blue circles) and 140 μm (red squares) at $\phi_{88} = 0.17\%$ and $\phi_{140} = 0.83\%$. The filtration regime is highlighted in blue, where 88 μm particles are separated from larger particles in the suspension. At low Ca very few or no particles are entrained, while at high Ca both particle sizes are entrained at similar relative quantities.

enough Ca this relationship breaks down as particles are trapped at the meniscus and do not coat the substrate, as observed in the red region: the soft filter is smaller than the particle size. The transition between the two regimes at Ca^* determines when the capillary filtration is possible: when $Ca < Ca^*$, particles can be filtered out of the liquid film, whereas when $Ca > Ca^*$, particles are entrained in the liquid film.

The capillary threshold for particle entrainment, Ca^*, depends on the particle size through the Bond number of the particle $Bo = (a/\ell_c)^2$, $Ca^* = 0.24\, Bo^{3/4}$ [33, 5]. Recently this relationship has been experimentally demonstrated across different particle sizes and working fluids [7, 4]. Note that this transition does not correspond to an inertial effect, as $Re \ll 1$ for all of the experimental data. In Fig. 2.8, the predicted threshold value is $Ca^* = 6 \times 10^{-3}$ [5], which is in good agreement with our measurements. In the following, we take advantage of this relationship by tuning Ca to filter suspensions.

To demonstrate this, we perform experiments for two bidisperse suspensions of different size ratio a_B/a_S, where a_B and a_S are the radii of the big and small particles in the suspensions, respectively. Here, we consider: (i) $2\,a_S = 88\,\mu$m and $2\,a_B = 240\,\mu$m and (ii)

$2\,a_S = 88\,\mu$m and $2\,a_B = 140\,\mu$m. We consider a low volume fraction, $\phi_B + \phi_S = 1\%$ to avoid cluster formation and limit the change of viscosity. In addition, the volume fraction ratio ϕ_B/ϕ_S is such that the number of small particles is not too large compared to the number of large particles [64]. The results are reported in Fig. 2.9(a)-(b). Since h is determined only by the fluid properties and withdrawal speed, N_A/N_V can be used to normalize the results above the threshold capillary number Ca^*, as demonstrated first in Fig. 2.8. This allows us to directly compare the entrainment of particles having different size and volume fraction. The evolution of N_A/N_V should remain the same across different particle suspensions as predicted in Eq. (2.15). For the bidisperse suspensions, we observe a clear range in which capillary filtration occurs. In Fig. 2.9(a), we note a capillary filtration regime of approximately $5 \times 10^{-4} < Ca < 3.5 \times 10^{-3}$ for separating $88\,\mu$m particles from $240\,\mu$m particles. In this range, the number of $88\,\mu$m particle entrained scales with the volume of fluid entrained, dictated by h, because $Ca > Ca^*_{88}$. On the other hand, $240\,\mu$m particle entrainment falls significantly short in this region, because $Ca < Ca^*_{240}$. We note that this region has a range of $\Delta Ca = 3 \times 10^{-3}$. The optimal Capillary number to achieve filtration is thus at a value slightly smaller than Ca^*_{240} where the number of small particles entrained will be the largest and equal to $N_A \simeq 0.94\,\ell_c\,{Ca^*_{240}}^{2/3}\,N_{V,88}$, where $N_{V,88} = 4/3\,\pi\,{a_{88}}^3\,\phi_{240}$, so that $N_A \simeq 3.94\,\ell_c\,{Ca^*_{240}}^{2/3}\,{a_{88}}^3\,\phi$. In Fig. 2.9(b), we see that the effective range of capillary filtration is significantly reduced when separating $88\,\mu$m particles from $140\,\mu$m particles, at approximately $5 \times 10^{-4} < Ca < 2 \times 10^{-3}$. In this case, $\Delta Ca = 1.5 \times 10^{-3}$.

The range of Capillary number can limit the filtration resolution when the particles are too close in size. To estimate ΔCa, we consider that a particle of radius a_S will be entrained for $Ca > Ca^*_S = 0.24\,{Bo_S}^{3/4}$. Similarly, a second larger particle of radius a_B will remain in the liquid bath for $Ca < {Ca_B}^* = 0.24\,{Bo_B}^{3/4}$. Therefore, the capillary

filtration range is

$$\Delta Ca = Ca_B^* - Ca_S^* = 0.24 \left(\frac{a_B}{\ell_c}\right)^{3/2} \left[1 - \left(\frac{a_S}{a_B}\right)^{3/2}\right]. \tag{2.16}$$

Using this expression, we find that the predicted capillary filtration range for the 240 μm/88 μm bidisperse suspension is $\Delta Ca_{240/88} = 3.3 \times 10^{-3}$ and for the 140 μm/88 μm suspension $\Delta Ca_{140/88} = 1.3 \times 10^{-3}$. These values are in good agreement with the values measured experimentally. Capillary filtration via dip coating may be best suited for applications in which ΔCa is large, corresponding to the situation where the filtered particles are significantly smaller than others, which may often be the case in removing large defects from industrial coatings or for biosample purification (e.g. bacteria $\sim 1\,\mu$m from mammalian cells $\sim 10\,\mu$m). It has been demonstrated that bioparticles follow a similar entrainment scaling as inert particles [5]

The efficiency of the filtration process within the range of capillary number allowing separation is illustrated in Fig. 2.10. The histograms represent the size distribution of the particles in the suspension (before the capillary filtration) on the top half and on the plate (after capillary filtration) on the bottom half. The large particles are completely removed while all the small particles are entrained, which results in a very similar probability distribution. If one were to filter a polydisperse suspension, successive dip coating experiments with varying capillary numbers would allow removing particles of unwanted size while retaining particles while retaining desired sizes.

Besides, the upper and lower filtration limits allow estimation of the maximum theoretical throughput for capillary filtration via dip coating. Given particles of radius a, substrate width W, withdrawal speed U, coating thickness h and fluid properties η, ρ and γ, the maximum withdrawal speed which does not entrain large particles, reached at Ca_B^*, is for $U_B^* \simeq 0.24(\gamma/\eta)(a_B/\ell_c)^{3/2}$. Thus the maximum particle throughput for a

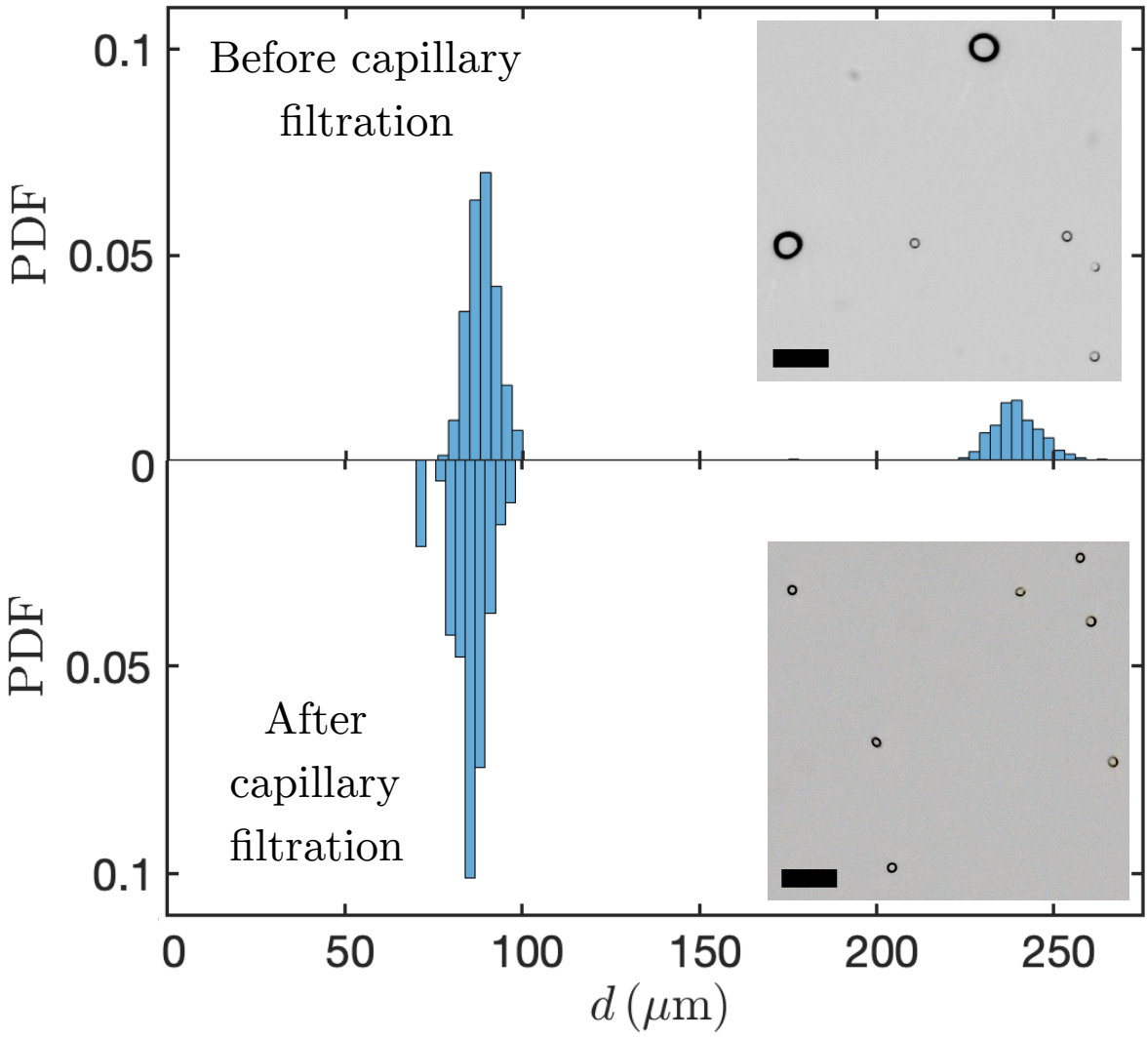

Figure 2.10: Example of capillary sorting of a bidisperse suspension: $88\,\mu$m and $240\,\mu$m at 0.91% and 0.09%, respectively. The experiment is performed at $Ca = 3 \times 10^{-3}$ and demonstrates that the particles collected in the liquid film are only the smallest ones. Insets: bidisperse suspension before (top) and after (bottom) the capillary filtration. Scale bars are $500\,\mu$m.

continuous planar substrate is given by $Q_p = 0.24\, w\, h\, (\gamma/\eta)(a/\ell_c)^{3/2}\, \phi$. Separated particles could be collected by either physical exclusion using a wiper, or by withdrawing the coated substrate from a secondary reservoir at a lower Ca [68].

A challenge with this method is that at higher volume fraction ϕ, particles can assemble into clusters in the meniscus and be entrained at a threshold capillary number Ca^* smaller than the expected value, thus reducing the range of ΔCa where capillary filtration is possible [5]. In addition, as large particles are filtered at the meniscus, the local volume fraction ϕ increases. This increases the local viscosity η [69, 19], and the local Ca. This aspect is best mitigated by working with dilute suspensions, which has the disadvantage of lowering effective particle throughput. However, of all the soft filtration techniques recently proposed [64, 65], capillary filtration via dip coating possesses the greatest scalability to overcome the necessity of dilute suspensions.

Finally, we note that we have applied this separation technique using a single working fluid, hence a single set of fluid properties. However, this technique relies only on the entrainment threshold for individual particles, which has been characterized by previous works across a broad range of particle sizes and working fluids [7, 4]. Therefore, nondimensionalization by the Capillary and Bond numbers will allow future application of this technique.

In this letter, we have demonstrated the selective exclusion of large particles at the meniscus of a dip coating interface in a capillary filtration process. When suspended particles differ in size, smaller particles can be selectively removed at the appropriate Ca, while larger particles remain in the bath. We have experimentally shown that this technique can separate particles in a bidisperse suspension. We quantify the separation range to give some insight into the resolution of this technique, and provide an estimate for maximum theoretical throughput for any dip coating filtration system using a planar substrate. Combining this mechanism with the scalability and robustness of dip coating

represents a promising approach for high throughput size-based filtration.

2.4 Future Perspective on Dip Coating

The two studies presented thus far highlight dip-coating as a versatile platform that can be adapted for selective size-based separation of suspended particles. For flat substrates, this process is controlled through careful selection of the withdraw velocity. However, as highlighted in the previous study regarding flat substrates, it can be difficult to separate particles of similar size purely based on withdraw velocity. For thin cylindrical substrates, we have an additional parameter for control: the substrate radius. If we compare the entrainment expressions obtained for a thin fiber and a plate (both presented above), we can show that proper fiber radius selection can amplify separation resolution by a factor of 3 or more! This reduces the requirement for ultra-precise velocity control for small particles of similar size.

With a second parameter, fiber-based dip-coating filtration systems offer numerous advantages over traditional filtration techniques. Dead-end filtration, the most common filtration technique in which a suspension must flow directly through a filter medium which traps particles larger than the filter pores, is extremely versatile but comes with several disadvantages. Some examples include typical HVAC air filters, which remove primarily dust and pollen from flowing air, and water filters, which remove parasites and large single-cellular organisms from untreated water. As large particles begin to accumulate on the filter, they restrict the flow. This either reduces throughput, due to a reduced flow rate, or it increases the energy cost if a constant flow rate is desired. Additionally, as the filter cake grows, its porosity decreases, capturing particles which are smaller than intended. If those particles are desirable, this represents a reduction in filtration efficiency.

With dip-coating as a new filtration platform, the confinement is soft, rather than the rigid confinement associated with traditional filters. While large particles are excluded

from the coating film, similar to how large particles are excluded when passing through a filter, they recirculate into the bath, rather than accumulate at the point of filtration. Therefore, optimized dip-coating filtration systems would not suffer from the same disadvantages of traditional filtration. With no filter cake, throughput and filtration efficiency would remain constant.

This concludes my focus on *soft confinement* of suspensions by a capillary interface. For the remainder of this work, I focus on *hard confinement* by solid geometric constrictions. There are two major differences between these cases. First, the confining surfaces cannot significantly deform in the case of hard confinement. Second, suspended particles can attach to solid surfaces via Van der Waals interaction, which is not the case for capillary surfaces.

Ultimately, this distinction is an excellent transition into the rest of my thesis work and the general topic of clogging. All traditional filters, which are examples of hard confinement, eventually clog once the filter cake has grown to the point that the desired flow rate is no longer achievable; at which point the filter must be replaced. While dip-coating may provide one solution for size-based filtration with minimal clogging, there are many other systems which clog. Some examples include irrigation lines, silo discharge exits, and sewer inlets/outlets. All of these are examples of hard confinement.

In the following chapters, I discuss how these different systems clog, summarize historical and current techniques to manage clogging, and investigate how to leverage hydrodynamics to minimize clogging in existing systems.

Chapter 3

Introduction to Clogging and Pulsatile Flows

This chapter provides an introduction to the phenomenon of clogging, when suspended particles stop flowing due to confinement, thereby arresting the flow. Historically, clogging has been addressed in a variety of ways, primarily though filtration or through chemical treatment of the flow path. We have already discussed some of the disadvantages of in-line filters, primarily that they still clog eventually and must be replaced. Not to mention the additional energy cost required for filtration, since the addition of a filter will necessarily increase the required pressure to drive the flow. But chemical treatment, such as the addition of chlorine as a biocide or the addition of acid to reduce mineral buildup, also has its own drawbacks. Namely that not all chemicals are compatible with all systems, on top of the added risk of environmental escape. Besides, flushing a line with chemicals can be costly —the acid flush used to maintain sewage lines on some U.S. air craft carriers cost about 400,000 USD. This unexpected periodic service is predicted to nearly double the operational cost a carrier over its 50 year life.

Clearly, there is room for improvement in how we manage clogging across a variety

of systems. Ideally, we should use passive techniques which are compatible with a broad range of applications, without reliance on chemical addition or heavy filtration. One strategy proposed in numerous studies is to use pulsatile flows, rather than steady flows, to drive flow systems which are susceptible to clogging. Unlike steady flows, pulsatile flows yield a continually varying shear environment which may help prevent the long-term growth of a clog. After all, nearly every macroscopic organism (those that can't utilize diffusion) rely on pulsatile flows to deliver nutrients through their circulatory system.

Therefore, the second half of this chapter provides some background on pulsatile flows as well. Besides remediating clogging, pulsatile flows have been used in microfluidic systems for a variety of applications, including microdroplet generation, enhanced mixing, and particle separation. As a result, numerous strategies for implementing pulsatile flows have also been developed. All of these are discussed in the pulsatile review at the end of this chapter.

3.1 The Physics of Clogging

3.1.1 Abstract

From clogged pipes to clogged highways to clogged arteries, stopping the flow is always inconvenient and sometimes quite dangerous. Clogging is often observed in confined flows having either too many particles or too large of particles. Clogging can be so inconvenient, necessitating lost time and labor, that we have historically worked very hard to try to prevent it. Yet, despite a rich history of empirical clog prevention methods, the underlying physics of clogging has only recently become an active research topic. Many parameters influence the probability of clogging, such as the properties of the particles, the concentration of the suspension, and the geometry of the systems in which the suspension flows. As the governing physics are revealed, new methods and design strategies to mitigate clogging are emerging. However, there are still numerous open questions to better model, predict, and prevent the formation of clogs.

3.1.2 When the Flow Stops, We Pay

Clogging can occur whenever a suspension, comprised of discrete particles dispersed in a liquid, flows through a confined geometry. These geometries or constrictions can be microscopic, such as the pores of a filter and microfluidic devices, or macroscopic, such as pipes transporting water and log jams forming under a bridge. As a result, clogging occurs in many environments and at various scales, as illustrated by the range of examples in figure 3.1.

Clogging is a major issue in many engineering systems: the clogging of inkjet printer nozzles by colloidal particles impairs their performance in the long term. Similarly, the frequent formation of clogs in nozzles used to dispense fiber-filled polymer inks in

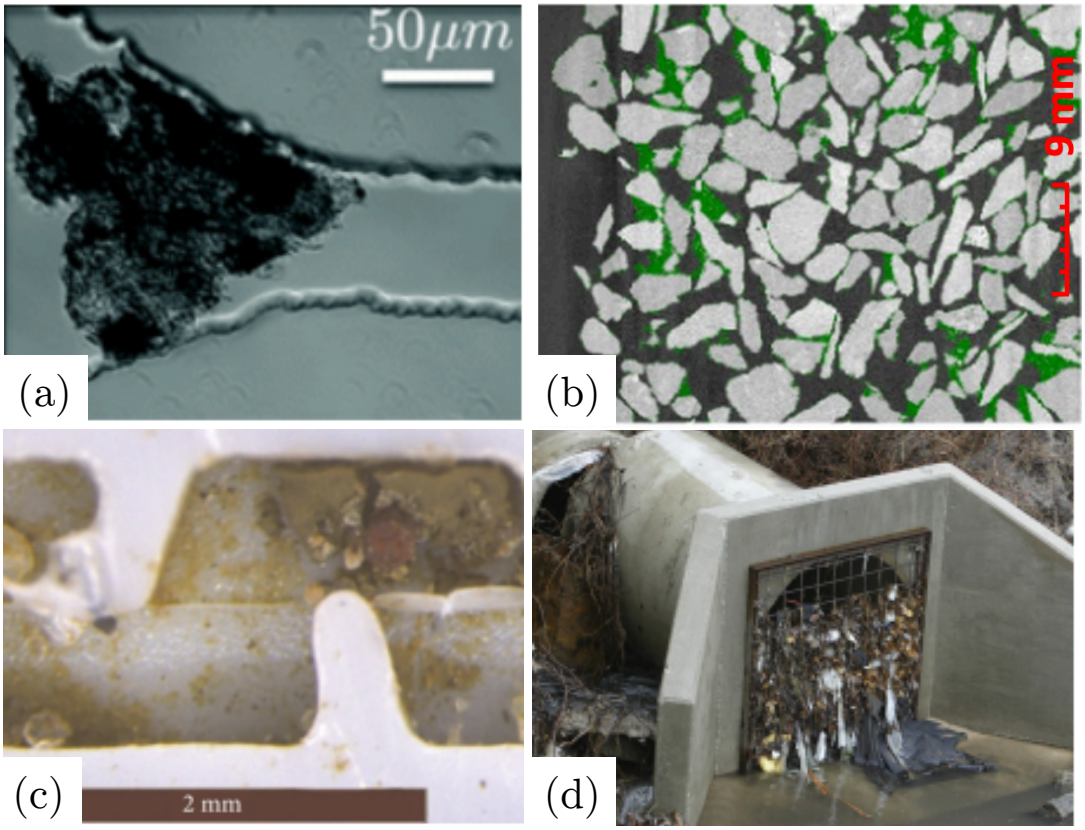

Figure 3.1: **Some examples of clogged or partially clogged systems at different scales**. (a) A protein aggregate stuck in a microfluidic constriction smaller than the aggregate size. (b) X-ray computed tomography of the internal structure of a porous media in which suspended solid particles have flowed for several hours. The particles trapped in the system are shown in green. (c) An irrigation emitter which has become clogged by fine sediment sticking to surfaces along the flow path. (d) Sewer drain outlet clogged by plastic bags, trash, and other debris.

extrusion-based additive manufacturing processes limits the concentration of fibers that can be used. Similarly, the possible presence of protein aggregates in solutions of monoclonal antibodies constitutes a threat to the reliability of autoinjection devices that allow patients to self-administer medicine since the aggregate may clog the nozzle, as shown in figure 3.1(a).

At larger scale, clogging is detrimental to water sustainability. Indeed, many arid regions rely on underground water as a primary source of freshwater. These underground caches are porous media called aquifers, and are either naturally recharged by precipitation or artificially recharged by redirecting surface water or injecting water through a deep well. In either case, recharge and extraction rely on water flowing through porous rock and sediment, similar to a filter. Over time, cycles of drainage and recharge can cause fine suspended particles to clog the aquifer, as can be seen in the example of figure 3.1(b) showing a 2D slice of a porous media where particles (in green) get deposited in the pores and may eventually clog and decrease the permeability of the medium. This increases the energy cost for extraction and recharge, and also reduces the operational life of the aquifer. Aquifers are not the only water resource that can be crippled by clogging. Roughly 70% of the water in the United States is used for irrigation. Microirrigation, which uses a series of small targeted emitters to water crops, has been demonstrated to be 50% or more efficient than sprinkler and furrow irrigation, both of which lose significant water to evaporation. However, less than 10% of irrigated land in the U.S. utilizes drip irrigation, primarily due to their clogging susceptibility. One main issue is that the narrow channels in drip irrigation emitters can easily be clogged by suspended sediment, fertilizers, and biofilms like algae and bacteria, as shown in figure 3.1(c).

Civil engineering is another field where clogging leads to many challenges and issues. As cities have grown both in physical size and in population, city infrastructure must continually handle more stuff. In particular, sewers for both wastewater and storm runoff

allow cities to maintain sanitary living conditions while also providing some protection against flooding during periods of high precipitation. These sewers are typically accompanied by both inlet and outlet grates to prevent people and other large objects from entering the sewers. Over time, these grates can become clogged by all sorts of things, including moss, dirt, and leaves, in addition to all manners of urban trash, such as plastic bags and cardboard, as shown in 3.1(d). When sewers clog, they cannot handle their designed throughput, potentially resulting in significant urban flooding. Thus maintenance of sewer inlets and outlets is essential to ensure that flooding does not occur. However, determining the optimal maintenance schedule can be difficult, as clogging risk and clogging rates have historically been hard to estimate and can vary based on region and weather.

While we focus here on the clogging of systems by liquid suspensions of particles, particles in air, where the interstitial phase between the particles can be neglected, can also clog. Perhaps the most classic case lies in granular flows, such as grains draining through a silo. Grains such as wheat are rough and irregularly shaped. Additionally, with no liquid to lubricate the grains, they exhibit high friction with each other, which can easily cause particles to jam and clog at the silo outlet. This effect becomes much worse with high humidity, as grains also become more cohesive. When silos clog, the stuck grains must often be manually cleared — either with a long pole, which can be dangerous since the operator is in the flow path, or an air cannon, which is much more expensive. The clogging of grains also shares many similarities with the clogging of active particles, such as cars, people, or livestock passing through a constriction. It has been observed that when sheep are entering or leaving their corral, they often overload the passageway, blocking each other and preventing other sheep from moving. It turns out this is a very important consideration when it comes to evacuation safety for large buildings and event spaces. During emergencies, people tend to rush towards the exit,

since the exit represents safety. However, emergency exits can become a bottleneck, and if too many people try to pass through at once, these exits can also become clogged. In the best case, this limits how quickly people can evacuate, which is sub-optimal in emergencies. In the worst case, people may try to force each other through or even trample one another, turning this symbol of safety into a hazard itself.

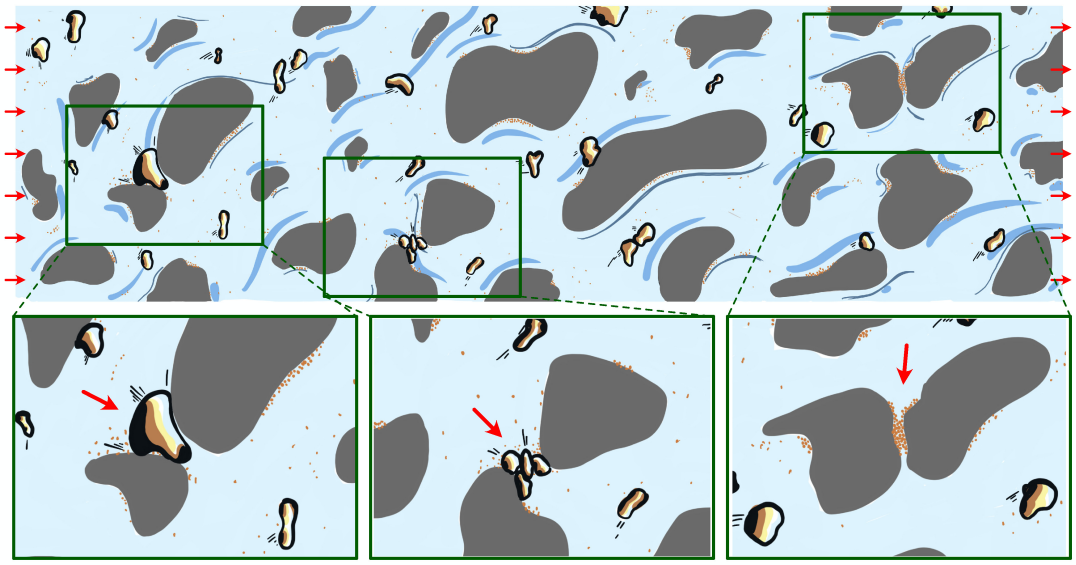

Figure 3.2: A suspension of particles flowing in a confined system, like the porous media depicted above, can clog the system at constrictions or pore throats following different mechanisms depending on the pore and particles properties. These mechanisms are highlighted in the insets. (left) Sieving by a particle with one dimension larger than the width of the constriction. (center) Bridging by the formation of an arch of particles arriving simultaneously at the pore. (Right) Progressive aggregation of small particles on the channel walls that could lead to the total clogging of the pore. (Schematics courtesy of Ram Sharma.)

The physics which governs how flowing particulate suspensions can clog a system has become an increasingly active research topic. This is, in part, due to the complexity of clogging. Its ubiquity means it spans many length scales, from bacteria to boulders, time scales, from less than a second to years, and often requires sophisticated equipment to study critically as direct visualization of clogging is challenging. Yet, the prediction of

clogging can lead to new design principles to improve the reliability of many systems. One of the first steps in tackling the broad topic of clogging is to categorize the dynamics, because systems clog in different manners. Generally, these clogging mechanisms are categorized as (1) sieving, when particles are too large to pass a constriction, (2) bridging, when particles jam each other at a constriction and form a stable arch, and (3) aggregation, the successive deposition of small cohesive particles at a constriction. While one or two of these mechanisms may be more common in certain systems, generally all of these mechanisms are present throughout a clogging process, adding to the complexity of establishing a general picture.

3.1.3 A Tale of Three Mechanisms: Sieving, Bridging, and Aggregation

To help describe clogging, there are some common parameters one must keep in mind. The particle size, shape, deformability, and the geometry of the system in which the suspension flows are all going to play a role on the clogging dynamics. When the particle is quasi-spherical, the size of the particle is often described by its diameter D. However, more complex shapes, such as fibers or aggregates of particles, can also clog a constriction. Equally important is the minimum dimension of a constriction W, which could represent the diameter of a filter pore, a reduction in cross-section for a pipe system, or the width of an emergency exit. The volume fraction of particles in a suspension ϕ, defined as the ratio of the volume of particles found in the total suspension volume, is also going to influence the probability of clogging. Another way to think about volume fraction is how close the particles are to each other, on average. Finally, the physical and chemical properties of the particles, for instance, their roughness, their adhesion, and cohesion between particles, is also going to play a crucial role in clogging, especially

in selecting the dominant clogging mechanism. The combination of these mechanisms contributes to establishing a unified framework of the physics of clogging. Nevertheless, each mechanism can be isolated to provide a fundamental understanding.

Sieving: too big to fit

The simplest case of clogging is when one of the dimensions of a particle is too large to pass a constriction. For instance, for a rigid spherical particle of diameter D and a constriction of width W, clogging occurs for $D/W \geq 1$. This clogging mechanism is one of the most common as it is routinely used to separate small particles from larger ones that remain blocked by a screen. Since most industrial suspensions are polydisperse, made of different particle sizes, the presence of only a few very large particles in the suspensions can be highly detrimental to the performance of systems presenting constrictions. Besides, since the aggregation of particles on a channel wall reduces the cross-section of the channel, sieving is often the final event in many clogging environments.

Although sieving seems to be a simple mechanism for spherical particles, it becomes less straightforward when more complex particles are involved. For instance, anisotropic particles, such as fibers or leaves, may enter a system at a given orientation but later clog the channel after some reorientation. This is why gutters must be periodically cleaned to prevent leaves and other debris from reorganizing over time and clogging the gutter. For rigid anisotropic particles, an approach to predict the clogging of a constriction of width W is to characterize the shape of the anisotropic particles using the maximum Férét diameter L_{F} as the largest distance and the minimal Férét diameter l_{F} diameter as the smallest distance, as illustrated in figure 3.3. Such a rigid anisotropic particle will always clog by sieving at a constriction if $l_{\mathrm{F}} > W$, and will never clog if $W > L_{\mathrm{F}}$. However, for an intermediate size of constriction, $l_{\mathrm{F}} < W < L_{\mathrm{F}}$, the orientation of the particle when arriving at the constriction will play a major role. If the particle passes the constriction

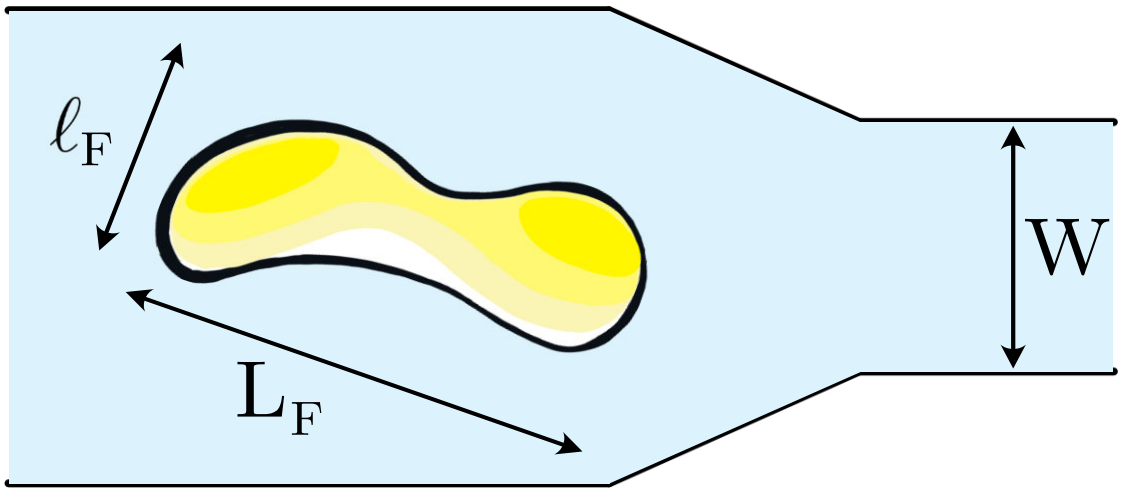

(a)

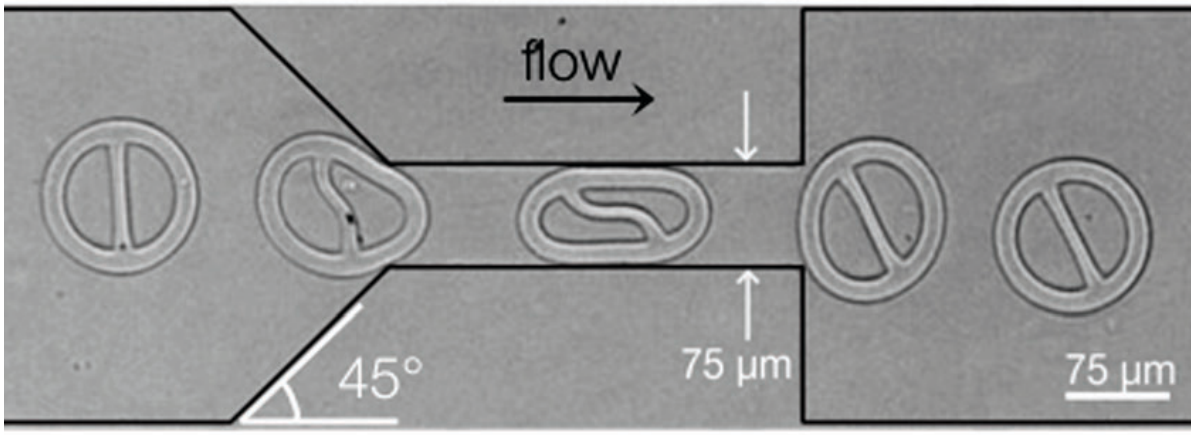

(b)

Figure 3.3: (a) Schematic of a deformable and anisotropic particle with minimal and maximal Feret's diameter ℓ_F and L_F, respectively, arriving at a constriction of width W (Schematics courtesy of R. S. Sharma). (b) A flexible particle can squeeze through a constriction smaller than its size if the input pressure is large enough [Reproduced from Chen *et al.* (Soft Matter, 2017)].

with its minor axis aligned with the flow, no clogging will occur since $l_F < W$. Finally, if the particle is aligned perpendicularly to the flow, sieving will occur as $W < L_F$.

Another complexity arises when the particles are deformable. This situation is particularly relevant to biological applications since vesicles, cells, and protein aggregates are all deformable. A deformable particle larger than a constriction can still enter it and may even flow through for a sufficiently large applied pressure.[70] Indeed, increasing the pressure increases the force applied to the particle, allowing it to squeeze through a constriction as it deforms. Beyond a pressure threshold that depends on the width of the constriction, as well as the size and the mechanical of the particles, the particle can squeeze through as illustrated in Figure 3.3(b).

Sieving is a somewhat random process, as it depends on the amount of particles larger than the constriction or pore sizes. For systems with many pores, sieving can usually be modeled as a Poisson distribution, where the clogging of each pore represents an independent event, the probability of which depends on the size distribution of suspended particles.[56] Overall, the most common way to prevent sieving is to prevent large particles from entering the systems, usually through upstream filtration. Even then, sieving still happens at the filter, where small pores prevent the passage of large particles.

Bridging: too crowded to pass

For dilute suspensions, typically of volume fraction ϕ smaller than a few percent, particles tend to pass through constrictions one at a time. Thus clogging by bridging is generally observed at higher volume fractions when particles can arrive at a constriction simultaneously. If too many particles arrive at once, they can jam each other, spontaneously forming a bridge, as illustrated by the time lapse in figures 3.4(a)-(c). Bridging or arch formation occurs when constrictions have a size W larger than the particle size D but of the same order of magnitude. For spherical non-cohesive particles, bridging

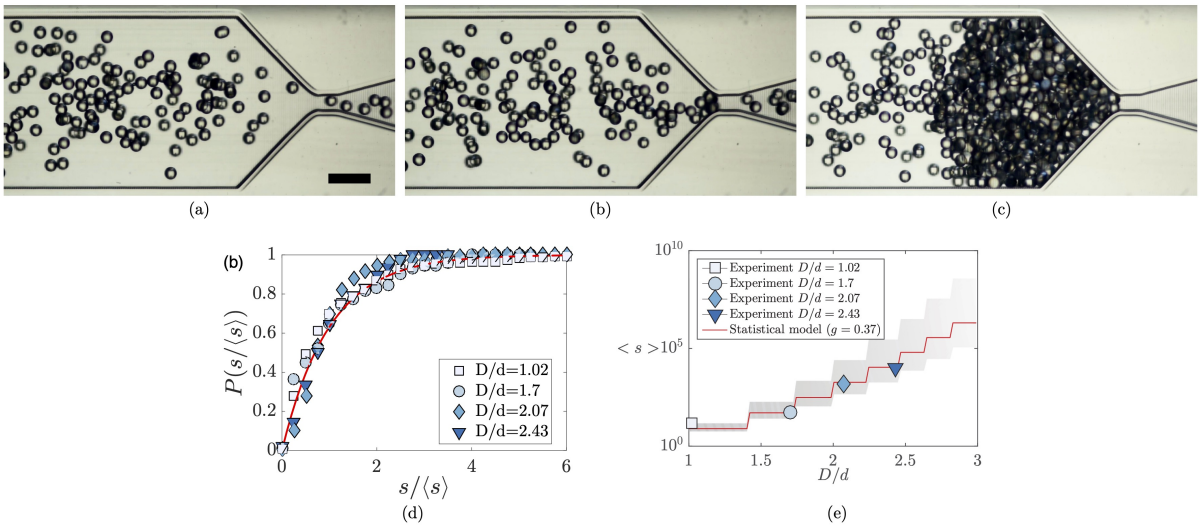

Figure 3.4: (a)-(c) Example of clogging by bridging of particles at a constriction (courtesy of D.-H. Jeong and N. Vani). (a) Particles are flowing through the channel until (b) a sufficient number of particles reach the constriction at the same time and clog the constriction. (c) The clogging prevents the flow of particles, which then form a filter cake. The scale bar is 2 mm. (d) Probability of clogging after s particles have escaped the constriction and (d) evolution of the average number of particles flowing through the constriction before clogging when varying the size of the constriction [Reproduced from Marin *et al.*, 2018 [71]].

has been observed to occur only when $W/D < 5$. For highly anisotropic particles, such as fibers or flakes, or cohesive particles like powders, this threshold can be pushed to $W/D < 8$ or even higher due to differences in particle arrangement and the resulting force network at the bridge [72]. Clogging by bridging shares many common features with the clogging of silos, where particles smaller than the constriction can form stable arches. The main difference is that the clogging of silo occurs only at the large packing since the dry particles are subjected to gravity.

A common approach used to describe such systems is to measure the number of particles s or the volume of suspension that flows through the constriction before a bridge is formed. The two relevant quantities are then the average number of particles $\langle s\rangle$ (or the average volume of suspension) before clogging occurs and the resulting distribution of the number of particles escaping. The latter has been shown to exhibit an exponential

decay owing to the constant probability of clogging during the flow. As a result, the probability of clogging also follow and experimental distribution, illustrated in figure 3.4(d). An approach to predict the average number of particles, or the average volume of fluid, flowing through the constriction before the bridging occurs is to assume a random distribution of particles in the channel and consider that a sufficient number of particles arrive at the constriction at the same time. For instance, in a 2D system and particles of diameter D, a constriction of width W will clog by bridging if the number of particles arriving simultaneously is $n \geq \text{floor}(W/D + 1)$. Considering a given particle density, it is then possible to show that the average volume of fluid dispensed before clogging will increase if the width of the constriction is increased [figure 3.4(e)]. Similarly, clogging will also be delayed if one decreases the volume fraction of the suspension. Clogging by bridging exhibits a particular feature of intermittency, where the flow clogs and unclog periodically, when some perturbations are present in the system. For intermediate values of W/D an intermittent regime where the arch periodically breaks can be observed. Overall, clogging by bridging will be significant for moderate values of W/D, typically for $1 < W/D < 5$, and large enough volume fraction ϕ. These conditions provide a framework to minimize clogging by bridging.

Aggregation: too sticky

Some particles, especially very small particles, can stick to surfaces and to each other. If a particle attaches to the wall of a constriction, that constriction becomes a little smaller, as illustrated in figure 3.5. Aggregation is when this deposition happens repeatedly, eventually leading to severely reduced constrictions which are more susceptible to both bridging and sieving. While initial deposition depends on particle-wall interaction, interparticle interaction can significantly increase the aggregation. The particle-fluid interaction is also an important parameter, because the flow determines how quickly par-

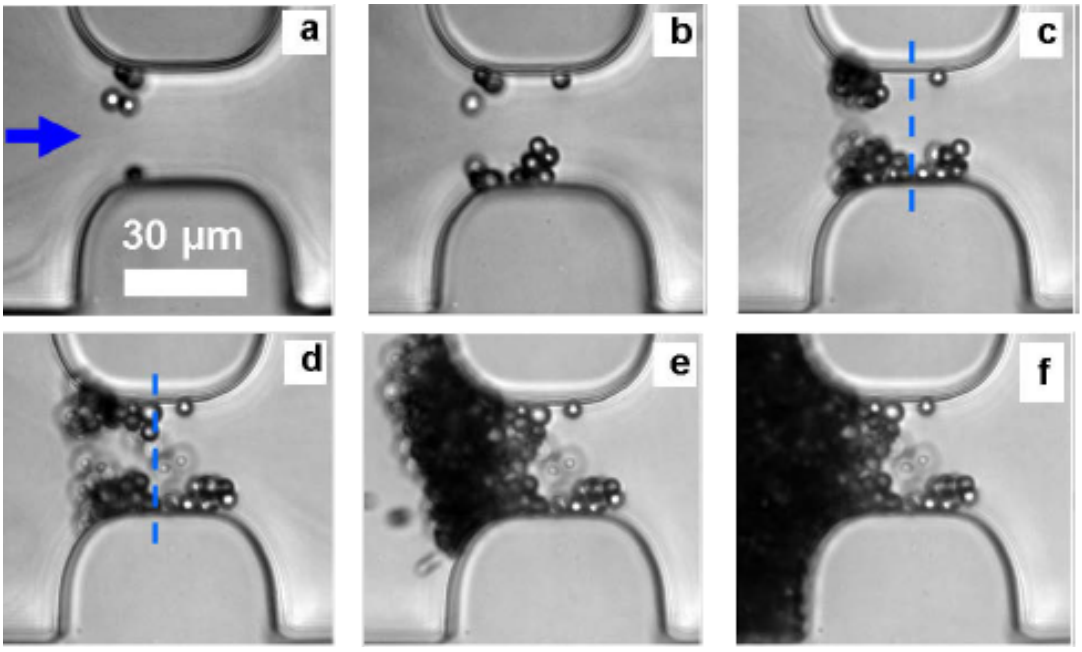

Figure 3.5: Example of clogging by the successive deposition of particles at the constriction [Dersoir et al. (2015)].

ticles will arrive, as well as the shear force environment that particles experience, which may influence whether or not particles can be eroded.

For particles like sediment or microplastics, aggregation is primarily due to Van der Waals forces, which are short-range forces resulting from distance-dependent interactions between atoms and molecules. Other small particles, such as bacteria and algae, can also be sticky. While still subject to Van der Waals forces, bioparticles often possess a variety of adhesion molecules on their exterior, allowing them to attach to surfaces or each other with greater force than abiotic particles. Once attached, many bioparticles can also multiply along a surface, while excreting chemicals that serve as a glue to bind them to a surface.[73]

While sieving and bridging are governed primarily by steric interactions, aggregation is more complicated and sensitive to chemistry. For particles in pure water, aggregation is often limited by an electric double layer repulsion. However, pure water is extremely rare

outside of specialized applications like wafer processing or scientific research. Changes in pH or the addition of salt increase ion availability in suspensions and can drastically reduce double-layer repulsion, allowing Van der Waals interactions to dominate. Even small concentrations of monovalent salt (< 0.1 M) can significantly increase the aggregation rate in systems.[70] Usually, clogging by aggregation can be observed even for constrictions much larger than the particle diameter and for very dilute suspensions. However, this clogging mechanism usually takes place over long period of time, from hours to years.

3.1.4 Clog Prevention: The Flow Must Go On

Since clogging is a major issue in a broad range of fluid systems, a large portion of contemporary research surrounding clogging investigates new techniques to prevent or mitigate it. Just as different systems result in different clogging dynamics, techniques to prevent clogging also vary based on the predominant mechanism, *i.e.*, there are different techniques to prevent sieving, bridging, and aggregation.

When it comes to sieving, a common way to prevent clogging for an ideal suspension of rigid spherical particles is to filter them upstream. However, most suspensions are not ideal. Many particles are anisotropic in shape, and may be deformable, such as cells or protein aggregates. These imperfections are actually opportunities to prevent clogging. For deformable particles, or even rigid particles flowing through a deformable constriction, elevated pressure can be used to squeeze particles through the constriction.[70] When this happens, the deformation of the particle, constriction, or both results in an adjustment of D/W such that the particle can pass. Many mammals, including humans, rely on this phenomenon as red blood cells must deform in order to flow through capillaries. In fact, there are numerous diseases that alter the deformability of red blood cells, increasing

the risk of blood clots and stroke since these cells cannot flow freely through small capillaries if they become too stiff. Highly anisotropic particles may clog a constriction in one orientation, but flow freely in another orientation. To prevent sieving in this case, the particle must be aligned such that it can pass the constriction. For some shapes, particularly those with high aspect ratios, this can be achieved through hydrodynamics. At low volume fractions, slender particles subject to a shear flow tend to align their longest dimension with the flow direction. However, at higher volume fractions or high flow rates possessing turbulence, the motion of anisotropic particles in confined systems is still an active research topic.

The simplest way to prevent bridging is to ensure that the suspension volume fraction is sufficiently low and the constriction is sufficiently large. However, in the case of grain silos or emergency exits, this can be impractical or even impossible. It turns out there are other ways to help prevent suspended particles from bridging. Indeed, once a bridge has formed in a static system, all of the kinetic energy is dissipated and the bridge will remain stable with an unclogging probability of zero. However, the stability of the bridge can be broken by introducing perturbations to the system.[72] One way to periodically perturb a system is through vibration with a piezoelectric device for dry granular media or by adding fluctuations to the flow for a suspension. Depending on the frequency and intensity of vibration, this has been shown to increase the unclogging probability to a nonzero value. Thus systems that rely on vibration to break bridges often exhibit an intermittent flow, reflecting both clogged and unclogged states. Another passive method to prevent bridging in silos is to place an obstacle just upstream of the constriction. With proper placement, this has been shown to reduce the bridging probability by a factor of 100 without reducing the flow rate. Furthermore, this technique has been shown to work for both passive particles, such as grains in a silo, as well as active particles, such as sheep or humans rushing through a constriction.[74] The addition of an obstacle reduces

the pressure upstream of the outlet and modifies the conditions for bridging, with the ultimate effect of reduced bridging probability, even for dense suspensions.

Preventing aggregation has proven to be a more difficult task thus far. Nevertheless, there are some promising techniques, both old and new. For a long time, the best way to prevent aggregation has been to introduce chemicals into a system that help prevent aggregation. Some examples include pH adjustment to reduce mineral precipitation in hard water, or adding biocides like chlorine which kill bacteria and algae to prevent them from attaching and proliferating. However, chemical addition is far from ideal, as many chemicals are only compatible with specific systems. Furthermore, adding chemicals to large flows presents an environmental risk, due to uncontrolled runoff and invasion into nearby ecosystems. Thus more robust techniques are being investigated. In some cases, surface treatment can help prevent aggregation. By modifying the surface roughness or surface energy (often both) the aggregation rate can be significantly reduced for some systems. However, it is very difficult to develop surface treatments that maintain anti-clogging properties for a long time, due to either erosion or fouling of the surface. Another technique that has been proposed leverages capillary forces to remove particles.[75] For instance, this can be done by passing a slow-moving bubble through a system. As the bubble passes over particles, it exerts an inward capillary pressure which can peel particles from the surface. This process of capillary peeling has been demonstrated for both inert particles as well as bioparticles. While this process has been demonstrated for short-term particle removal, it has not yet been tested as a long-term solution to curb aggregation. Additional methods to locally increase the fluid shear could also be developed in the future.

Finally, another promising solution to mitigate clogging is by implementing pulsatile flows.[76] Studies dating as far back as the 80s report on the anti-clogging potential of pulsatile flows. Over time, it has been observed that the unsteady shear environment

corresponding to pulsatile flows may play a role in mitigating all three mechanisms of clogging. With pulsation, anisotropic particles can be rotated such that they pass a constriction and do not sieve. While particle bridges are often stable in steady flow, pulsation can reorient or break apart a bridge, restoring flow to a channel. This is similar to how vibrations can be used to prevent bridging. Finally, it has also been observed that pulsatile flows may mitigate aggregation by periodically increasing the fluid velocity and eroding particles with a temporarily elevated shear.

3.1.5 Conclusion & Future Perspective

Clogging is detrimental in many applications and, as such, numerous studies have investigated the conditions required for clogging while also trying to develop techniques to mitigate clogging. However, since there are so many different systems that can clog in distinctly different manners, there are no one-size-fits-all solutions and there is still a lot of work to be done to obtain an entire picture of clogging in constricted flows. This is why understanding the impact of different parameters on clogging is important to be able to design future systems which are continually more resilient to clogging, thus saving time, money, and energy.

Ideally, as our understanding of clogging becomes more and more technical, general guidelines for clogging risk can be established. For bridging and sieving, we know that the size ratio W/D and the volume faction ϕ are dominant parameters which determine whether or not a system will clog. Therefore, it may soon be possible to describe a sort of phase diagram for clogging. In time, parameters like roughness, particle anisotropy and deformability can also be considered. Additionally, the influence of channel geometry, such as the angle of a constriction, needs to be considered.

Aggregation is more complex, but may be handled in a similar manner. For aggre-

gation, we can assume that $W/D \ll 1$, thus the constriction width is a less important consideration for an aggregation phase diagram; although it would change the time scale for the channel to be fully clogged. Similarly, increasing the volume fraction ϕ should simply increase the aggregation rate. Rather, an aggregation phase diagram would tell us when to expect aggregation based on the competition between attachment forces, due to a combination of Van der Waals forces and additional adhesive force, and erosion forces, due to the shear exerted by the fluid. If the erosion force exceeds the attachment force, then we would expect minimal aggregation and/or an upper limit to average aggregate size. But if the attachment force exceeds the erosion force, we would expect continual aggregation and eventually a complete clog.

In order for these understandings to surface, an interdisciplinary approach is required. Depending on the application, clogging can be sensitive to hydrodynamics, biology, chemistry, and physics all at once. Suspensions may contain billions of polydisperse particles (or more) with varying properties, and their specific locations in the suspension are unknown. Thus, similar to turbulence modeling, advanced clogging models require extensive validation and iteration in order to reach a useful predictive capability. While simplified systems are essential for isolating specific aspects of clogging, complex systems must be investigated as well. Real suspensions are polydisperse and must flow through a wide variety of geometries. Field research and case studies focused on clogging in real systems will be extremely useful for helping scientists design relevant experiments while also serving as validation sources for clogging models.

3.2 Pulsatile Flow in Microfluidic Systems

The previous section provides a background on how systems clog and how clogging is currently managed. If we are interested in probing how pulsation can influence clogging dynamics, it is also imperative that we understand how to contend with pulsatile flows. The following review paper provides a physical definition for pulsatile flows and summarizes a variety of pulsatile signal generation techniques, as well as numerous applications which utilize pulsatile flows including mixing, droplet generation, bioassay automation, and more. Given the wide range of applications, it follows that pulsatile flows are likely to become more prevalent, especially in microfluidic systems where pulsation helps overcome some of the limitation of steady laminar flows. Hence understanding the relationship between clogging and pulsation becomes increasingly valuable.

3.2.1 Abstract

This review describes the current knowledge and applications of pulsatile flow in microfluidic systems. Elements of fluid dynamics at low Reynolds number are first described in the context of pulsatile flow. Then the practical applications in microfluidic processes are presented: the methods to generate a pulsatile flow, the generation of emulsion droplets through harmonic flow rate perturbation, the applications in mixing and particle separation and the benefits of pulsatile flow for clog mitigation. The second part of the review is devoted to pulsatile flow in biological applications. Pulsatile flows can be used for mimicking physiological systems, to alter or enhance cell cultures, and for bioassay automation. Pulsatile flows offer unique advantages over a steady flow, especially in microfluidic systems, but also require some new physical insights and more rigorous investigation to fully benefit future applications.

3.2.2 Introduction

The precise manipulation of fluids at the submillimeter scale through microfluidics benefits a wide range of applications including material science, microscale physics, in vitro diagnostics, drug discovery, biotech process control, and ecological screening.[50, 77, 78, 79, 80] This potential was first realized in the development of inkjet printheads, which utilized microfabricated arrays of 10-100 m nozzles to efficiently and rapidly deliver ink droplets.[81] Their precise control, rapid actuation, and ease of automation allowed microfluidic inkjets to revolutionize the printing industry. However, it has only been over the last two decades that microfluidics has seen tremendous growth in other applications, as microfabrication technologies have become cheaper and more accessible.[50] This has opened many exciting directions for innovation and new research, giving rise to a dynamic field of microfluidics-based research.

Over this period, sophisticated microfluidic devices have emerged, demonstrating rapid cell sorting,[82] ultrasensitive analyte detection,[83, 84] monodisperse microdroplet emulsification, [85] precise micro pumping ,[86, 87, 88] and biosample purification.[89, 90] These have utilized a variety of different transport phenomena which can be broadly categorized as either capillary, pressure-driven, centrifugal, electrokinetic, and acoustic transport.[50] Regardless of the transport scheme, microfluidic devices are all characterized by submillimeter length scales, giving rise to physical relationships which differ considerably from macroscale flows. Herein lie numerous advantages which have enabled so many novel microfluidic applications, as well as some clear limitations which have made it challenging for these new applications to reach the scalability and ubiquity of inkjet printing. Many of these limitations are tied to the nature of steady laminar flow in microchannels.[91] Recent reports suggest that these limitations may be overcome using more complex unsteady flows.

Laminar flows through circular and rectangular channels can be solved analytically, while flows in more complicated geometries can be solved with high accuracy using simulation software.[92] This allows for microfluidic designs to be prototyped and fine-tuned using digital models before investing in any microfabrication. While this simplicity is desirable from a design standpoint, several challenges come with laminar transport, one of which is reagent mixing.

For a reagent or chemical species with mass diffusivity , the ratio of advective to diffusive mixing is described by the Pclet number (P). At the macroscale, mixing is generally dominated by turbulent transport. But in low Reynolds number (Re) flows, the mixing speed is controlled by the diffusivity of reagents. In a rectangular microchannel, this can result in mixing lengths larger than 1000 times the channel width.

Several inertial microfluidic strategies have emerged in the last decade, which use higher flow velocities to reach to leverage inertial effects in fluid mixing and particle transport.[93][DiCarlo2009] Another technique is to increase the channel length to ensure sufficient reagent mixing before the next microfluidic operation. However, both strategies (increasing channel length or flow velocity) incur a significant energy cost, as the necessary pressure difference scales with both channel length and velocity for incompressible flow through constant cross-section microchannels. These pressures often necessitate rigid fabrication materials such as glass and silicon [94] and pose a significant challenge for point-of-care or consumer applications due to the cost of fabrication and limited access to external high-pressure sources.[95] Another option is to depart from steady unidirectional flow and take advantage of fluid oscillations.[96]

A pulsatile flow is an unsteady flow in which any arbitrary flow property can be decomposed into a time-averaged and oscillatory component. Oscillatory flows are a specific category of pulsatile flows, having only an oscillatory component with zero time-averaged components. In the mixing problem outlined above, it is possible to take advantage of the

viscous nature of these low-Re flows, which require negligible energy to accelerate or decelerate. Instead of using the channel geometry to increase its length, using an oscillatory velocity to periodically switch the flow direction increases the effective travel distance without requiring an increased pressure.[97] This increase in effective length is just one example of how pulsatile flow has been used in microfluidics, with numerous other examples in recent literature, many of which are far more complex. The time variance of pressure, velocity, shear stress, etc. in pulsatile flows has been used for enhanced separation and mixing,[98] microdroplet pinch-off and control,[99] efficient on-chip process automation,[97, 100] and clog mitigation.[101, 102]

In addition to their added complexity for enhanced microfluidic functions, pulsatile flows also possess significant biological relevance. Nearly all macroscopic animals rely on some sort of open or closed circulatory system, through which fluid transport is driven by a pulsatile heartbeat. Indeed, many cardiovascular flows are modeled as pulsatile flows through chambers or channels.[103] Even organisms which possess no heart or complex circulatory systems, such as jellyfish, sponges or fungi, often rely on unsteady flows in their environment to circulate nutrients and waste.[104] The pulsatile environment plays a critical role in the growth, motion, and development of many cell types.[105, 106, 107] As a result, many biologists have begun to incorporate pulsatile flows in their experiments. However, the characterization of pulsatile flow in these studies is often incomplete, due to a lack of standardization for describing and controlling parameters of the pulsatile flow. As more and more studies emerge, consistent nomenclature and control strategies will be paramount in establishing the cross-disciplinary knowledge needed to fully utilize pulsatile microsystems.

This review provides a brief primer outlining some important physical phenomena in pulsatile flows, and what these mean in the context of microfluidics. It then presents a summary of the state-of-the-art in microfluidic systems which utilize pulsatile flows to

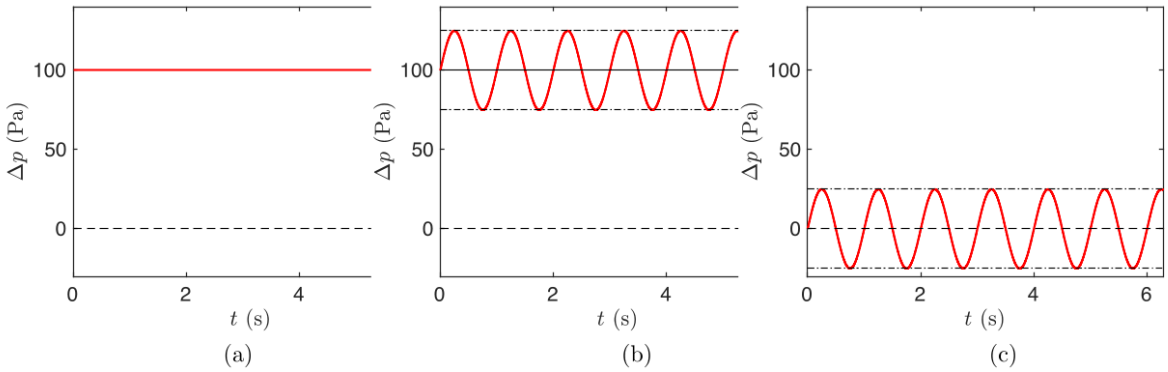

Figure 3.6: Characteristic steady and transient flow schemes. For each plot, time is represented on the independent axis, and the dependent axis represents a flow-related variable such as velocity, pressure, or shear rate. A) Steady flow has a nonzero mean value and no oscillatory component. B) Pulsatile flow has nonzero mean value, with periodic time-varying oscillations about that mean. C) Oscillatory flow has zero or near-zero mean value, with periodic time-varying oscillations about that mean.

reach new levels of functionality across a broad range of applications. Finally, this review addresses the importance of pulsatile flows in biological systems, in particular, to enhance cell culture efficacy and mimic physiological conditions in biomicrofluidic experiments.

3.2.3 Physical Description of Pulsatile and Oscillatory Flows

The majority of microfluidic systems have relied on steady flows in rigid or deformable devices. To enable new functionalities, a few studies have focused on how to leverage pulsatile flows. While steady flows are time-invariant, pulsatile flows present a new time scale associated with the oscillation of the flow. These systems are commonly driven by an external oscillating harmonic field. For example, a microfluidic flow driven by a pulsatile pressure difference Δp can be written as $\Delta p = \delta p_0 e^{i\omega t}$, where Δp_0 is the time-averaged pressure, δp denotes the amplitude of the pressure oscillation, and ω is the frequency of the oscillation.

With this expression, several different flow fields can be defined, as shown in Fig. 3.6. When the oscillation amplitude is zero ($\delta p = 0$), time variance disappears, leaving

classical steady flow (Fig. 3.6a). When $\delta p \neq 0$, two types of harmonic flow can be defined. Pulsatile flow describes the case when $\Delta p_0 \neq 0$, as shown in Fig. 3.6b. In this situation, there is an average advection of fluid particles with an oscillatory amplitude of δp and angular frequency $f = \omega/(2\pi)$ superposed on it. Oscillatory flow describes the case when $\Delta p_0 = 0$, hence fluid particles experience no net advection over time, but rather oscillate about a central position.

To characterize the influence of flow oscillations for varying microfluidic chip designs, it is also necessary to take into account the characteristics of the system. The Reynolds number (Re) describes the magnitude of inertial forces relative to viscous forces in a flow, described by $\mathrm{Re} = UL/\nu$, where U and L are the characteristic velocity and length scales respectively, while ν is the kinematic viscosity of the fluid, defined as the ratio of dynamic viscosity η to density ρ such that $\nu = \eta/\rho$. A typical microfluidic device (utilizing water as the working fluid $\nu \approx 10^{-6} m^2 s^{-1}$, average velocity $U \in [10^{-6}, 10^{-2}] m s^{-1}$, and channel width $L \in [10^{-6}, 10^{-4}] m$) possesses a range of $10^{-6} < \mathrm{Re} < 1$.[91] Therefore, viscous effects tend to dominate fluid transport in microfluidic systems, yielding laminar flows. However, Re does not contain any parameters to account for the time-varying aspects of pulsatile and oscillatory flows.

In a pulsatile environment, the fluid flow can be subjected to both viscous resistance and inertia resulting from the pulsatile nature of the system, even at low Re. This situation is different from steady flow in microchannels, where only viscous resistance is relevant. As a result, an additional dimensionless parameter needs to be introduced. The Womersley number (Wo) compares the transient inertial effects to viscous forces,[108] defined as $\mathrm{Wo} = (\omega L^2/\nu)^{1/2}$.

For $\mathrm{Wo} << 1$, viscous effects dominate, and the oscillation frequency of the flow is sufficiently small, such that the steady velocity profile has time to develop during each cycle. For instance, in a cylindrical capillary, the steady-state Poiseuille profile

is recovered at each oscillation cycle for low Wo. The opposite situation, where the oscillation frequency is sufficiently large, leads to Wo $>>$ 1 and corresponds to the situation in which the oscillatory inertial force dominates the dynamics and strongly modifies the mean flow profile. In this regime, when the pressure gradient is reversed, it takes some time before the pressure gradient can change the direction of the flow, which leads to a phase shift between the fluid flow and the pressure gradient. For instance, in blood vessels, the Womersley number typically ranges from Wo $\sim$ 15 for the larger vessels (aorta, large veins) to Wo $\sim 10^{-3}$ for the smaller capillaries.[109] Thus the flow profile for larger vessels is significantly modified and out of phase with the pressure field, while the flow profile for smaller vessels is in phase with the pressure field.

Another important aspect that neither Re nor Wo capture is the relative amplitude of oscillation $\xi = \delta p/\Delta p_0$. ξ also captures the approximate flow state where $\xi << 1$ corresponds to steady flow, $\xi >> 1$ corresponds to oscillatory flow and $\xi \sim 1$ corresponds to pulsatile flow. While this parameter is not commonly used in contemporary pulsatile studies, it completes the non-dimensional description of pulsatile flow. Re describes the laminarity of the flow, Wo describes the flow response to oscillatory forcing, and ξ describes the flow as steady, pulsatile, or oscillatory. For studies that seek to produce physiologically relevant pulsatile flows in microsystems, matching the values for Re, Wo, and ξ is thus crucial.

The analytical resolution of single-phase flow in the laminar regime can be performed in the case of a rigid microfluidic chip and has been considered, for example, to describe physiological flows. Nevertheless, the influence of flexible microfluidic channels on pulsatile flows is still an active research area that we will mostly neglect in this review, as the effects of compliance and harmonics are highly system-specific.[109, 110, 111]

3.2.4 Pulsatile Flows in Microfluidic Processes

Pulsatile Signal Generation

To drive an oscillatory or pulsatile flow in microchannels, external and internal sources can be used to generate an oscillatory signal. External inputs, such as peristaltic pumps or digitally modulated pressure controllers, are perhaps the most straightforward mechanisms for generating a pulsatile signal. Similarly, custom pneumatic channels to superpose oscillatory pressure signals over a steady flow have been used to generate complex pulsatile flows, as illustrated in Fig. 3.7.[112, 113] While simple and relatively robust, external sources require additional power and space, making them unsuitable of point-of-care or field applications. They are also limited to signal frequencies less than about 15 Hz. As a result, numerous on-chip techniques have been explored.

Generally, on-chip mechanical generation of oscillatory signals is still in early development. Asymmetric elastomeric components have been integrated into microfluidic channels to generate pulsatile flows with constant flow inputs.[114] This technique, analogous to an electronic switching circuit, requires that the device be designed as a whole to achieve the desired signal, and has only been demonstrated to reach frequencies as high as 1 Hz. Oscillator fluid circuits, which operate using a constant water-head pressure, have been demonstrated to reach frequencies as high as 10 Hz with flow rates up to 2 mL min1.[115, 116] These oscillators are unique in their ability to generate dynamic flow rates with a constant pressure source. While microfluidic applications are dominated by incompressible flows, microfluidic oscillators made of SU-8 on silicon havebeen shown to reach near-kilohertz frequencies with compressible flows.[117] Additionally, pneumatic oscillators fabricated in glass have been used to for on-chip peristaltic pumping using a constant vacuum pressure input, with demonstrated oscillator frequencies as high as 50 Hz and peristaltic flow rates as high as 14 L min1.[118]

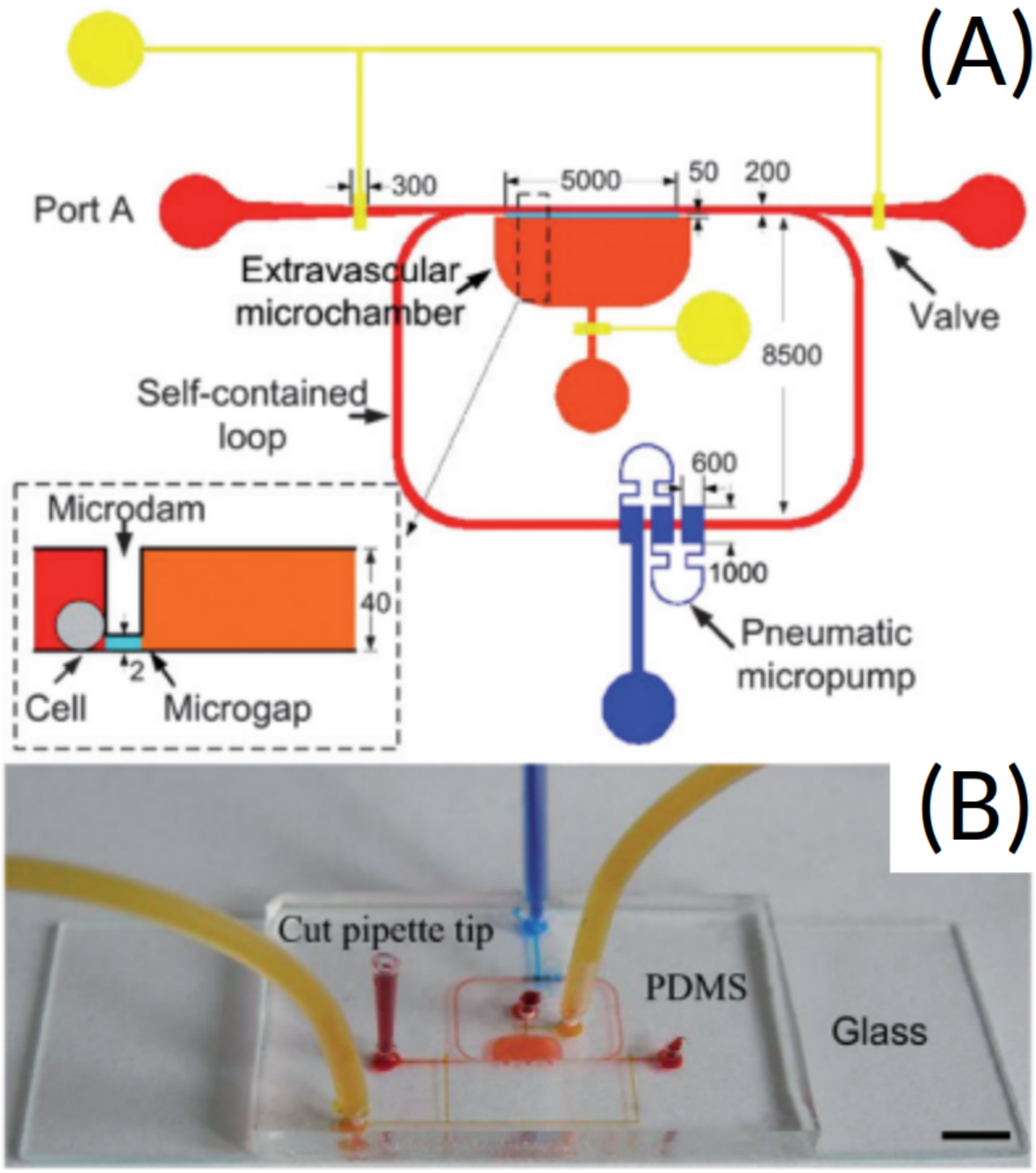

Figure 3.7: Pneumatically driven microcirculatory system. A) Illustration of the circulatory loop (in red), pneumatic micropump (in blue), and valves and extravascular area (in yellow). The exploded view shows a microgap for cell trapping. Notably, the pneumatic micropump was used to generate a pulsatile flow to recapitulate the physiological shear stress environment of endothelial cells. B) Photograph of the microcirculatory chip with dye to indicate sections outlined in the schematic, with 5 mm scale bar. Reproduced with permission.[103] Copyright 2009, The Royal Society of Chemistry.

Chemically induced oscillation of polymer gels was demonstrated in 1995,[119] in which chemical and temperature-sensitive hydrogels are subject to self-oscillatory swelling and deswelling through nonlinear chemical reactions. Just recently, this phenomenon has been leveraged in microfluidic flow control, utilizing an autonomous hydrogel oscillator to switch between on and off states corresponding to the alcohol content of the working fluid.[120] While this system has demonstrated excellent stability, with an operational life over 3 months, it has been limited to a maximum oscillation frequency of about 0.05 Hz.

On-chip pulsatile flows are commonly achieved using an oscillatory electrical signal. With origins in inkjet printing, thermal bubble micropumping uses an integrated micro-heater to drive the expansion of an attached bubble. This has been used to impose an oscillatory flow with frequencies up to 300 Hz [121] and can be performed using either Joule [122] or induction [123] heating to influence bubble expansion. Piezoelectric diaphragms have also been used to induce fluid motion over a wide frequency range.[124, 125, 83]

Electrodynamic phenomena can also drive pulsatile flows. In electrowetting, the surface energy between a fluid and dielectric-coated electrode can be manipulated using an applied potential. This is well-suited to microfluidic applications where surface tension alone can be used to drive capillary flows. Electrowetting systems are relatively simple to fabricate, requiring a single-level patterned electrode for basic functionality.[126] Electrowetting can be used to control fluid motion over the patterned electrodes with actuation frequencies in the kilohertz range,[127] with significant potential to enhance micro-scale mixing when combined with droplet-based systems.[128, 129]

Electroosmosis is an electrokinetic phenomenon, in which an electric field is used to drive the bulk flow through capillaries or microchannels. Electroosmotic flow (EOF) has the advantage of straightforward, full-channel implementation, similar to electrowetting

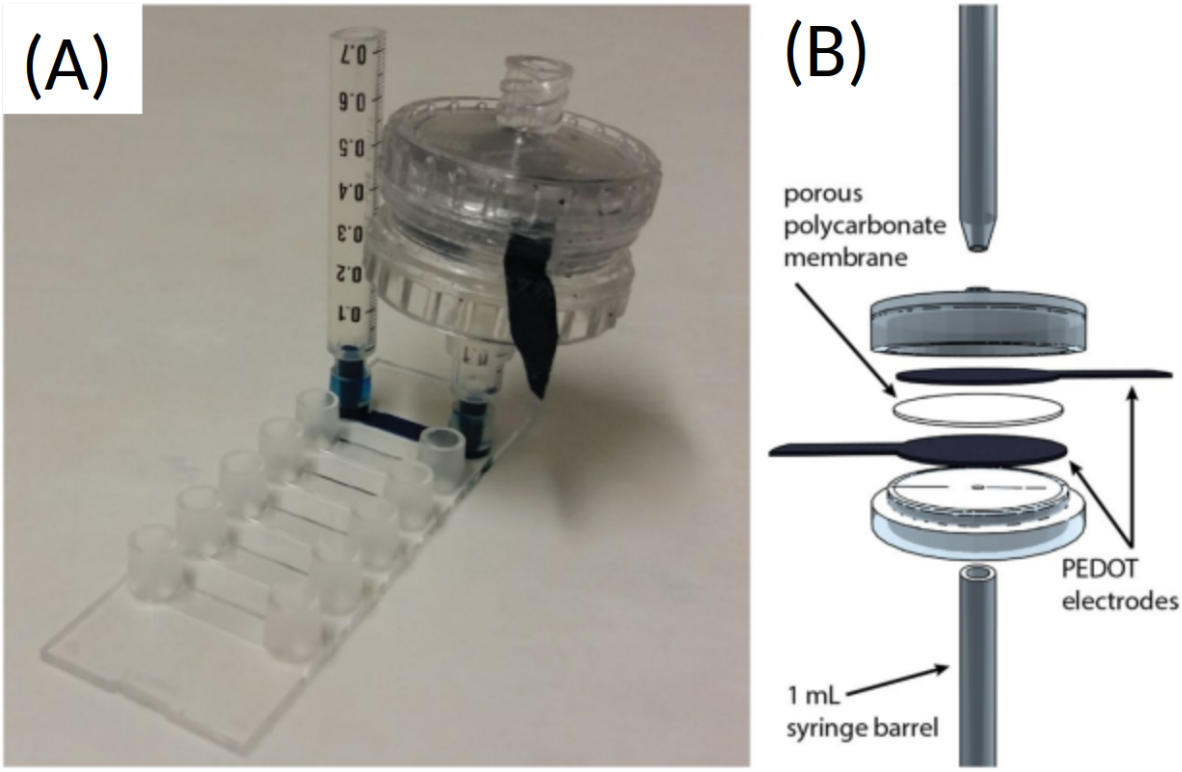

Figure 3.8: Modular clip-on electroosmotic pump for oscillating flow. A) Photograph of the pump and modified syringe filter holder attached to a simple microfluidic culture array filled with blue dye. The pump attaches with a standard Luer connector. B) Exploded schematic of the modified syringe filter holder and pump, consisting of a porous polycarbonate membrane and two poly(3,4-ethylene dioxythiophene) polystyrene sulfonate (PEDOT:PSS) electrodes. Reproduced with permission.[130] Copyright 2018, Springer Nature.

techniques. However, its sensitivity to electrochemical properties and Joule heating can limit its applicability to a variety of samples.[131] Oscillatory EOF is still in early development, with numerous theoretical studies emerging.[132, 133, 134, 135] Bengtsson et al. recently developed a clip-on electroosmotic pump with standardized Luer connectors for microfluidic cell culture devices, shown in Fig. 3.8. This device could easily be adapted for other oscillatory microfluidic flows.[130] It has the advantages of low-cost, low-footprint, and easy implementation with demonstrated oscillatory flow rates of 400 μL min^{-1} and frequencies up to 0.25 Hz.

This summary illustrates the wide variety of techniques that can be used to generate oscillatory signals, which include a mix of active, passive, external, and on-chip strategies. On one hand, this variety is advantageous for designing microfluidic systems which may operate over a wide range of flow rates or handle samples with a variety of thermal, electrical, and viscous properties. On the other hand, this variety presents a challenge in describing the effects of pulsatile flows across such a wide range of operating conditions. For instance, many of the strategies reported above focus primarily on oscillatory frequency, while only a few specifically mention mean flow rate and oscillatory amplitude. Eventually, a more complete description of pulsatile parameters will be required to compare different techniques and standardize pulsatile studies across disciplines critically.

Droplet Generation

One classical application of microfluidic technologies is droplet generation and control, which has become a versatile tool with applications in material synthesis,[136, 137, 138] high-throughput biochemical screening,[139, 140] and single-cell analysis.[141, 142, 143, 144] Droplet-based systems possess the advantages of low reagent use, scalable production of droplets, a high-surface-area-to-volume ratio which facilitates fast reactions, and independent droplet control.[145] Most applications demand high uniformity in droplet

size, but some applications require well-controlled sequences of droplets with different volumes.[99] Managing droplet coalescence is also critical in systems which use micro-droplets for encapsulation of miniature reaction volumes.[146] In any case, precise control of droplet size, formation, and motion are essential.

Early systems have utilized passive droplet generation techniques, in which constant flow rates or pressures are enforced in a two-phase microfluidic junction. The flow is driven by syringe pumps or pressure controllers, and the energy of the system is partially converted into interfacial energy which destabilizes the liquid-liquid interface and can induce droplet formation or corrugations of the jet.[85, 147, 148] Passive techniques for droplet generation rely on the spontaneous growth of Rayleigh-Plateau instabilities to trigger droplet formation.[149] While channel geometry can be used to passively induce or suppress droplet breakup,[150] pressure and flow rate are the only tunable parameters. Electric fields can also be used to influence droplet breakup of dielectric jets,[151] but requires suitable working fluids. This means passive techniques are limited in droplet size, generation frequency, and appropriate fluid choice.[148, 152] Instead, active techniques have emerged to provide additional flexibility in droplet size and production rate while also improving the system response time needed for stable droplet production.[99, 153]

Pulsatile flow is essential to numerous active droplet generation techniques. The pulsatile condition provides additional control over droplet formation, as it removes the dependence on Rayleigh-Plateau instability growth. Triggering the droplet formation with external forcing is particularly useful in generating droplets having very low interfacial tension. Such is the case for aqueous two-phase systems (ATPS).[154, 155] In this case, a constant continuous-phase input and pulsatile disperse-phase input have been used to generate monodisperse ATPS droplets ranging from 10 pL to 10 nL.[156, 157, 158, 159, 160][83-87] Notably, the pulsatile frequency (0 to 200 Hz) and amplitude (1 to 3 mm) impact the synchronization of glycerol-in-oil droplets generation.[161] Indeed,

pinch-off dynamics induced by these pressure fluctuations are highly dependent on the initial perturbations.[162]

Droplet formation can also be induced by vibrations. Using a traditional passive capillary injection coupled with an active loudspeaker and membrane, ATPS droplet generation frequencies as high as 1 kHz have been demonstrated,[164] which is roughly 100 times faster than the natural frequency for droplet formation for this system. Finally, pulsatile flows also provide additional control over the position and shape of the individual droplet in confined flows.[165] These aspects are not only directly useful in the design of droplet-based microfluidic systems, but may also shed light on the dynamical features of physiological systems, such as red blood cells in pulsatile flows.

A unique strategy introduced by Zhou et al. combines the benefits of both passive and active methods. This method involves perturbations induced by secondary oil droplets, termed choppers, to distort an adjacent aqueous surface and induce droplet formation in the aqueous phase.[163] While both the oil and aqueous phases are introduced via steady flow, the passive breakup of the high-surface tension oil jet triggers oscillatory perturbations in the aqueous jet, which leads to spontaneous active droplet formation. This was demonstrated at frequencies up to 2.1 kHz for droplet sizes ranging from 20 m to 300 m, having a coefficient of variance between 0.75% and 2.45% for droplet diameter. Oil and ATPS droplets were then separated by density in a -shaped glass capillary. The droplet generation, separation, and collection steps of this method are depicted in Fig. 3.9.

Finally, it is worth noting that pulsatile flow conditions are not always desirable for droplet generation. Periodic perturbations are useful for triggering instabilities in systems with low interfacial tension, in which the natural instability growth is slow or nonexistent. However, for systems exhibiting high interfacial tension, pulsatile forcing and natural instability growth may simultaneously contribute to droplet formation, re-

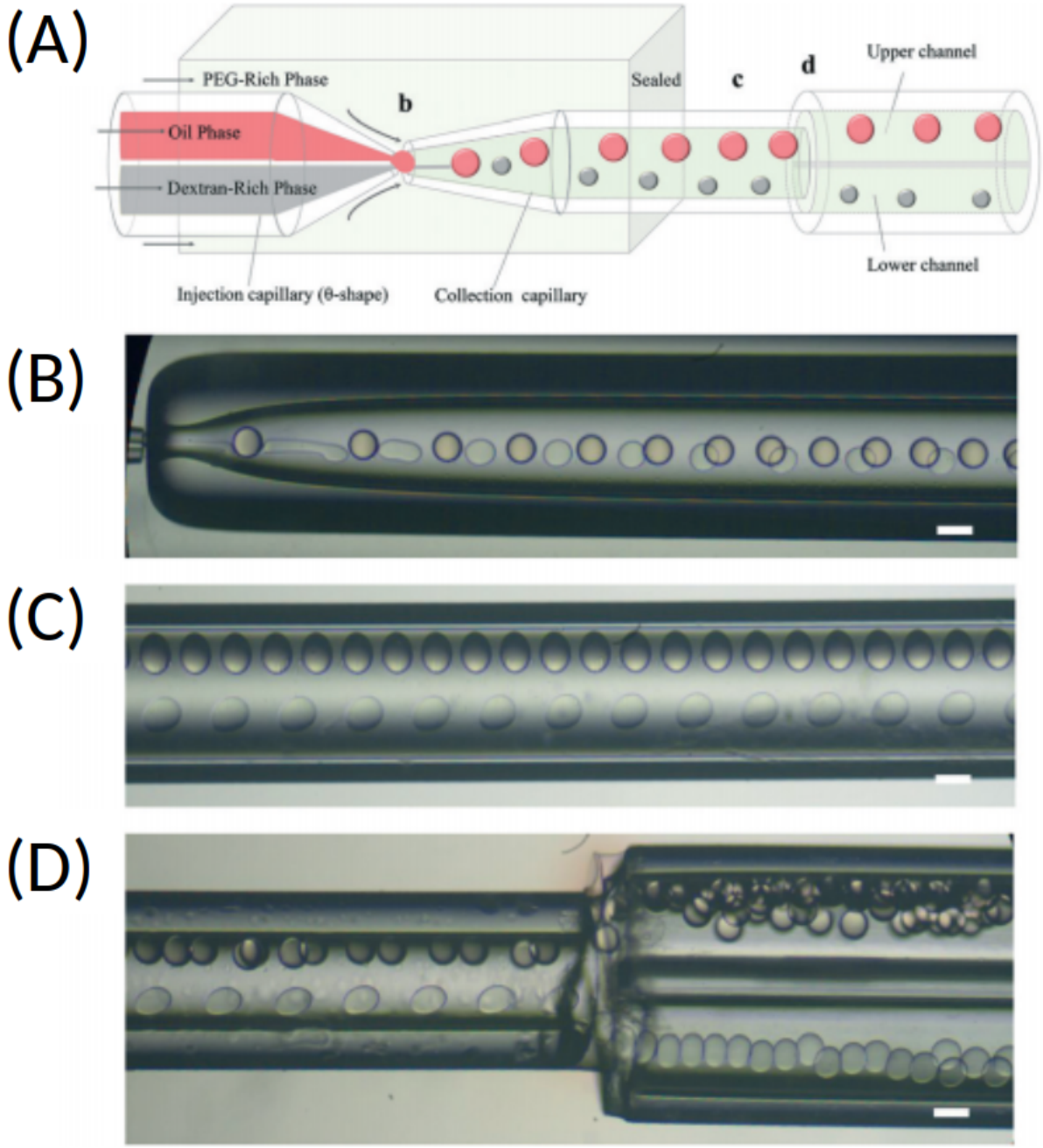

Figure 3.9: Oil-chopper based microdroplet generator. A) Illustrative schematic of device operation with the oil-phase shown in red and aqueous phase in gray. B) Pulsatile inputs to the oil-phase create oil microdroplets which perturb the adjacent continuous aqueous phase. This triggers rapid instability growth and aqueous droplet formation. C) Oil and aqueous droplets are separated by density and then D) collected in a theta-shaped capillary. Scale bars are 200 m. Reproduced with permission.[163] Copyright 2017, The Royal Society of Chemistry.

sulting in nonuniform droplets. Indeed, Li et al. visualized syringe-pump-induced fluctuations at a liquidliquid interface and suggest that these fluctuations are responsible for the 1%5% polydispersity noted in numerous microdroplet studies.[147] Thus steady, constant-pressure flows are desirable for generating monodisperse emulsions.

Enhanced Mixing

Mixing is often a crucial step in functional microfluidics, especially in material synthesis and bioassays. [98, 166, 167] Traditional microfluidic devices operate in a low-Re regime, yielding laminar flow profiles in which mixing is limited by diffusion. To improve upon this, more complex geometries in steady flow regimes can induce two-dimensional stretching and folding of fluid elements, which increases the interfacial area between segregated fluids to facilitate faster mixing. This process is termed chaotic mixing.[166] In addition to geometric elements, such as herringbone or serpentine channels, hydrodynamic focusing is also used to fold segregated fluids and enhance mixing times repeatedly.[167] Pulsatile strategies can also significantly improve mixing times, especially if coupled with other enhancements.

The simplest pulsatile mixing strategy is to add an oscillatory component to an otherwise-steady mixing interface. An early demonstration of this combined two aqueous fluids at a y-connection and used a pinch valve on each arm to generate strong pulsations, while a peristaltic pump provided the mean flow.[169] With this setup, Truesdell et al. performed a set of experiments to investigate the relative effects of pulse period, pulse width, and delay. They note that in cases of improved mixing, the mixing interface appears fractal, while the interface remains undisturbed under poor mixing conditions.

Another early demonstration was performed by Tsai and Lin, who used a thermal bubble micropump to generate an oscillatory flow in a microfluidic mixer.[122] They found that mixing of blue food dye and isopropyl alcohol improved with increasing oscillatory

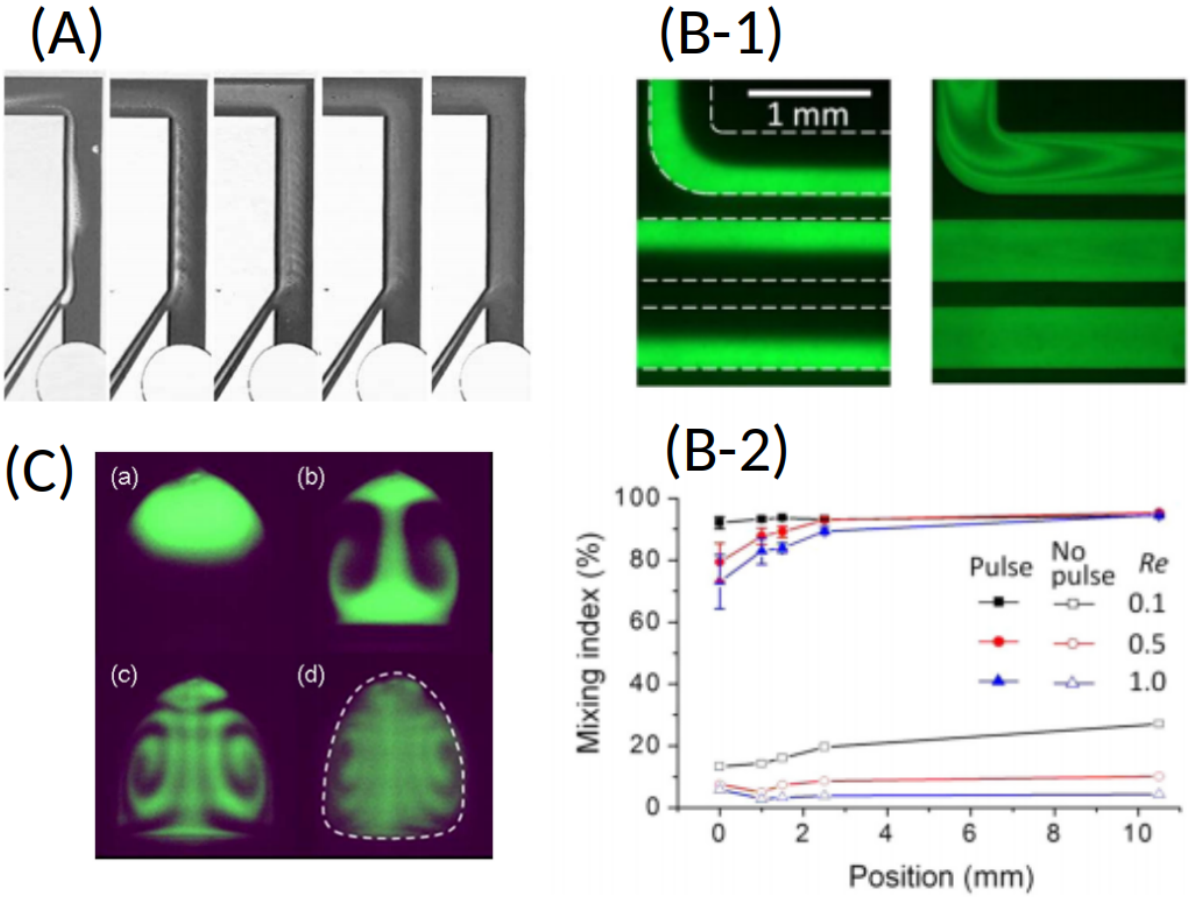

Figure 3.10: Examples of mixing enhancement by oscillatory perturbations. A) Mixing of IPA and blue dye in a microchannel improves with increasing oscillatory frequency. From left to right: 5, 50, 100, 150, and 200 Hz. Reproduced with permission.[122] Copyright 2001, Elsevier. B-1) Comparison of streamwise mixing in straight and elbow microchannels under steady flow (left) and 18 Hz pulsatile flow (right). B-2) Plot comparing the mixing index in the streamwise direction, demonstrating significantly faster mixing under pulsatile conditions. Reproduced with permission.[168] Copyright, 2016 Elsevier. C) Time-lapse of mixing in a droplet due to electrowetting-induced oscillatory motion at 81 Hz, with 0.55 s between images. Reproduced with permission.[129] Copyright 2006, AIP Publishing.

actuation frequency, with optimal mixing achieved around 200 Hz, as depicted in Fig. 3.10a.

Recently, Li and Kim presented a microfluidic device which does not rely on any off-chip dynamic controllers to achieve pulsatile mixing.[168] They used integrated valves and elastomeric membranes to generate an oscillatory signal. The authors report a five- to twenty-fold improvement in mixing index at a switching frequency of 18 Hz when compared to a steady, diffusion-limited case as summarized in Fig. 3.10b.

Depending on the sample type and additional required functionalities, several other strategies to enhance mixing with a pulsatile flow have been proposed. For example, pulsatile flows can be combined with geometry to induce rotational flows via circular mixing chambers,[170] or amplify chaotic mixing through converging-diverging nozzles[171] or cross-flow junctions[172]. Another promising technique leverages the internal convection of a confined moving droplet to enhance mixing.

A confined droplet or fluid plug, which is in interfacial contact with the surrounding microchannel, will experience internal circulation as it moves through the channel. Stone et al. developed a model which predicts enhanced mixing in a spherical droplet subject to external flows,[173] while enhanced mixing in confined droplets has been experimentally demonstrated and visualized.[174, 175] Mugele et al. added oscillatory motion to the droplet via transient electrowetting to further improve mixing speed, while also decreasing the required channel length.[129] They used an oscillatory frequency between 10 and 125 Hz to enhance mixing time by two orders of magnitude over pure diffusion in millimeter-sized droplets. The time evolution of one droplet, initially labeled heterogeneously with a fluorescent dye, is shown in Fig. 3.10c.

Mixing is a major microfluidic operation which has seen drastic improvements when enhanced by pulsatile flows. Whether through simple flow reversal to increase mixing time without increasing device footprint, high-frequency fluid oscillations to induce

chaotic mixing, or internal circulation using droplet techniques, pulsatile strategies can improve mixing times by an order of magnitude over steady flow counterparts. Nevertheless, determining the optimal oscillatory parameters has largely been an empirical process, thus there remains significant room for the development of new models to describe pulsatile mixing environments.

The applications of pulsatile flows to multiphase systems goes beyond the mixing of two liquids. The motion of particles in suspension can be altered by the addition of a time-dependent component of the flow field.

Particle Separation and Control

Particle manipulation is an enabling function for many microfluidic systems. Inert microparticles, such as those made of polystyrene, are frequently used to demonstrate particle operations including separation, concentration, and focusing.[176] Functional micro- and nanoparticles, such as magnetic or bio-conjugated beads, allow for more sophisticated particle manipulation via external fields or specific adsorption of target molecules to enhance bioassays.[47] Droplets, cells, bacteria, viruses, and even large macromolecules such as DNA[177] are all particles ranging in size from tens of nanometers to hundreds of micrometers.[178] Due to the variety of particle sizes and physical properties, manipulation cannot be achieved using the same technique for all applications, inspiring a surge in the development of passive and active particle manipulation platforms over the last two decades.[63, 46]

While the majority of microfluidic operations involving particles have been performed with a steady flow, pulsatile and oscillatory environments have enabled novel functionality. One challenging aspect of low-Re inertia-less flows is their reversibility, which must be overcome in pulsatile systems. This has been done by designing microfluidic fea-

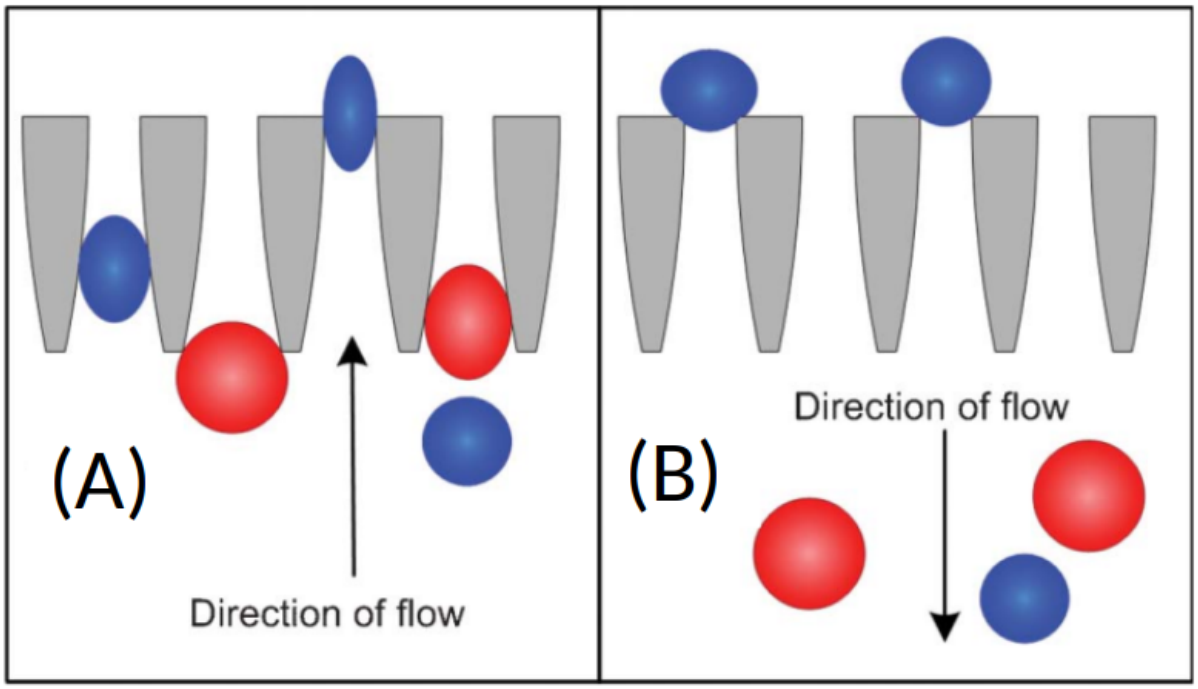

Figure 3.11: Illustration describing the operation of a microfluidic oscillatory ratchet for cell sorting. A) Under forward flow, smaller deformable particles (blue) can pass through the tapered constrictions since they are small enough to fit through the opening. Larger particles (red) cannot squeeze through. B) Under reverse flow, smaller particles are trapped, as they no longer fit through the reverse openings, while large particles flow in the reverse direction. Organizing these obstructions in an array allows particles to be separated by size under oscillatory flow. Reproduced with permission.[179] Copyright 2012, The Royal Society of Chemistry.

tures which break the symmetry of the flow, allowing for different particle motion in the forward and reverse directions.

McFaul et al. demonstrated a microfluidic funnel ratchet to separate cells based on size and deformability, as illustrated in Fig. 3.11.[179] In this device, cells pass through a network of asymmetric tapered constrictions under oscillatory flow conditions generated by a commercial pressure controller. Smaller cells can pass through the constrictions in the forward direction, while larger cells are excluded. Under reverse flow, the smaller cells remain trapped upstream, resulting in repeatable and irreversible cell sorting. The authors report a throughput of approximately 9000 cells per hour with 98% efficiency.

They separated peripheral blood mononuclear cells (PBMCs) and mouse lymphoma cells (MLCs) with a sorting area of 3.2 mm x 1.34 mm.

A similar technique was used by Cheng et al. to perform single cell capture, array, release, and labeling with a relatively simple design.[100] They used a two-dimensional trap array to filter 2 m beads from 12 m beads with 92.7% efficiency under a 1 Hz pulsatile flow, however separation of circulating tumor cells (CTCs) from whole blood was challenging due to the significant overlap in sizes of CTCs and white blood cells (WBCs). Based on similar works, CTC isolation could be improved by deformability-based separation,[180, 181, 182, 183, 184] rather than size-based separation, while still benefitting from the reduced footprint and simplicity of operations facilitated by the pulsatile flow strategy.

Recently, Lee et al. demonstrated a passive microfluidic chip capable of both particle sorting and focusing using a similar combination of asymmetric obstacles and oscillatory flow.[184] They use an array of asymmetric traps, depicted in Fig. 3.12, to uniquely influence particle migration in both the forward and reverse direction. They demonstrate size-based segregation with $> 95\%$ efficiency, solution exchange (i.e., washing), and focusing/splitting of particle suspensions on a closed fluidic circuit requiring minimal external equipment.

Oscillatory flows have also been implemented in inertial microfluidics, which perform particle focusing and manipulation in microchannels using inertial lift forces.[185] One limitation to inertial microfluidics is the strong correlation between particle size and the inertial lift force. Particles smaller than a few microns require prohibitively long channel lengths to reach their focusing position, on the order of a few meters. However, an oscillatory flow strategy enables microchannels to have an infinite effective length, enabling the inertial focusing of small particles in relatively short channels. This was demonstrated by Mutlu et al. in 2017, who used a 10 to 20 Hz oscillatory flow to focus a

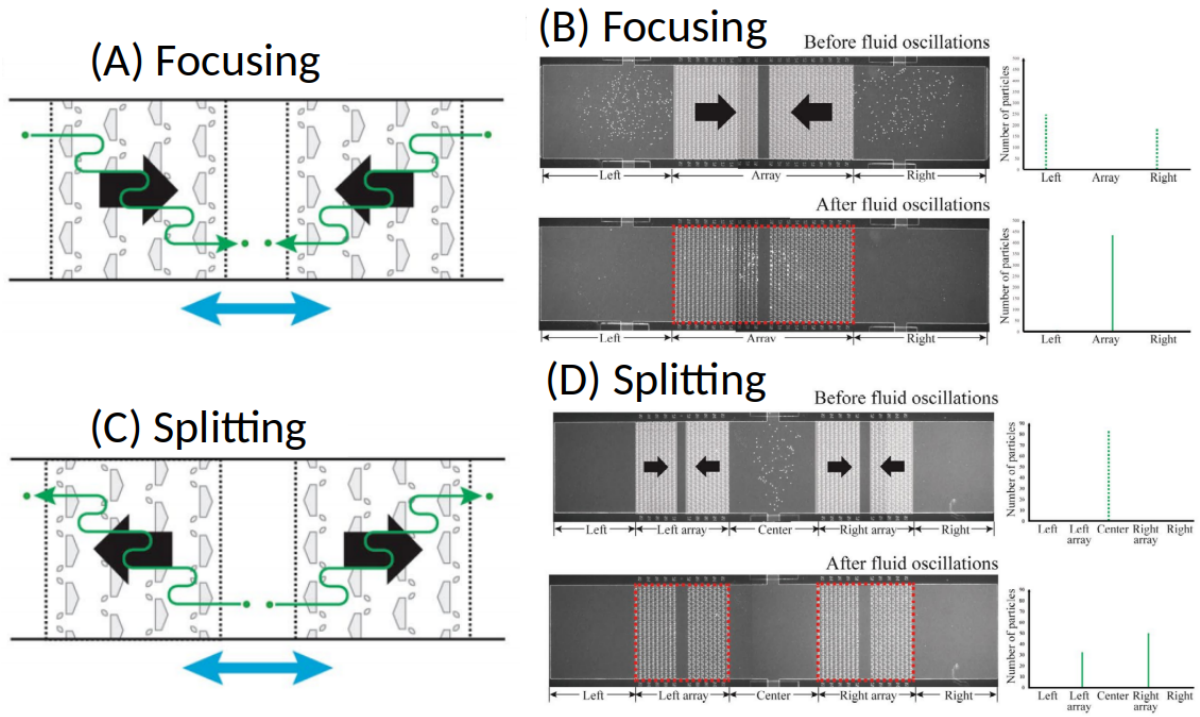

Figure 3.12: Particle operations performed in an asymmetric obstacle array under oscillatory flow. A) Illustration showing particle focusing under oscillatory flow when arrays are pointed toward the center. B) Micrographs taken before and after particle focusing, with corresponding histograms to quantify particle migration. C) Illustration showing particle splitting under oscillatory flow when arrays are pointed away from the center with D) corresponding micrographs and histograms. Reproduced with permission.[184] Copyright 2019, Springer Nature.

variety of particles as small as 500 nm in 10 seconds.[186] In addition to focusing, other modes of self-assembly are possible in oscillatory inertial microfluidic systems.[187]

In all of these strategies, a major advantage of oscillatory flows is the reduction in device footprint, since flow switching increases the effective channel length without increasing the actual physical length. The particle operations are therefore performed over an infinite effective length without incurring significant losses due to drag forces, which leads to unique operations when the forward and reverse flows are asymmetric. Additionally, many of the works reviewed above demonstrate superior reliability and claim that oscillatory systems exhibit a lower susceptibility to clogging than equivalent steady-flow techniques. This is extremely promising for high-throughput particle operations such as blood fractionation or rare-cell isolation, which are often limited by their operational robustness.

Clog Mitigation

A considerable obstacle to the commercialization and widespread use of microfluidics is their propensity for clogging. Whether due to accidental contamination with impurities or an accumulation of target particles themselves, clogging is typically detrimental to microfluidic systems, which can be prohibitively difficult to clean or reset once the flow is impeded.[58] Until this issue is adequately addressed, microfluidic platforms may continue to suffer from a low adoption rate. As a result, there has been a push to understand the complex problem of clogging at the single-pore[53, 71] and even single-particle level,[188] to better predict and model the growth of clogs.[59] All of these fundamental clogging studies have focused on steady flow, but recent reports have found that clogging can be effectively mitigated with the aid of oscillatory perturbations.

Under steady inertia-less flow, particles which become clogged are most likely to remain clogged. However, periodic oscillations can re-orient particles to delay or eliminate

the onset of clogs. For example, in the previously mentioned study by McFaul et al., the oscillatory flow was not only essential in controlling particle motion in the microfluidic chip, but also played a significant role in clog mitigation. The authors operate the system continuously for more than four hours without any degradation in functionality.[179] An oscillatory flow strategy was also used to mitigate clogging in the previously mentioned microdevice by Cheng et al., using a 1Hz pressure fluctuation as their oscillatory condition.[100][26]

In 2016, Cheng et al. demonstrated a clogging-free platform for cell separation from undiluted blood, which is highly susceptible to clogging.[189] They used a bidirectional micropump to enable reverse flushing of micropores to prevent clogging of the commercially available polycarbonate membranes. Their bidirectional flow strategy highlights the impact of oscillatory motion in clog prevention. At the same time, Yoon et al. used a piezoelectric actuator to add 130 Hz fluid oscillations to a micro-sieving system capable of size-based separation of polystyrene particles and cancer cells with 100% separation efficiently and 98% retrieval.[102] They used the same device to separate cancer cells from whole blood, during which fluid oscillations prevent the micro-sieve from becoming clogged by filtered cancer cells, allowing continuous separation with high efficiency. Partially-clogged, flowing, and filtered samples are shown in Fig. 3.13.

Another whole blood device, developed by Mehendale et al., uses a radial array of pillars and a vibration motor to achieve clogging-free operation.[101] The radial flow pattern results in dynamic cross-flow regions as certain pathways become more constricted, while the attached vibration motor helps to disturb cell clusters which would otherwise clog the array. The oscillatory frequency of the vibration motor was not explicitly discussed.

While numerous groups have noted the effectiveness of pulsatile flows in mitigating clog formation, few have quantified this phenomenon. Lee et al. performed a direct comparison between steady flow and pulsatile flow in a microfluidic chip for plasma

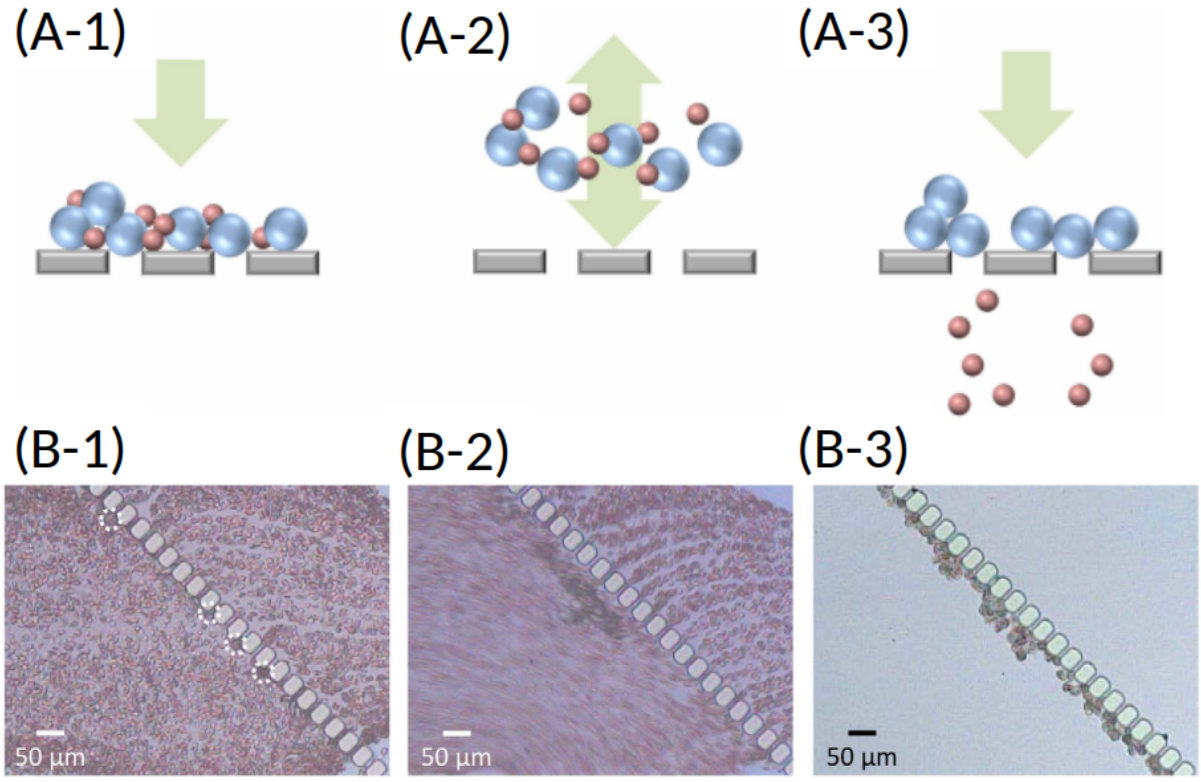

Figure 3.13: Clog mitigation via pulsatile flow. A) Illustration demonstrating the impact of pulsatile flow in clog mitigation. A-1) Small and large particles become packed against the filter, resulting in a clog. A-2) Pulsatile flow continuously clears the filter space to prevent clog formation. A-3) Small particles continue to flow through the filter, allowing large particles to be enriched. B) Micrographs of a continuous -sieve device for the enrichment of cancer cells in whole blood. B-1) A filter region which is partially clogged by a combination of cells. White dotted circles indicate the cancer cells. B-2) Clog-free sieving under pulsatile flow. B-3) Enriched cancer cells after sieving the spiked blood sample. Reproduced with permission.[102] Copyright2016, Springer Nature.

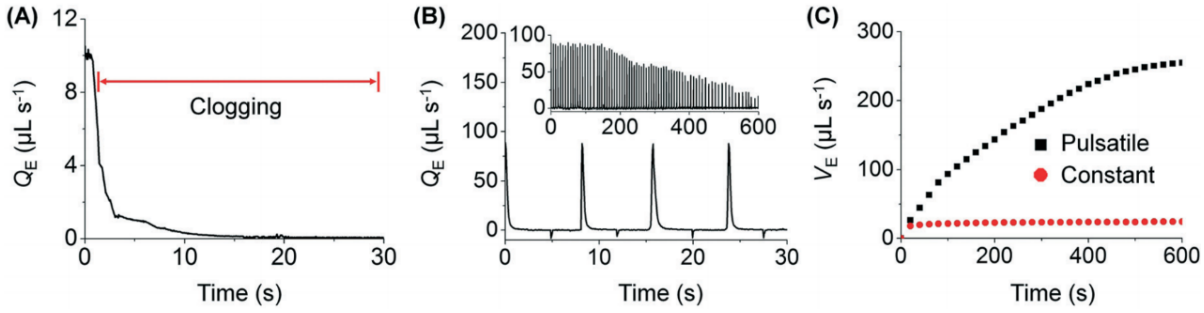

Figure 3.14: Quantitative comparison between steady and pulsatile flow performance in a microfluidic blood plasma separation device. A) Under steady flow, the plasma extraction rate drops to nearly zero L s1 after just 10 s of operation, due to clog formation which impedes the flow. B) Under pulsatile flow, the plasma extraction rate is significantly improved, maintaining a nonzero extraction rate after 600 s of operation. In (C), the total volume extracted is compared between steady (red circles) and pulsatile (black squares) flows. Due to its ability to mitigate clogging, the pulsatile case yields nearly ten times the volume of plasma in the same amount of time as the constant flow case. Reproduced with permission.[190][124] Copyright 2018, The Royal Society of Chemistry.

filtration,[190] using a water-head-driven oscillator.[115, 116, 168] They measured the extraction rate under both steady and pulsatile operating conditions, and plot the results in Fig. 3.14. Due to rapid clog formation, extraction rate is poor under steady flow, while the pulsatile flow condition yields roughly ten times the volume extracted over the same 10 min operational time.

Across these studies, we note that the oscillation frequency can vary significantly while still mitigating clog formation. Some authors have reported frequencies as low as 1Hz, and as high as 200 Hz, while some authors do not report their oscillatory parameters. Based on the works reviewed, pulsatile flows provide some benefit to clog mitigation, but there is still much to learn in terms of optimization and physical mechanisms. The dynamics of clogging and clog mitigation in microfluidic systems is still a growing topic, and a rigorous study of clogging in pulsatile systems has yet to be conducted.

Despite the current gaps in pulsatile flow mechanisms and parameter standardization, numerous groups have already used pulsatile flows for droplet generation, enhanced

mixing, particle control, and clog mitigation. These signals can be generated in a variety of ways, each with their own strengths and limitations, giving rise to a wide range of platforms. Many of these have been utilized in biological studies spanning the molecular- to tissue-level, as pulsatile flows are ubiquitous throughout living systems.[103, 104] Additionally, the range of operations enabled by pulsatile flow techniques makes them extremely attractive for the automation of standard bioassays.

3.2.5 Applications of Pulsatile Flows in Biology

Biomimicry for Physiological Studies

Biological experiments are a cornerstone to critical advancements in drug discovery, genetic mapping, and biophysics. [191] Generally, these experiments are challenging because rigorous control is difficult to achieve with living systems, hence repetition and multiplexing are heavily utilized to improve the clarity and significance of results.[192] Furthermore, they may require exotic, expensive reagents which can become prohibitive. To directly address these issues, biological experiments have now utilized microfluidic platforms for decades,[193] allowing for reduced reagent consumption and better environmental controls, such as cell localization and environment sterility. Indeed, numerous groups have taken advantage of lab-on-a-chip platforms to automate multiplex processes and generate results at an accelerated rate.[194]

The underlying assumption of these in vitro experiments is that the results offer some insight about in vivo biology. To satisfy this assumption, the in vitro models seek to mimic relevant aspects of the in vivo environment. This includes the mechanical environment of the biological system.[195] For example, endothelial cells, which line the inside of the cardiovascular system (CVS), are exposed to shear forces resulting from blood flow.[103] These forces are driven by the heartbeat and are pulsatile in nature with

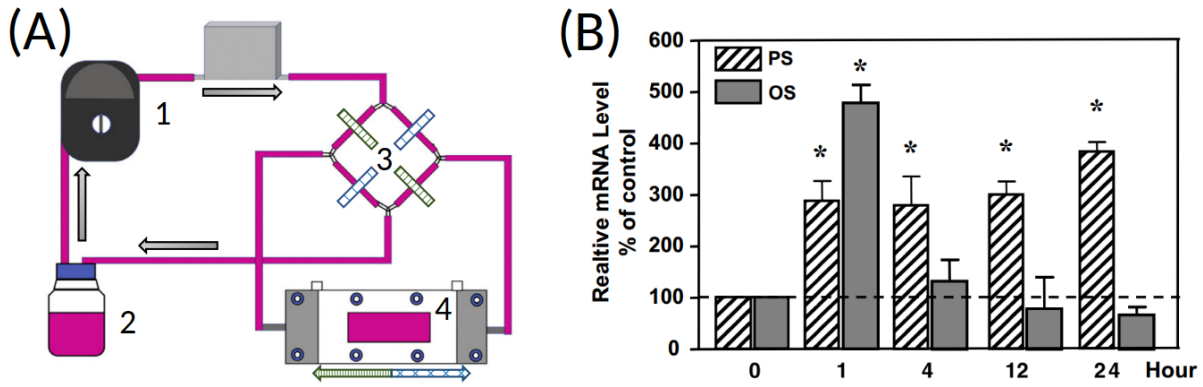

Figure 3.15: Oscillatory flow for investigating the effects of physiological shear stress on cultured endothelial cells (ECs). A) Illustration of an oscillatory parallel plate flow chamber. The pump 1) draws fluid from the reservoir 2) at a constant speed. Directional control switches 3) are used to open and close hoses, generating a pulsatile flow through the perfusion chamber 4). Reproduced with permission. [135] Copyright 2019, Elsevier. B) Flow-pattern specific regulation of Krppel-like factor 2 (KLF2) in ECs exposed to either pulsatile flow (PS) or oscillatory flow (OS) compared to the static control. The horizontal dashed line represents KLF2 expression in the static control group, while PS and OS levels are normalized as a percentage of the static control. RNA samples were isolated at 0, 1, 4, 12, and 24 h after exposure to pulsatile or oscillatory flow and quantified via real-time RT-PCR. Reproduced with permission.[200] Copyright 2006, Elsevier.

Wo ¿ 1 in many regions of the CVS. Therefore, steady flow is insufficient in recapitulating the stress environment of many endothelial cells, and there has been significant interest in capturing the pulsatile nature of cardiovascular flows.[196, 197] Shear stress was experimentally determined in vivo in 1980, using the feline mesentery as a model system spanning a wide range of vasculature levels at a scale similar to that of a human.[198, 199] Pulsatile microfluidic environments can hence be tuned to mimic in vivo conditions and provide greater physiological relevance.

Using a pulsatile flow chamber, Chien et al. compared endothelial cell (EC) gene expression and morphological changes under steady, oscillatory, and pulsatile flow conditions.[197] While the authors used an oscillatory pump to generate various pulsatile flow conditions, it is also possible to convert a steady flow perfusion system into a pulsatile system using a set of switches to periodically redirect flow, as illustrated in Fig. 3.15a.[201] Using

similar techniques, numerous groups have demonstrated a variety of mechanical feedback mechanisms which yield distinct responses under pulsatile flow conditions.[197, 201, 202] In 2006, Wang et al. showed that expression of Krppel-like factor 2, which is essential to EC differentiation and development, is different under static, oscillatory, and pulsatile flow condition, reported in Figure 10b.[200] Similar experiments have demonstrated that endothelial cells respond to oscillatory shear stress with increased expression of miRNA-663[203] and Toll-like receptor 2 (TLR2),[204] both of which are highly associated with an inflammatory response. Therefore, mimicking the pulsatile nature of cardiovascular flows is essential to understanding inflammatory diseases like atherosclerosis and even aneurysm progression.[205] Numerous cardiovascular organ-on-a-chip (OOC) platforms have emerged over the past decade, and have just recently begun incorporating complex flows to emulate the in vivo stress environment.[206]

Physiological pulsatile flows are not limited to the cardiovascular system. Eyes are coated by a thin film of tears, which is subject to an oscillatory flow generated by blinking. Blinking helps to clear debris from the cornea, as well as redistribute tears to maintain hydration.[207] The oscillatory shear forces associated with blinking may also be an essential signal for corneal epithelial cell growth and maintenance. Corneal epithelial cells were grown under static, steady, and oscillatory conditions, then compared using a combination of scanning electron microscopy and immunofluorescence. Cells grown under oscillatory conditions exhibit drastic differences in cell morphology and expression of cell junctions when compared to steady flow and static control.[208] This emphasizes the importance of accurately capturing the transient shear environment when modeling ocular surface pathology, especially when tear film may be compromised, such as with contact lenses or chronic dry eyes. Other time-varying signals in human systems include pulsatile glucagon stimulation of liver cells, periodic hormonal regulation, neuronal signaling, and more.[209, 210, 211] In these cases, chemical stimulation is pulsatile in nature, and can

be facilitated in vitro using pulsatile flow systems.[212]

Oscillatory flows emerge in many other natural settings as well, which may require translation to microfluidic platforms for simplified study. Tidal environments are inherently subject to oscillatory forcing from waves, as well as long-term oscillations in their local environment as the sea waxes and wanes. This has an extreme impact on the spacial heterogeneity in coastal aquifers[213] and the lifecycle and feeding habits of benthic organisms.[214] Many of these marine animals are microscopic and use small hair-like filaments called cilia to sense their environment and capture food particles. These cilia generate micro-pulsatile flows to pump food particles toward them, which has inspired several groups to model synthetic oscillating cilia for microparticle capture[215] and asymmetric oscillatory signal generation.[216] Additionally, many microswimmers rely on asymmetric oscillatory forcing to move through their environment.[217, 218] Platforms which can precisely control oscillatory force environments are essential in studying these diverse organisms and interactions. The initial efforts toward the development of such platform have focused on cell culture, in which a single species or community of cells are grown under controlled conditions. When these organisms are sensitive to shear stress, the nature of their flow environment can affect their growth and proliferation; hence, pulsatile flows have seen increased use in cell culture protocols.

Enhanced Cell Culturing

Many early efforts in recapitulating physiologically relevant cellular environments have focused on cell culture, in which a single species or community of cells are grown under controlled conditions. Cell culture is a fundamental component of biomedical research, enabling the investigation of cellular and molecular mechanisms, pharmaceutical development, and regenerative medicine.[219] Naturally, there is a demand for miniaturizing the cell-culture environment using microfluidic technologies to reduce media

consumption, improve sterility, and provide greater control.[220] In particular, microfluidics enables the precise manipulation of shear forces experienced by cells, with well-characterized and highly repeatable flow profiles. For many cell lines, the shear stress environment significantly affects cell growth and development.[196, 197, 221] Therefore, oscillatory flows may better mimic physiological flow conditions, giving rise to improved cell proliferation and viability.

It is well-understood that endothelial cells (ECs) possess mechanosensitive feedback mechanisms which are highly sensitive to the shear flow environment.[222] Depending on the mean shear stress and oscillatory shear stress, the feedback mechanisms can bolster or impede endothelial cells growth. Generally, a pulsatile environment with relatively high mean shear stress has demonstrated positive effects on endothelial cells growth, while oscillatory environments are correlated with inflammation and disordered cell morphology.[113] But endothelial cells are not the only cell type to respond to pulsatile culture systems.

Bone tissues are also subject to a periodic mechanical loading, and the fluid shear stress induced on bone cells in vivo is dynamic in nature. Bone marrow stromal cells possess the stem-cell-like ability to differentiate into bone, cartilage, adipose, and hematopoietic supporting tissues based on chemical and physical differentiation cues.[223] Oscillatory techniques benefit the culture of these cells for regenerative therapies. Human marrow stromal cells subject to pulsatile flow in parallel plate flow channels exhibit increased proliferation and intracellular Ca2+ mobilization.[224] Similarly, mouse osteoblast-like cells exhibit significantly improved viability and proliferation uniformity under pulsatile flow conditions when compared to steady and static flow conditions in 3D culture, as illustrated in Fig. 3.16.[149]

The optimization of cell culture has great importance beyond cellular studies. Tissue-engineered parts for regenerative medicine require hemodynamic conditioning to ensure

healthy tissues with enhanced mechanical strength and viability.[225] Therefore, numerous bioreactor strategies have begun to incorporate dynamic techniques for cell culture. These include rotational seeding and growth of vascular myofibroblasts onto tubular scaffolds to replace blood vessels,[226] as well as pulsatile bioreactors for aortic heart valve formation.[227]

Automation of PCR and Other Bioassays

Polymerase Chain Reaction (PCR) is a nucleic acid amplification technique heavily utilized in biomedical research and forensic investigations.[229] Multiplex PCR enables the amplification of several distinct DNA templates in the same reaction volume, which reduces the total time and effort required.[230] Most conventional PCR systems rely on macroscale thermal cycling, which can take 2 3 hours for a 30 40 cycle amplification, due to the overall thermal mass and large diffusion lengths. To improve cycle time, microfluidics-based PCR devices have emerged.

Stationary microchamber PCR is a miniaturized analog to conventional PCR. The PCR solution is kept in a stationary well while a micro-heater performs the thermal cycling steps. This system still requires some optimization of thermal mass to minimize reaction times and power consumption.[231] Continuous-flow PCR utilizes pumping to drive the PCR solution through several isolated reaction zones, which improves the temperature transition rate and reaction time. However, continuous flow reactors lack cycle time and cycle number flexibility.[232] Oscillatory flow PCR reactors have been developed to address all of these shortcomings.

Oscillatory PCR reactors also use a moving sample, which can be either single-phase or droplet-based, but modulate the flow speed and direction in an oscillatory manner as illustrated in Fig. 3.17. This allows individual reaction zones to be utilized repeatedly, which adds flexibility in accommodating amplification cycles while maintaining a simple,

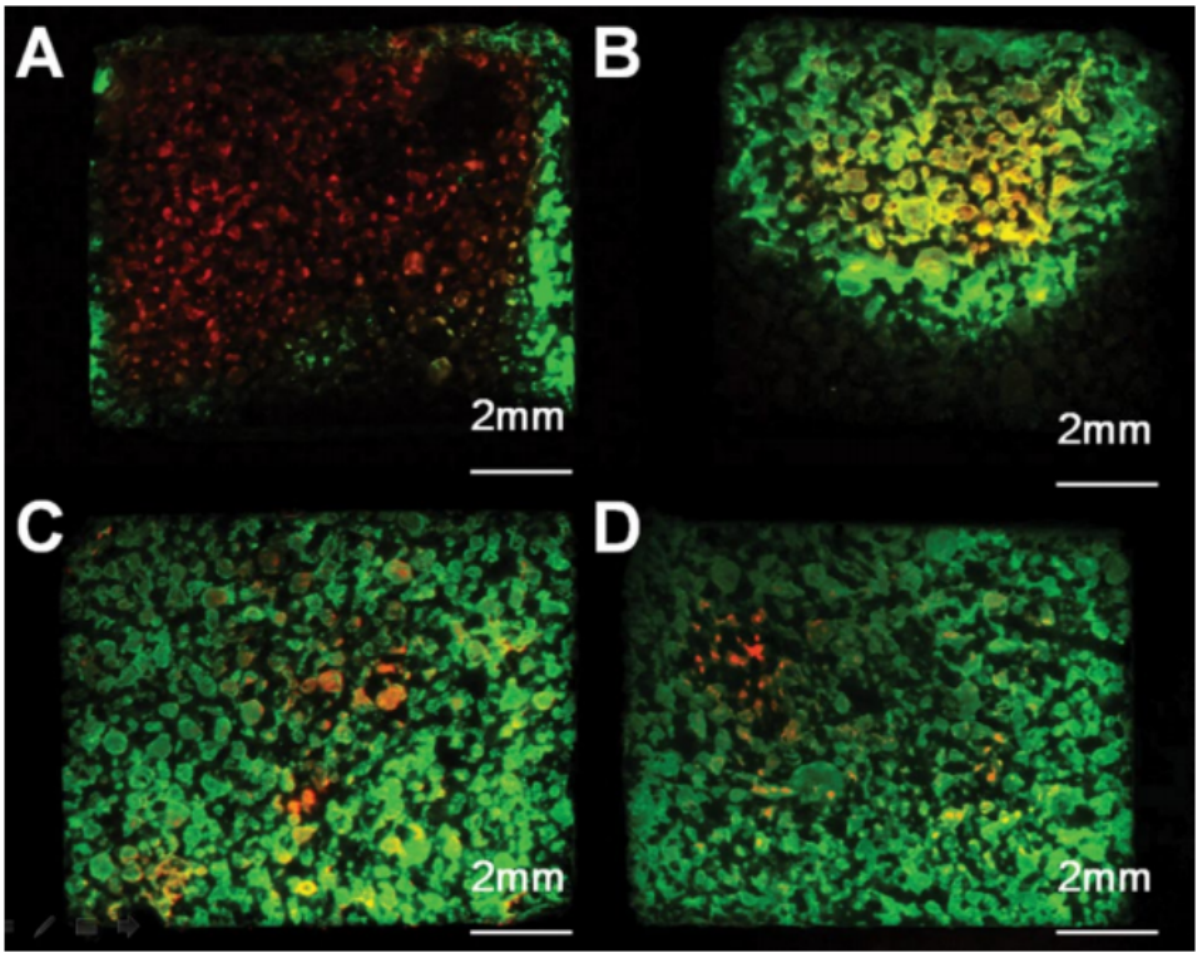

Figure 3.16: Effects of oscillatory shear stress on osteoblast-like cells. Cells are stained with Calcein-AM to indicate live cells (green) and propidium iodide to indicate dead cells (red). Each frame represents a different flow condition: A) static culture, B) steady perfusion at 1 mL min1, C) pulsatile perfusion at 0.5 mL min1, D) pulsatile perfusion at 1 mL min1. Both pulsatile cultures exhibit superior cell proliferation and viability compared to the static and steady flow cultures. Reproduced with permission.[228] Copyright 2009, Wiley Periodicals Inc.

compact platform. These advantages have allowed for simultaneous detection of multiple bacterial pathogens in just 15 minutes, with detection limits comparable to that of conventional PCR. [233, 234, 235] Oscillatory flow reverse transcription (RT) PCR reactors, which utilize an additional enzyme to amplify RNA targets, have also demonstrated similar rapid process times as low as 15 minutes. [236]

With clear advantages in processing speed and footprint reduction, oscillatory flow PCR reactors still have room to grow in complexity and robustness. For example, many of the groups mentioned above have neglected multiplex thermal protocols for PCR, as the annealing temperature for each PCR reaction may be different depending on the template and primer pairs. Nie et al. have addressed this by using microheaters and temperature sensors integrated on a silicon substrate and parallel microchannels fabricated in glass or PDMS laminates.[237]

Oscillatory PCR systems will benefit from additional technologies which incorporate sample preparation and real-time detection on-chip. Naturally, these platforms will synergize well with other pulsatile bio-environments used for physiological studies and cell culture, as PCR and RT-PCR are extremely valuable tools for obtaining direct information about gene expression in cells. With growing evidence that highlights the importance of transient stresses in many cells types, combined with all of the functional benefits demonstrated thus far, progress in pulsatile signal generation and pulsatile flow operations will continue to enable physiologically-relevant studies and bioassay automation in microsystems.

3.2.6 Conclusions and Perspetive

Microfluidic devices have been increasingly used over the last two decades to take advantage of several attributes that come with miniaturization. Ideally, their small foot-

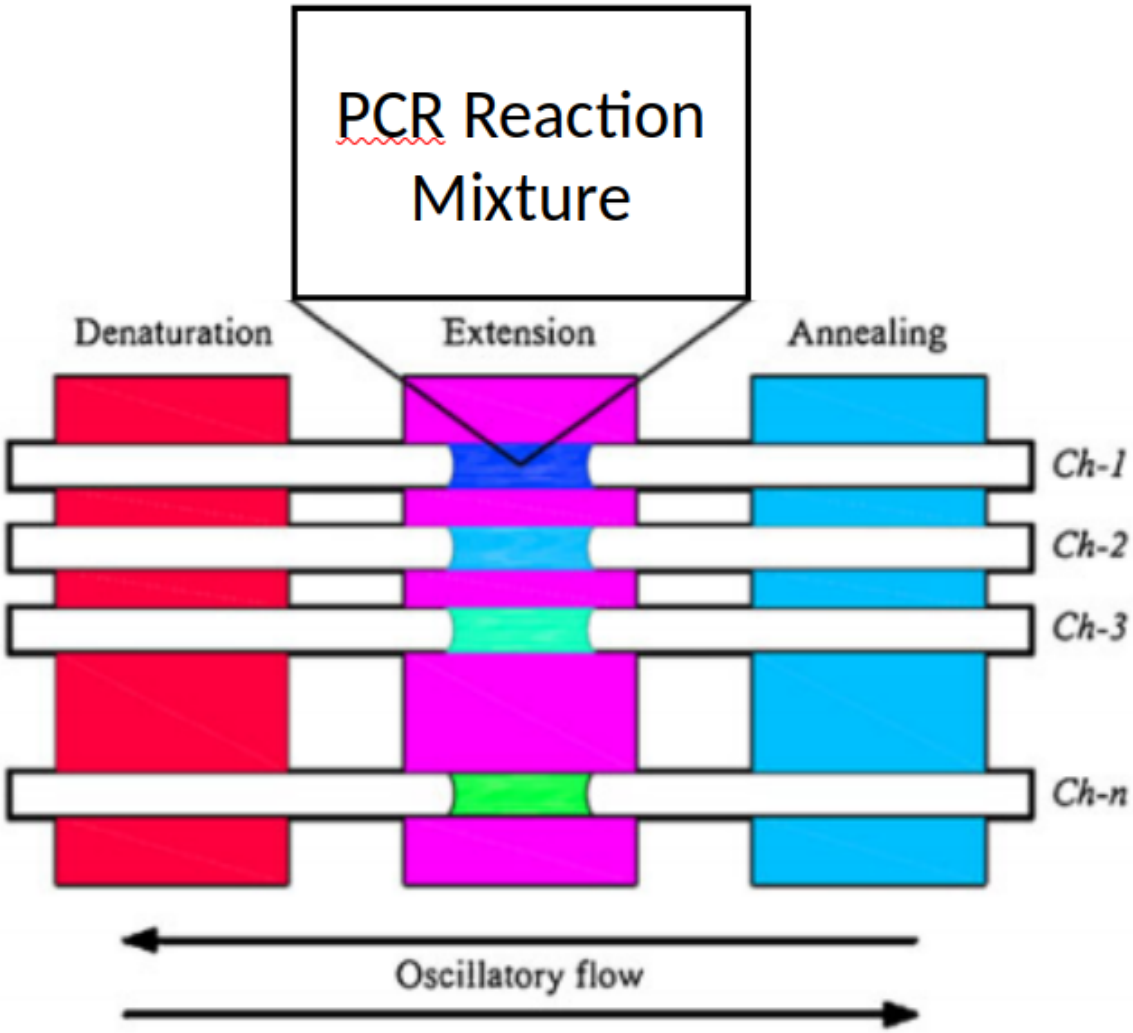

Figure 3.17: Illustrative schematic of an oscillatory PCR chamber. PCR mixtures, consisting of primers and DNA templates, are represented by the colored droplets along the center. N channels can be aligned in parallel over the three constant-temperature reaction zones for denaturation, extension, and annealing for multiplex testing. Each channel can be controlled with an independent pressure source, enabling different PCR recipes which correspond to different PCR mixtures. This strategy allows for any number of thermal cycles without increasing the device footprint, while also ensuring reaction homogeneity through mixing induced by oscillatory droplet motion. Reproduced with permission.[232] Copyright 2011, Springer Nature.

print and multifunctionality allow for portable use with minimal user experience. Their sub-millimeter scale often results in low-Re flows, which can start and stop almost instantaneously with high repeatability. Micron-scale features allow for precise manipulation of micron- and submicron-scale particles, such as red blood cells, cancer cells, bacteria, viruses, and designer micro- and nanoparticles. But microfluidic devices also suffer from their own set of unique challenges, some of which may be overcome using pulsatile or oscillatory flows. Many studies have emerged which demonstrate oscillatory enhancements in mixing, low interfacial tension droplet generation, particle manipulation, and clog mitigation. Additionally, recent biological studies have focused on the incorporation of pulsatile flows to improve the physiological relevance of in vivo system, enhance cell cultures, and automate bioassays such as PCR. However, a great deal of these studies has also left many open questions to be addressed with future work.

A distinct lack of turbulent transport in low-Re flows means that mixing of heat, momentum, and chemical species is limited by their respective diffusivities. Mixing by diffusion can be prohibitively long; thus, tremendous effort has been spent on improving mixing times in microfluidic systems. Recently, we have seen numerous oscillatory techniques which can be easily combined with existing chaotic mixing strategies to significantly enhance mixing time. This is particularly beneficial in the automation and rapidization of bioassays, which often rely on mixing for chemical labeling and thermal cycling.

The dominance of interfacial effects at the microscale has enabled an era of precise droplet generation and control. Aqueous two-phase system (ATPS) droplets are desirable for their extreme biocompatibility, which makes them ideal platforms for cell encapsulation[238] and biomolecule delivery.[239] However, stable generation of ATPS droplets is challenging under steady flow, as Rayleigh-Plateau instability growth is slow with low interfacial tension. The addition of oscillatory perturbations has been demon-

strated to remove the dependence on passive instabilities, allowing for ATPS droplet generation at frequencies as high as 2 kHz, spanning a wide range of droplet volumes.

The challenge of clogging has always plagued microfluidic systems, especially when handling complex samples such as whole blood. As a result, many microfluidic functionalities are only demonstrated with highly controlled samples, such as microbeads in water. Eventually, clog formation and clog mitigation must be understood to facilitate the development of robust microfluidic systems, which can be successfully operated without clogging outside of the laboratory environment. Several groups have recently utilized a variety of pulsatile flow strategies to periodically reset particles and delay or prevent the onset of clogging. These strategies vary tremendously in their oscillatory parameters, indicating that almost any significant oscillatory input may reduce clogging susceptibility.

The applications of mixing, droplet generation, particle control, and clog mitigation have made oscillatory microfluidics an ideal platform for cell manipulation and miniaturization of bioassays, such as PCR. Additionally, pulsatile and oscillatory flows themselves are desirable for developing physiologically relevant models in which in vivo oscillatory conditions are significant, such as the cyclic stresses experienced in blood flow and bone loading. Indeed, we have seen that adding oscillatory conditions to traditional cell culture systems can alter cell growth and proliferation, demonstrating the importance of oscillatory control when optimizing culture protocols or investigating the impact of oscillatory stresses in vitro.

With all of these applications emerging in the last decade or so, pulsatile microfluidics is still in its infancy. The move from steady to pulsatile input conditions increases design complexity in several respects. The addition of oscillatory frequency and amplitude represent two additional control parameters which affect the transient flow profile and overall system functionality. The influence of harmonics, especially in compliant

systems such as those made of PDMS or other elastomers, means that these oscillatory parameters are coupled with the system itself. This complicates the design process, as harmonic effects can alter effective impedance and damping force at the microscale must be considered. Measuring, controlling, and reporting these parameters will be essential in the development of broadly-applicable pulsatile theories.

As new applications emerge, developing a more thorough understanding of pulsatile systems will greatly benefit microfluidics as a whole. Microfluidics has recently experienced a push toward modularity[240, 241, 242] to improve adoption rate by decreasing the need for custom lithographic devices. This presents an excellent opportunity for designing modular fluid oscillators, which eliminate the dependence on outside equipment to generate the oscillatory signal. However, given the complexity of pulsatile flows in microsystems, fundamental characterization and optimization of oscillatory parameters for the applications mentioned in this review represent an essential step in standardizing the implementation of modular microfluidic oscillators. With that established, simplified inclusion of pulsatile flows in microfluidic systems will contribute to a new era of functionality and reliability, which will greatly benefit existing microfluidic assays and processes, and help enable the widescale development and commercialization of microfluidic solutions.

Chapter 4

Clogging under Pulsatile Flow

This next chapter focuses on the specific observations of pulsatile clog mitigation with an emphasis on relevant parameters —the pulsatile amplitude and the pulsatile frequency. This study aimed to evaluate a broad range of pulsatile parameters, while capturing specific mechanisms for clog mitigation in an unsteady shear environment. This study is comprised of 4 primary components:

1. First, an understanding of clogging in steady flows is established through a series of experiments. We use a micro array containing numerous parallel channels, which resembles a quasi-2D filter. We flow a dilute suspension of microparticles through the array and detect the formation of clogs in two ways: Visually, by observing the temporal buildup of particles in the array using the microscope and attached camera. And hydrodynamically, by measuring the real-time flow rate through the array using an in-series flow sensor.

2. Next, we connect these two separate clogging observations (visual and hydrodynamic), based on knowledge of our system. We demonstrate that individual clogging events can be inferred based on a local reduction in flow rate, which allows us

to ascribe clogging events to averaged data sets across multiple experiments.

3. We repeat the same experiments as above, with the same mean pressure, initial flow rate, and suspensions. But this time, we use a pulsatile pressure waveform rather than a steady pressure input. We proceed to record clogging in the same manners as before, and then compare our observations to the steady experiments. We find that pulsatile flows can reduce the clogging rate when compared to steady flows, based on proper selection of the pulsatile frequency and amplitude. However, there are inappropriate choices as well, which may have no impact on clogging or even accelerate clogging when compared to steady flows. We find that, like many systems, the clogging of this micro array is largely driven by sieving of rare aggregates, which can be modeled a Poisson process, after an initial monolayer deposition of particles at each constriction. We show that pulsation lowers the probability of clogging when compared to steady flows under this model.

4. Through time lapse images and supplemental video recordings, we document specific mechanisms for clog mitigation witnessed in pulsatile flows. These include periodically eroding particles under high shear conditions, shifting the filter cake to improve porosity and restore flow, and even complete removal of existing clogs with a high enough pressure fluctuation. We also note an instance of clog acceleration observed in the case of flow reversal —when the pulsatile amplitude is so high that the flow periodically changes direction.

Overall, this study highlights that clog mitigation can be achieved through pulsatile flows, but the choice of pulsatile parameters is highly dependent on the system. For some systems, such as filtration systems resembling our micro array, flow reversal may be undesirable. Additionally, the pulsatile frequency must be tuned to the average clogging

rate of the system, which can be hard to assess for large systems. If the frequency is too low relative to the rate of clog formation, there will likely be no benefit.

This study also illuminates several specific mechanisms for clog remediation, each of which is worthy of further investigation to better understand how and where they can be utilized at-scale.

4.1 Clog Mitigation in a Microporous Array via Pulsatile Flows

4.1.1 Abstract

Clogging is a common obstacle encountered during the transport of suspensions and represents a significant energy and material cost across applications, including water purification, irrigation, biopharmaceutical processing, and aquifer recharge. Pulsatile pressure-driven flows can help mitigate clogging when compared to steady flows. Here, we study experimentally the influence of the amplitude of pulsation $0.25\,P_0 \leq \delta P \leq 1.25\,P_0$, where P_0 is the mean pressure, and of the frequency of pulsation $10^{-3}\,\mathrm{Hz} \leq f \leq 10^{-1}\,\mathrm{Hz}$ on clog mitigation in a microfluidic array of parallel channels using a dilute suspension of colloidal particles. The array geometry is representative of a classical filter, with parallel pores that clog over time, yielding a filter cake that continues to grow and can interact with other pores. We combine flow rate measurements with direct visualizations at the pore scale to correlate the observed clogging dynamics with the changes in flow rate. We observe that all pulsatile amplitudes at 0.1 Hz yield increased throughput compared to steady flows. The rearrangement of particles when subject to a dynamic shear environment can delay the clogging of a pore or even remove an existing clog. However, this benefit is drastically reduced at 10^{-2} Hz and disappears at 10^{-3} Hz as the pulsatile timescale becomes too large compared to the timescale associated with the clogging and the growth of the filter cakes in this system. The present study demonstrates that pulsatile flows are a promising method to delay clogging at both the pore and system scale.

4.1.2 Introduction

Clogging is a multiscale phenomenon present in nearly all confined suspension flows. Depending on the suspension properties and constriction geometry, suspended particles can deposit at a constriction, forming an aggregate that grows over time. The particles can also form a bridge, or even directly sieve the constrictions.[58] Clogging and the resulting growth of the filter cake reduce the permeability of the constriction, substantially reducing the flow rate at a given pressure.[59] Clogging can be dangerous, manifesting in life-threatening conditions like thrombosis,[243, 244] or natural disasters like flooding.[245] Clogging is also a significant issue in water management, affecting critical applications like groundwater recharge, [246, 247] irrigation, [248, 249] and desalination.[250] Besides, the clogging of colloidal microplastics is becoming increasingly important, as they are heavily utilized in biopharmaceutical manufacturing [251, 252, 47] and are an increasing environmental threat due to the erosion of plastic pollution.[253] Furthermore, systems which have fully clogged and thus have a flow rate close to zero are often prohibitively challenging to unclog, and require a significant energy or material cost to restore. Changing a filter or backflushing a pipeline both require temporary inoperation of the system which they are a part of, as well as labor and materials to remedy the clog.

Clogging mechanisms are categorized according to the scenarios from which they arise. The nature of clogging mainly depends on the particle size d, the constriction size L, the volume fraction of the suspensions, and can also depends on the geometry of the channel.[58, 57] Sieving describes the scenario in which $L < d$, thus particles cannot pass through the constriction. This is often the goal in filtration where particles above a certain size threshold determined by the filter pore size L are removed. Sieving is typically the final event occurring in most clogging scenarios. [254, 255] Bridging

describes when several particles simultaneously arrive at a constriction and form a bridge due to geometric confinement. Bridging can rapidly block a constriction, but typically only occurs for concentrated enough suspensions when $L/d \lesssim 3$ for non-adhesive and rigid spherical particles.[71, 256, 257, 258] Aggregation describes the successive deposition of suspended particles at a constriction, driven by particle-wall interactions.[53, 259, 260, 188] Aggregation allows even large constrictions with $L \gg d$ to become clogged over time as small particles deposit and shrink the constriction, increasing the probability of other clogging mechanisms.[261] Overall, the clogging of practical systems often involves a combination of the three mechanisms.

Currently, clog prevention is primarily handled in two ways.[266, 267, 268, 269] The first approach is to rely on an upstream filtration, wherein particles are captured at a known, accessible location upstream of susceptible constrictions. A second common approach is to rely on chemical addition, wherein acids, bases, or biocides like chlorine are used to eliminate suspended particles or aggregates.[270, 271] However, both of these techniques have clear disadvantages. Upstream filtration prevents clogging later down the line, but filters themselves may clog relatively quickly, and filter replacement has a cost. Chemical addition is limited by the material properties of the system, and comes with the long-term risks of altered biodiversity [272] and chemical invasion [273] into

Reference	Frequency (Hz)	Amplitude	Main clogging mechanism	Geometry	Application
Jackson *et al.* (1987)[262]	10^{-4}	$800\%\, P_0$		Single pores	Irrigation
Bichara *et al.* (1988) [263]		$200\%\, P_0$	Mixed	Packed sediment bed	Aquifer redevelopment
McFaul *et al.* (2012) [179]	0.25	$150\%\, P_0$	Sieving	Microarray	Cell separation
Cheng *et al.* (2016) [189]		$> 100\%\, P_0$		Microporous membrane	Whole blood separation
Yoon *et al.* (2016) [102]	$70 - 230$		Sieving	Microarray	Cancer detection
Zhang *et al.* (2017) [264]	0.04	$70\%\, P_0$	Aggregation	Microarray and labyrinth channel	Irrigation
Lee *et al.* (2018) [112]	0.125			Microarray	Blood plasma filtration
Cheng *et al.* (2018) [100]	1	Oscillatory ($P_0 = 0$)	Sieving	Microarray	Cell capture & staining
Mehendale *et al.* (2018) [101]				Micropillar array	Whole blood enrichment
Kastl *et al.* (2021) [265]	$5 - 10$	$35 - 80\%\, P_0$	Aggregation	Microporous membrane	Forward osmosis

Table 4.1: Summary of some studies that utilized pulsatile flows for clog mitigation and relevant parameters, main clogging mechanism, geometry of the channels, and applications considered.

nearby ecosystems. In fact, chemical addition can preferentially select for opportunistic microorganisms while eliminating their competition, causing systems to clog even faster.[204] For these reasons, there is a strong motivation to develop active or passive hydrodynamic techniques to prevent or delay clogging.

In particular, while bridging and sieving can sometimes be mitigated with proper filtration and dilution, aggregation remains an intricate clogging mechanism to prevent in many applications. For instance, bacteria and algae are well-known clogging sources in irrigation, because the individual cells are too small to filter practically and can attach at constrictions via aggregation. Attached bioparticles can feed off of nutrients in the flow, allowing them to grow from micro-scale clusters to 3D milli-scale communities that clog the constriction.[271, 274] Besides, aggregation is present in any suspension flow where particles are small enough for Van der Walls forces to play a role. [275] As a result, various past studies have investigated particle deposition and aggregation at the microchannel scale [53] and the pore-scale,[259] some using DerjaguinLandauVerweyOverbeek (DLVO) theory to explain their findings. These studies utilize steady flows with a constant driving pressure, which is typical of many practical flows. Recently, Trofa *et al.* numerically investigated clogging under both constant pressure and constant flow rate for adhesive particles.[276] They demonstrated the potential to predict numerically fouling and clogging for steady flows, given sufficient input physical parameters.

Schwarze *et al.* investigated particle attachment and detachment under an accelerating shear flow. They observed a decrease in net particle deposition with increasing shear, as well as a rate-dependent hysteresis.[277] In their experiments, particles that deposit and remain attached at a lower shear can detach and become re-suspended at higher shear. In fact, hydrodynamic techniques like backflushing and high-pressure flushing have historically been used to periodically manage clogging, as reversing the shear direction or increasing its magnitude can shed particles from partially clogged constrictions.[278, 279]

These observations suggest that this phenomenon can be leveraged quantitatively by continually varying the shear environment via pulsatile flows.

A pulsatile pressure-driven flow can be expressed using the instantaneous driving pressure $P(t) = P_0 + \delta P \sin(2\,\pi\,f\,t)$, where P_0 is the mean pressure, δP is the pulsatile amplitude, t is time, and f is the pulsatile frequency.[280] Pulsatile flows have been proposed as a strategy to help mitigate clogging across applications spanning irrigation, water purification, blood filtration, and cancer detection.[262, 263, 179, 189, 102, 264, 112, 100, 101, 265] Table 4.1 summarizes several studies that utilize pulsatile flows to mitigate clogging in a system. The frequency f, amplitude δP, primary clogging mechanism, constriction geometry, and application are noted if present in the original study. Most of these studies feature similar constriction geometries, *i.e.*, a parallel configuration of microchannels or micropores. There is a drastic range for frequencies and amplitudes across these experiments, despite many of them operating at similar scales. Although the studies mentioned in Table 1 demonstrate clog mitigation via pulsation, none are systematic with respect to pulsation and they often fail to report critical pulsatile parameters. Furthermore, most studies focus on either the pore-scale or system-scale thus lacking the information to bridge the microscale dynamics to the mascroscopic flow rate. In particular, no mechanisms to explain why pulsatile flows may be efficient at delaying clogging were clearly visualized. Thus there remains a significant knowledge gap in optimizing pulsatile parameters and pumping schemes to balance clog mitigation with energy input. Besides, to better understand the mechanisms at play during the clogging of microchannels in pulsatile flow, it is important to be able to visualize the dynamics both at the macroscopic scale but also at the pore scale.

In this study, we investigate experimentally a range of pulsatile amplitudes δP and frequencies f as they relate to clog mitigation in a microfluidic array. We first present the experimental methods in section 4.1.3. The array, shown in figure 4.1, shares common

features with a conventional filter in geometry, consisting of identical parallel pores. We enforce the instantaneous driving pressure $P(t)$ in our experiments while directly measuring the total flow rate $Q(t)$ through the array. Section 4.1.4 then reports the experimental results for both clogging under steady conditions and for pulsatile flow when varying the amplitude and the frequency of pulsations. We combine the flow rate measurements with direct visualization to correlate clogging at the individual pore scale with measurement of the flow rate at the device scale. Finally, section 4.1.5 considers in more detail the change in the probability of clogging with pulsatile flows. In particular, we show that an exponential distribution, corresponding to a Poisson process, captures the clogging dynamics in both steady and pulsatile conditions, but the time or volume intervals between two clogging events increases for a pulsatile flow. We also highlight some clogging and unclogging scenarios that explain our observations and shed light on the mechanisms behind pulsatile clog mitigation.

4.1.3 Experimental Methods

Microfluidic chip

The microfluidic array, shown in figure 4.1 is fabricated out of polydimethylsiloxane (PDMS) Sylgard 184 through soft lithography and plasma-bonding to a PDMS-coated slide. This method ensures that all internal surfaces are made of the same material. Plasma-bonding leaves the surfaces temporarily hydrophilic, and they slowly recover their hydrophobicity over time. Uncontrolled hydrophobicity could cause different clogging rates between experiments.[281] To address this issue, all devices are thermally annealed at 120 °C for at least three hours prior to experiments to ensure consistent hydrophobicity.[259] The array consists of 40 microchannels, each with minimum constrictions of 10 μm and largest width of 50 μm and a channel depth of 13 to 15 μm.[53, 56]

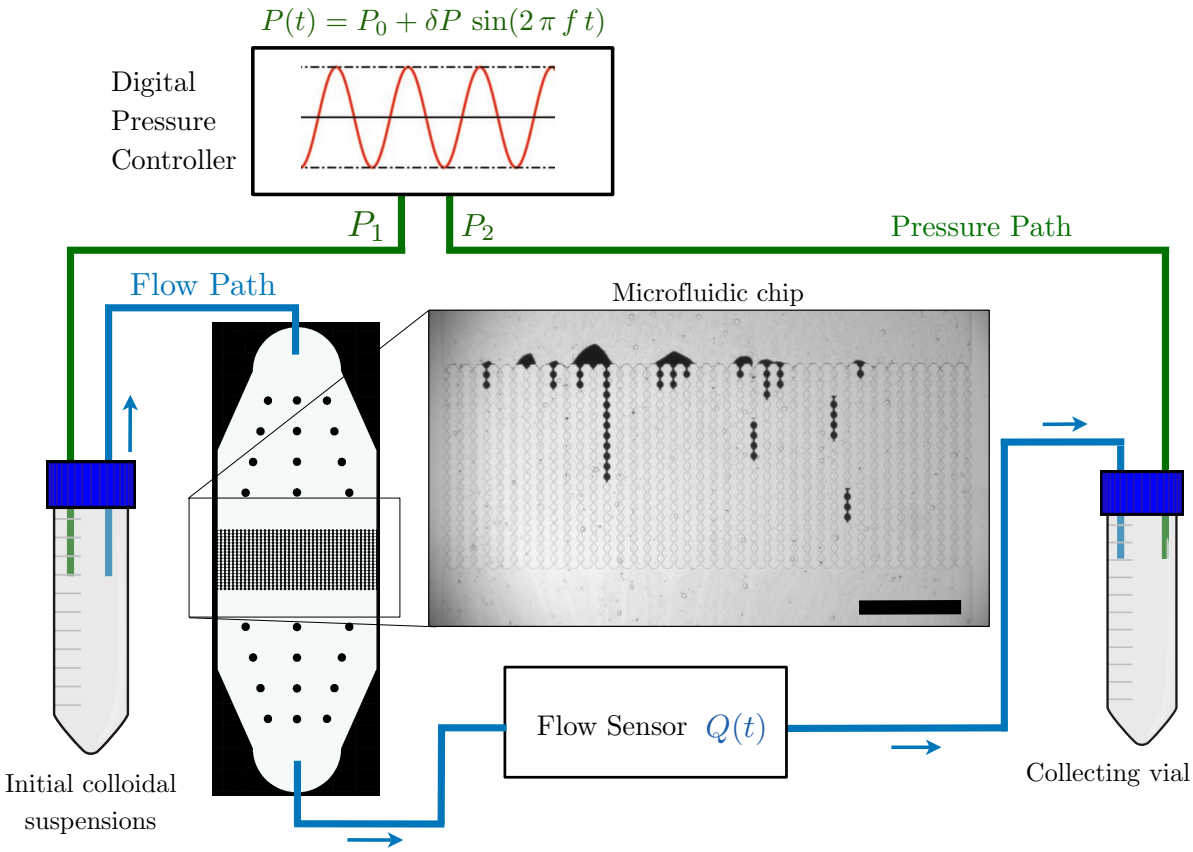

Figure 4.1: Schematic of the experimental setup showing the pressure driven system, the microfluidic device and the flow sensor. The square area indicates the region of observation. Scale bar is 1 mm.

The parallel channels connect two large reservoirs, which serve as the inlet and outlet for the suspension flow. Each reservoir has 12 large pillars which serve as anchors to minimize pressure-induced deformation. Deformation is undesirable in these experiments, as it makes the pressure-flow rate relationship nonlinear, and could also cause particles attached in the reservoir to shift and migrate down to the array. Since the nonlinearity between P and Q would influence clogging in an uncontrolled manner, we verified experimentally that we work in the linear regime, even for the largest pressure difference used during the pulsatile experiments.

Suspension properties and preparation

The suspension is comprised of pure water (Millipore Milli-Q), 100 mM NaCl (Sigma-Aldrich), and 2 μm carboxylate-modified latex beads (Invitrogen) at a volume fraction of $\phi = 0.3\%$. At this volume fraction, the suspension viscosity remains unchanged from water,[282] while also minimizing the probability of bridging events.[71] The beads have a density $\rho = 1.055$ g cm^{-3} at 20 ^{o}C, thus sedimentation is negligible. The particles are stable up to 1 M univalent salt, and even higher based on our testings. Without the addition of salt, we encountered variation in clogging times that we believe may be due to streaming electrification, which can occur when ultra-pure water flows past insulating surfaces. [283, 284] The addition of salt prevents charge accumulation and improves the repeatability of experiments. Besides, the addition of salt is a common aspect of numerous clogging studies, as the increased ion availability decreases the Debye's length and pushes the aggregation process into the Van der Waals Regime.[73, 281]

Each suspension is filtered through an 8 μm track-etched membrane filter (Whatman Nuclepore) directly before experiments. This eliminates particles and aggregates that would immediately clog the array through sieving since the width of the constriction is $W = 10\,\mu$m. We measured the particle size distribution and obtained a resulting diameter

$d = 2.4 \pm 0.56\,\mu$m (see Supplemental Materials), smaller than the constriction width W with an aspect ratio $W/d \simeq 4.2$ thus, most particles cannot lead to clogging by sieving or bridging.[58] However, larger anisotropic aggregates in the tail of the distribution could sieve the constriction after a monolayer of particles deposit and shrink the local width of the constriction. During the experiment, we avoid stirring the suspension to minimize shear stress prior to reaching the array. The velocity field associated with stirring increases the probability of particle interaction, which could cause particles to aggregate prior to reaching the array.

Experiment overview

A diagram of the entire experimental setup is depicted in figure 4.1. For each experiment, inlet and outlet pressure are enforced by a digital pressure controller (Elveflow OB1 MK3+) with $P_0 = 150\,$mbar. The average pressure P_0 is kept constant in all the experiments presented in this paper, and the amplitude and frequency of pulsation are varied in the range $37.5\,\text{mbar} \leq \delta P \leq 187.5\,\text{mbar}$ and $10^{-3}\,\text{Hz} \leq f \leq 10^{-1}\,\text{Hz}$, respectively. These pulsations are directly imposed through a commercial pressure controller, which relies on piezo regulation. We tested the system frequency limitation, *i.e.*, the maximum frequency at which the flow rate still follows the time-varying pressure to select the upper frequency limit, $f = 0.1\,$Hz, for our system (see Supplemental Materials). The flow rate is continually measured with an in-series Coriolis flow sensor (Bronkhorst) downstream of the array. The flow sensor smooths the measurement over intervals smaller than 1 s. However, since the raw data exhibits some fluctuations inherent to the accuracy of the flow senser, we further smooth the data using a custom-made MATLAB routine based on an moving average with a window of typically 100 s for $f = 0.01\,$Hz and of 50 s for every other cases. This time window is smaller than the clogging time and thus does not influence our measurements of the clogging frequency and the long-term evolution of the

flow rate. However, we shall see later that for the smallest frequency used in this study, $f = 0.001\,\mathrm{Hz}$, the smoothing interval is such that we still observe the oscillations in the flow rate. The array is transparent and positioned under an inverted microscope (Nikon Eclipse), allowing us to record a video at two frames per second with the attached USB camera (IDS Imaging) for the entire duration of each experiment, typically around 10 hours.

For each experiment, we begin by pre-filling the system with 100 mM NaCl to remove any air bubbles. Then we introduce the particle suspension and start recording the flow rate and video footage synchronously. We allow the experiment to run until either (a) all 40 channels have clogged or (b) at least 10 hours have passed – whichever comes first.

Each video is then reviewed to extract the time and location of each clog. There are 40 channels with 20 constrictions per channel, or 800 potential clog locations. To aid in the review process, we utilize a grid overlay, custom-made for this device footage. This makes the review process simpler and less error-prone.

For the experiments performed in the present study, the flow is laminar with an associated Reynolds number $\mathrm{Re} = uL/\nu \leq 0.4$, where u is the flow velocity in an open channel, L is the hydraulic diameter of a pore, and $\nu = \eta/\rho$ is the kinematic viscosity of the suspension. The average Womersley number $\mathrm{Wo} = L\sqrt{2\,\pi\,f/\nu}$ remains smaller than 0.01 across experiments, thus transient inertial forces due to pulsation are negligible compared to viscous forces.[108] For low-Reynolds and low-Womersley number flows, such as those featured in the present study, the pressure and flow rate are linearly related through the Hagen-Poiseuille equation. [285] The average Péclet number is $\mathrm{Pe} = u\,L/D \sim 10^5$, where D is the mass diffusivity for a particle of diameter $d = 2\,\mu\mathrm{m}$, given by the Stokes-Einstein equation $D = k_b T/(3\pi\eta d)$, where k_b is the Boltzman constant and T is the temperature. Therefore, in the present system, the particle transport is governed by advection, and diffusion plays a negligible role.

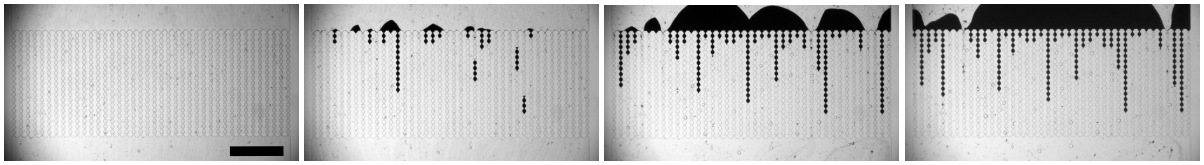

(a) (b) (c) (d)

Figure 4.2: Time lapse showing an example of clogging dynamics observed in a steady pressure experiment, beginning with a clean device. Over time, clogs form at the constrictions while the filter cakes grow until all or most channels are clogged. Pictures taken at (a) $t = 0\,\mathrm{s}$, (b) $1920\,\mathrm{s}$, (c) $11520\,\mathrm{s}$ s, and (d) $30000\,\mathrm{s}$, respectively. Scale bar is 1mm.

4.1.4 Results

Clogging and Flow Reduction under Steady Flow

First, we aim to characterize clogging under steady flow with $P = P_0 = 150\,\mathrm{mbar}$. We chose this value for P_0 to ensure that we do not exceed the deformation limit for the device during pulsatile experiments, which are subject to higher instantaneous pressures than the steady case (see Supplemental Materials). During the first one thousand seconds, initial clogs begin to seed the array, as shown in figure 4.2. Since we work at constant input pressure, and the hydraulic resistances of the tubings and the reservoir are negligible compared to the microchannels, the flow rate is the device is the sum of the flow rate in each individual microchannels. In addition, the flow rate q in each microchannel is drastically reduced for clogged constrictions, but remains nonzero due to the porosity of the clog.[59] As a result of the pressure-driven flow, the flow rate in the non-clogged microchannels remains similar throughout the experiments. At clogged channels, since particles may arrive but not pass, a filter cake begins to develop at each clogged constriction. This filter cake can then grow and merge with other filter cakes, or even spill into an adjacent channel, potentially catalyzing another clog. This interaction between the parallel microchannels and filter cakes is present in many real filtration environments. Eventually, most or all of the channels clog, reducing the flow rate to ¡5%

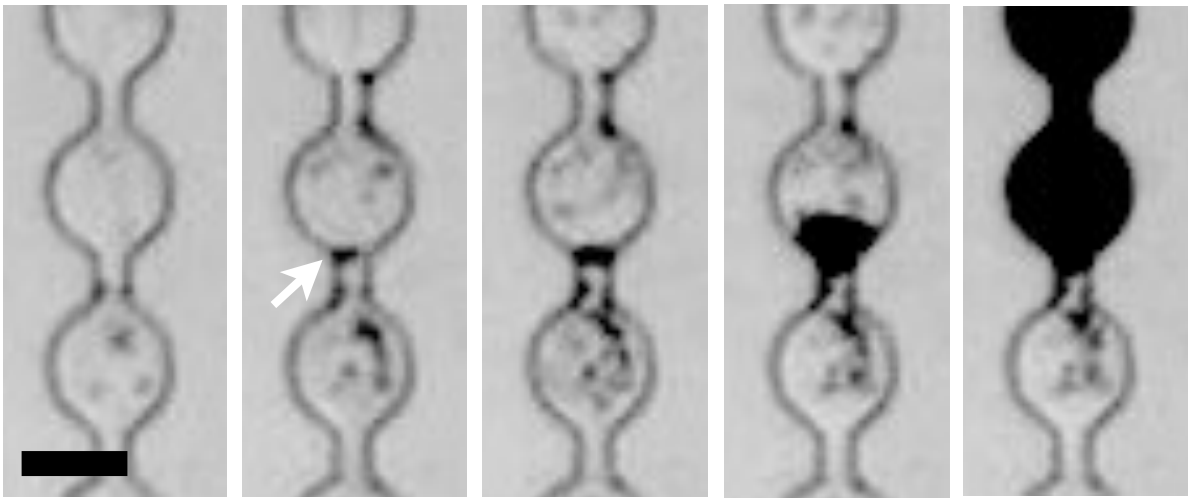

Figure 4.3: Time lapse showing the progression of an individual clog at the pore scale. Particles deposit along the device walls shrinking the constriction (for instance as shown by the white arrow in (b)) until a final particle or aggregate arrives and clogs the constricted channel leading to the creation of a filter cake and a reduction of the flow rate to nearly zero. Pictures taken at (a) $t = 0\,\mathrm{s}$, (b) $300\,\mathrm{s}$, (c) $600\,\mathrm{s}$, (d) $1000\,\mathrm{s}$, and (e) at the end of the experiment, respectively. Scale bar is 40 um.

of the initial flow rate.

At the pore scale, we can observe the progression of an individual clog, as shown for instance in figure 4.3. The particles successively deposit onto the walls of the constriction, shrinking its effective width and height. Eventually, a final particle or aggregate sieves the constriction, preventing future particle passage. This process takes place over hundreds to thousands of seconds for each microchannel. The clog formation depends on the concentration of aggregates in the suspension, the initial deposition of the particles on the wall, as well as the probability of sieving and bridging at the constrictions with reduced widths.[56, 254]

The flow rate for five independent steady experiments is reported in figure 4.4, as well as the mean value and standard deviation between this set. Due to slight variations in channel depth between microfluidic chips, the initial flow rate before any clogging

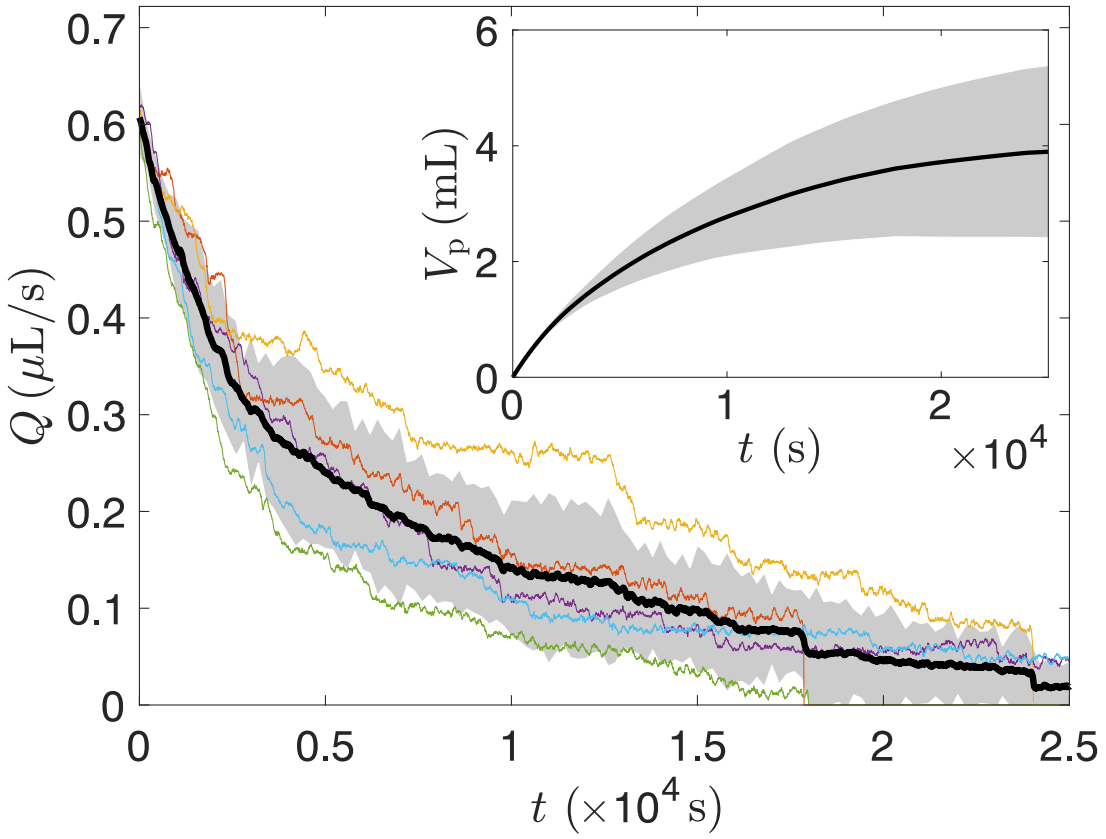

Figure 4.4: Flow rate Q from five independent steady flow experiments (color lines). The thick black line shows the mean value, and the standard deviation among this set is represented by the gray area. Inset: Time evolution of the volume of suspension processed $V_\mathrm{p} = \int Q\,\mathrm{d}t$ obtained from integrating the mean flow rate data shown in the main panel.

occurs is equal to $Q_\mathrm{avg} = 0.60 \pm 0.04\ \mu\mathrm{L.s}^{-1}$ at 150 mbar, *i.e.*, can vary slightly between devices. Therefore, for systematic comparison and to average across experiments, we report the rescaled flow rate $(Q_\mathrm{exp}/Q_0)\,Q_\mathrm{avg}$, where Q_exp and $Q_0 = Q_\mathrm{exp}(t = 0)$ are the flow rate directly measured from the flowmeter and the initial flow rate in a given device, respectively, and Q_avg is the average flow rate at time $t = 0$ between all devices tested with the same pulsatile conditions. We later refer to this quantity as Q. We observe the same overall behavior for the five experiments reported here: the total flow rate Q

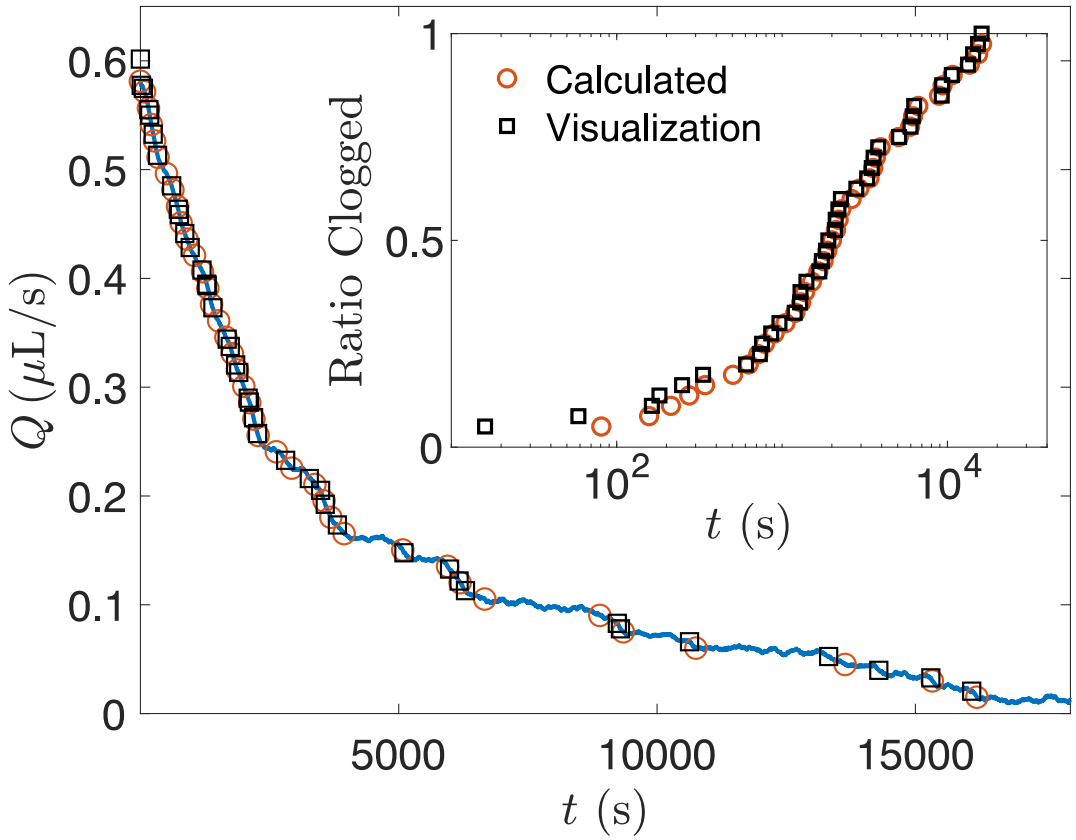

Figure 4.5: Comparison of raw clogging times obtained by direct visualization at the pore scale (black squares) and the calculated clogging times obtained by using a criterion on the reduction of flow rate by $1/N$, where $N = 40$ is the number of parallel microchannels (orange circles). Inset: Time evolution of the ratio of clogged channel for the experiment pictured in the main panel.

exhibits a fast decrease as initially, all the channels may be subject to clogging. After an initial period of frequent clogging events and a fast decrease of the flow rate Q, the last clogging events are slower so that over time the evolution of the flow rate slows down until reaching a value close to zero (but not zero) at the end of the experiments where most of the $N = 40$ channels, if not all, have clogged.

We define the total volume processed as $V_\mathrm{p} = \int Q \, \mathrm{d}t$, where we use the flow rate averaged across experiments. The aim of a method to delay clogging would be to reach a larger volume processed over the lifetime of the device. We report the evolution of V_p as

a function of time in the inset of figure 4.4. After an initially large volume is processed, V_{p} saturates when most of the microchannels are clogged.

To correlate the evolution of the total flow rate through the device with the formation of individual clogs, we compare flow rate measurements with direct visualizations at the pore scale. Figure 4.5 shows the flow rate Q for a single experiment. We report the clogging times determined through direct visualization (black squares) superimposed to the evolution of the flow rate. A channel is considered fully clogged when particles can no longer be seen exiting a constriction. We can also detect clogging events based on the total flow rate. Indeed, there are $N = 40$ channels per device, each with a flow rate $q = Q_0/N$. We plot in figure 4.5 successive $1/40^{th}$ reductions in Q_0, assuming that it gives a good estimate of the clogging dynamics. One can note that the flow rate-predicted clogging times align fairly well with the direct visualization at the pore scale. The observed and the flow rate-predicted clogging times are re-plotted in the inset of figure 4.5 as a ratio of channels clogged against time. The evolution with time of the relative number of clogged channels has a behavior similar to what was reported in previous studies.[53] The slight delay between an estimate based on the flow rate is likely due to the time required to build a sufficiently long filter cake, so the flow rate in the channel becomes negligible, typically a few tens of seconds.[59] The agreement between these curves demonstrates the clear relationship between flow rate and clogging times. Thus we can reasonably infer clogging times at the microchannel scale based on reductions in flow rate at the device scale.

Influence of the Pulsatile Amplitude

For the pulsatile experiments, the maximum values for δP and f were limited by the system. At pressures above 350 mbar, the pressure-flow rate relationship becomes non-linear as the PDMS begins to deform.[286, 287] At frequencies greater than 0.1 Hz,

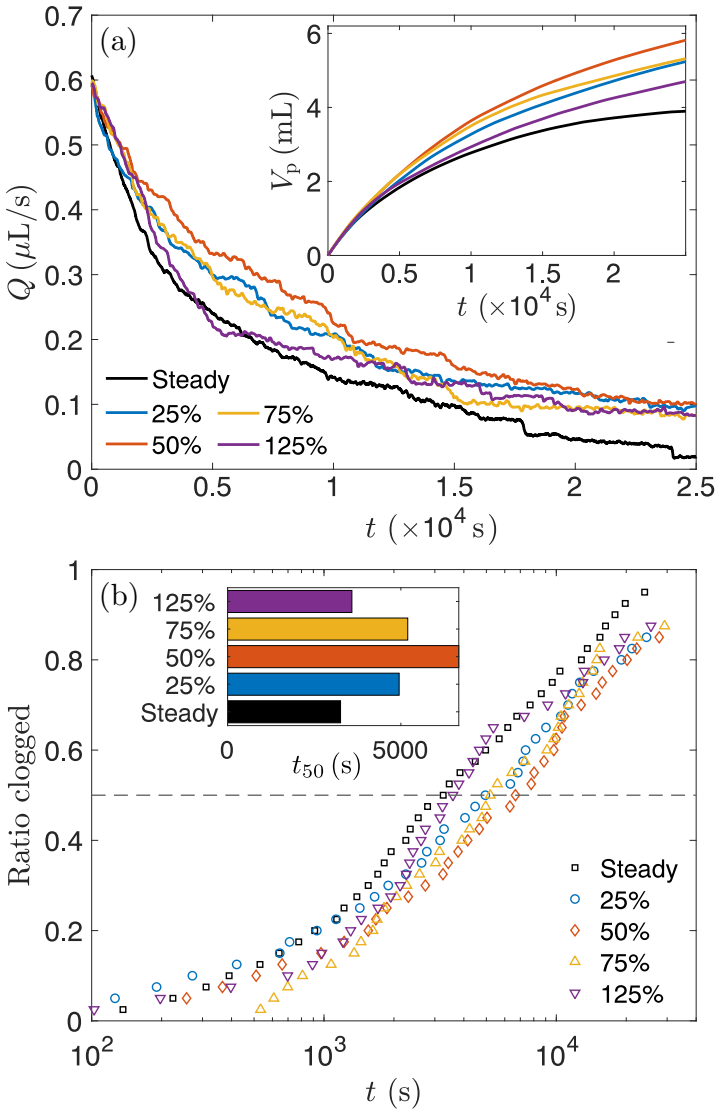

Figure 4.6: Influence of the rescaled amplitude of pulsation $\delta P/P_0$ for a frequency $f = 0.1\,\mathrm{Hz}$. (a) Flow rate for the steady experiments (in black) and for the pulsatile experiments for an amplitude of pulsation $\delta P/P_0 = 25\%$ (blue line), $\delta P/P_0 = 50\%$ (orange line), $\delta P/P_0 = 75\%$ (yellow line), and $\delta P/P_0 = 125\%$ (purple line). Inset: Cumulative volume processed V_p for pulsatile experiments, compared to steady. The color code is the same as the one used in the main panel. (b) Ratio of clogged channels for pulsatile experiments compared to the steady case. The horizontal dashed line indicates the device half-life. Inset: Average time t_{50} to reach a clogging ratio of 50% for a given amplitude of pulsation $\delta P/P_0$.

the maximum and minimum flow rates predicted by the Hagen-Poiseuille equation are not achieved due to the compliance of the system. The details of the characterization of the limits of our system are reported in Supplementary Informations.

We vary the pulsatile amplitude at a constant frequency $f = 0.1$ Hz, still keeping the average pressure constant and equal to $P_0 = 150\,\text{mbar}$, and compare the results to the steady experiments. We consider pulsatile amplitudes of $\delta P = [0.25, 0.5, 0.75, 1.25]\,P_0$, corresponding to $\delta P = [37.5, 75, 112.5, 187.5]\,\text{mbar}$. Note that the case $\delta P = 1.25\,P_0$ constitutes a case where a total flow reversal occurs. The flow rate Q and volume processed V_p are plotted in figure 4.6(a). We observe some degree of clog mitigation for every pulsatile amplitude tested; up to around 50% improvement in flow rate and volume processed compared to steady flows. Therefore, these results suggest that simply adding a fluctuating component to the flow in an array of parallel microchannels can significantly increase the lifetime of such devices. The increase in the lifetime of the device is related to the increase in clogging time interval. Indeed, figure 4.6(b) reports the time evolution of the clogging ratio for each pulsatile amplitude. We also extracted the device half-life, *i.e.* the expected time to reach a clogging ratio of 50%. We found pulsation can achieve nearly 100% improvement in filter half-life compared to a steady flow. Interestingly, even relatively small pulsation amplitude (25%) increases the lifetime of the microfluidic device. However, for pulsation amplitudes leading to flow reversal, $\delta P > P_0$, the advantage of pulsatile flow on clogging mitigation decreases for the present system of parallel microchannels.

The improvement in clogging resilience thanks to pulsatile flow is likely due to several factors, some of which have been observed directly and will be discussed in section 4.1.5. In particular, the introduction of pulsation leads to a mechanism where particles can attach during low shear and then detach at a higher shear, increasing the time it takes for an individual clog to form.[277] PDMS is also a slightly deformable material, thus

it is possible to squeeze a rigid particle or aggregate through a deformable constriction at a higher pressure,[258, 288, 70] though we note this occurrence to be extremely rare at the pressures considered here. Finally, we have observed that the filter cake itself is deformable, as it tends to shrink under higher pressures and grow under lower pressures due to variations in the local porosity. This can result in the unclogging of a channel if a filter cake can shrink enough to pass a constriction, or conversely, expand enough to facilitate a higher permeability and increased drag environment, which can move particles.

However, as emphasized previously, the largest amplitude demonstrated the least improvement in our configuration. Indeed, at amplitudes where $\delta P > P_0$, the flow is reversed with each period of oscillation. Although this condition may lead to favorable effects in a straight channel, it appears to be undesirable in parallel multichannel systems, as flow reversal allows clogs and aggregates to affect other channels. Indeed, we have observed channels becoming clogged due to a re-suspended aggregate entering adjacent microchannels. This situation will be discussed further in section 4.1.5. In summary, pulsatile flows results in a dynamic force environment that is not present in steady flows. Generally, the unclogging phenomena out-pace the clogging phenomena for the amplitude and experimental conditions considered here since pulsatile flows lead to longer clogging times.

Influence of the Pulsatile Frequency

A second key parameter that characterizes pulsatile flows is the frequency f. We now keep the pulsatile amplitude constant, $\delta P = 0.5\, P_0$ and vary the frequency f between 10^{-3} Hz and 10^{-1} Hz. The flow rate and the total volume processed are reported in figure 4.7(a). Similar to the previous section, we also report the clogging ratio to compare the different cases in figure 4.7(b). Here the transition in the evolution of the clogging

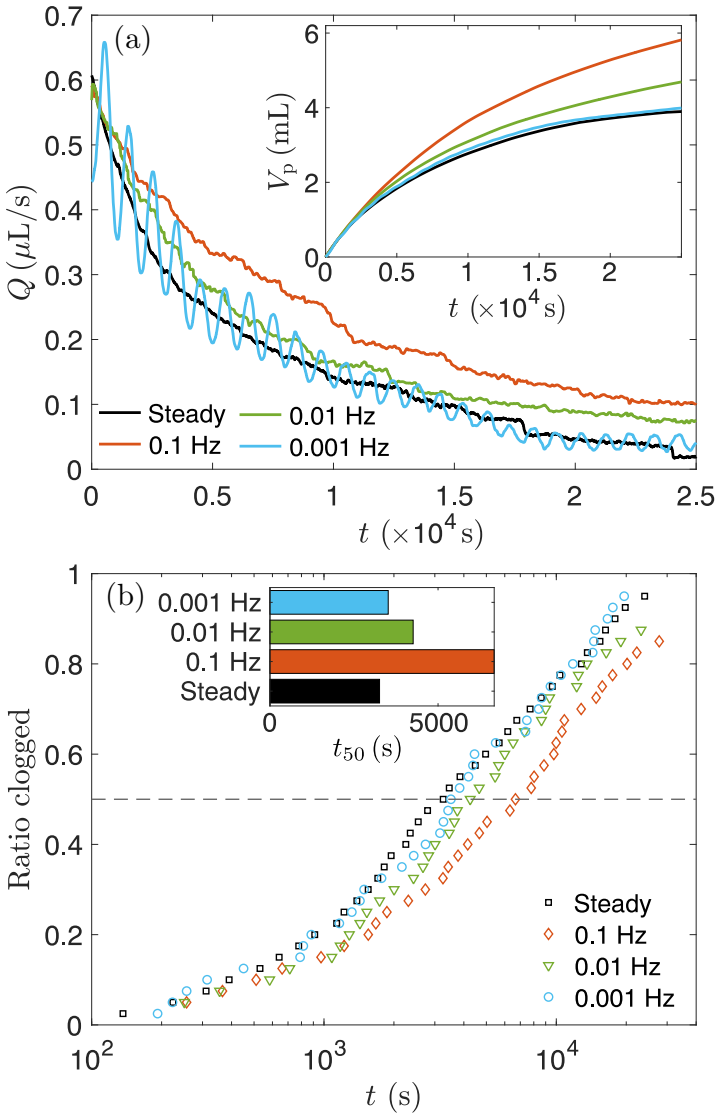

Figure 4.7: Influence of the frequency of pulsation f for an amplitude $\delta P/P_0 = 50\%$. (a) Flow rate for the steady experiments (in black) and for the pulsatile experiments ($\delta P/P_0 = 50\%$) for a frequency $f = 0.1\,\text{Hz}$ (orange line), $f = 0.01\,\text{Hz}$ (green line), and $f = 0.001\,\text{Hz}$ (blue line). Inset: Cumulative volume processed V_p for pulsatile experiments, compared to steady. The color code is the same as the one used in the main panel. (b) Ratio of clogged channels for pulsatile flow experiments compared to the steady case. The horizontal dashed line indicates the device half-life. Inset: Average time t_{50} to reach a clogging ratio of 50% for a given frequency of pulsation f.

dynamics from steady to pulsatile flows is clear. Indeed, we observe that clogging is best mitigated at the highest frequency that we can reach in our system ($f = 0.1\,\mathrm{Hz}$).

At $10^{-3}\,\mathrm{Hz}$, the lowest frequency tested, all curves closely follow the steady flow experiments. This is because, at this frequency, the period of pulsation $T = 1/f = 1000\,\mathrm{s}$ is too large compared to the timescale of clogging, of order a few 100s of seconds. The benefits of pulsation are therefore not observed because the device clogs as if the flow was steady. Indeed, as soon as a clog forms, a filter cake emerges. The filter cake grows, increasing its size as particles arrive but cannot pass.[59] Increasing the length of the filter cake reduces the flow rate and significantly damps the shear oscillations through the cake and the possibility of local reorganization that would be able to unclog the system.

4.1.5 Discussion

Probability of clogging with pulsatile flows

In this system, the clogging of a pore is due to particle deposition, aggregation, and sieving of large particles. In each experiment, an 8 μm filter sets the cutoff size for large particles and aggregates. Note that non-spherical particles, for instance, aggregates made of several particles, can have a length larger than $8\,\mu$m and a width smaller than $8\,\mu$m. These aggregates or large particles could still flow through the filter and later clog the microchannels. Such aggregates are likely to be found in infinitesimal quantity but can still control the clogging events.[254, 255] Since the constrictions are of width $\sim 10\,\mu$m and the particles have a diameter $\sim 2.4\,\mu$m, this means that sieving is not possible until enough particles have deposited onto the sidewalls of constrictions. We observe that particle-wall attachment begins immediately after starting an experiment, forming a sparse monolayer. Particle-particle attachment is minimal due to their electrostatic stabilization. This means that after the deposition of a monolayer, the sieving of aggre-

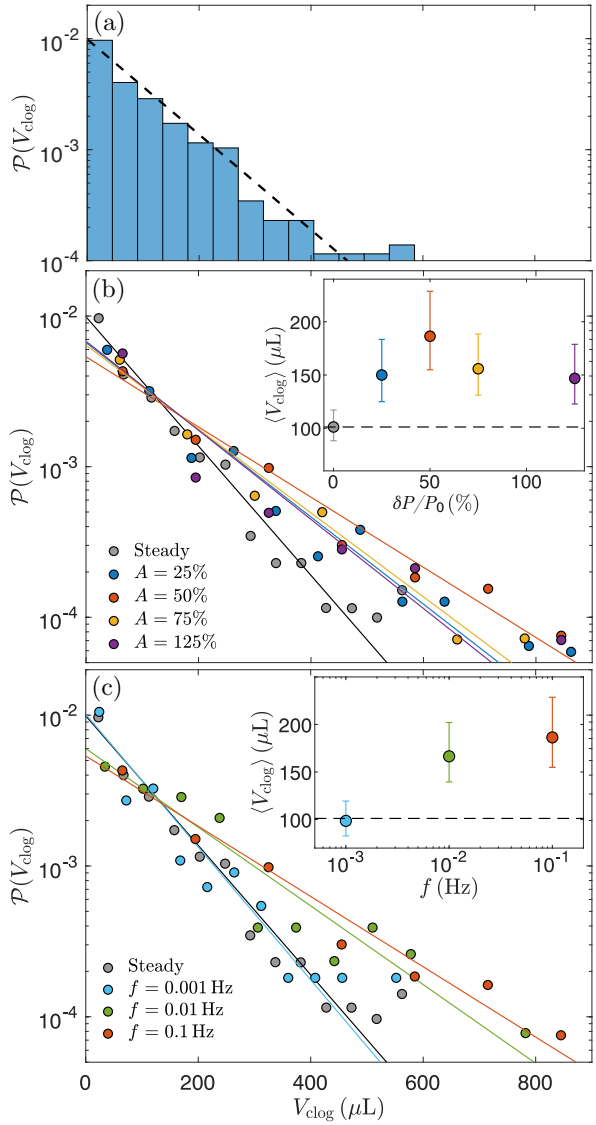

Figure 4.8: (a) Distribution of clogging volume intervals $\mathcal{P}(V_{\mathrm{clog}})$ in the steady case ($f = 0$). The black dotted line is the best fit assuming an exponential distribution with $\langle V_{\mathrm{clog}}\rangle = 101\,\mu$L. (b)-(c) Comparison of the distribution of clogging volume intervals $\mathcal{P}(V_{\mathrm{clog}})$ when varying (b) the amplitude of pulsation $\delta P/P_0$ at $f = 0.1$ Hz and (c) the frequency of pulsation f at $\delta P/P_0 = 0.5$. In both figures the circles are the experimental results and the continuous line are the corresponding best fit with an exponential distribution given by Eq. (4.4). In figures (b) and (c) the insets show the average clogging volume interval $\langle V_{\mathrm{clog}}\rangle$ and the horizontal dashed line indicates the steady case.

gates of superparticles that can be smaller than $8\,\mu$m governs the clogging process since locally the width of the constriction can be reduced down to $5-6\,\mu$m. These aggregates, or large particles, may be anisotropic; thus, they may sieve in some orientations and flow in others.[254]

Sieving in an array of parallel microchannels can be described by a Poisson process. [56, 59] In the present case, we assume that (i) large aggregates or particles are present in the suspension, which can clog channels by sieving after monolayer deposition, (ii) the deposition of the monolayer happens on a timescale smaller than the sieving (*i.e.*, for a dilute amount of large aggregates in the suspension) and that the monolayer appears at the same rate for every channel. Finally, (iii) each free constriction has an equal probability of intercepting an aggregate that may sieve it. In addition, we consider that the clogging dynamics follows a Poisson process for steady and pulsatile forcing. The pulsation can decrease the possibility of clogging through different mechanisms such as the reorientation of a non-spherical aggregate, the temporary increase of pressure on the sieved particle that eventually unclogs the channel, etc. Therefore, we define c as the number of clogging entities per unit volume (due to large aggregate, bridging events, etc.). Note that c is not simply a concentration of large aggregates in the suspension like in previous studies,[56, 254] but also depends on the pulsation parameters.

The clogging time interval in seconds between the clogging of the i-th and the $(i-1)$-th channel is defined as $t_{\mathrm{clog},i} = t_i - t_{i-1} = 1/[c\,Q(i)]$. [56] The index $i \in [1, N]$ therefore denotes the i-th clogging event, irrespective of the position of the channel in the microfluidic array. The clogging time interval depends on c, and on the instantaneous total flow rate $Q(i) = (N-i)\,q$, where $N-i$ is the number of unclogged channels and q is the flow rate in each unclogged channel. Note that since the hydraulic resistance of the reservoir and the tubings are negligible compared to the microchannels, q depends at first order on the pressure input $\Delta P(t)$ and the hydraulic resistance of a single microchannel

R_{hyd} through $q = \Delta P / R_{\text{hyd}}$. The average clogging time $\langle t_{\text{clog}} \rangle$ is then given by:[59]

$$\langle t_{\text{clog}} \rangle = \frac{1}{N} \sum_{i=0}^{N-1} \frac{R_{\text{hyd}}/(N-i)}{c\,\Delta P} = \frac{1}{Nqc} \sum_{j=1}^{N} \frac{1}{j}. \tag{4.1}$$

For a number of channels N large enough, this expression leads to

$$\langle t_{\text{clog}} \rangle = \frac{H_N}{N\,c\,q}, \tag{4.2}$$

where $H_N = \ln N + \gamma$ is the harmonic number of order N, with $\gamma \simeq 0.577$ the Euler's constant. Using the time interval is convenient for steady flows, since time is linearly related to the number of particles passing through a constriction, which controls the clogging.[53, 56] However, with pulsatile flows, the number of particles depends on the flow rate, which varies throughout the pulsatile waveform. Once the period of oscillation $T = f^{-1}$ is comparable to the mean clogging interval $\langle t_{\text{clog}} \rangle$ a different metric must be used. We use an integral approach to describe the clogging interval as the volume of fluid that passes through the device between each clogging event, such that $V_{\text{clog},i} = V_i - V_{i-1} = \int_{i-1}^{i} Q(i)\mathrm{d}t$. The clogging time interval $t_{\text{clog},i}$ and the clogging volume interval $V_{\text{clog},i}$ are related through $V_{\text{clog},i} = t_{\text{clog},i}\,Q(i)$. With this definition, the average clogging volume interval is given by $\langle V_{\text{clog}} \rangle = 1/c$ and is related to $\langle t_{\text{clog}} \rangle$ through

$$\langle V_{\text{clog}} \rangle = \frac{N\,q\,\langle t_{clog} \rangle}{\ln N + \gamma}. \tag{4.3}$$

Note that c is expected to be constant for a suspension, a microchannel geometry and a steady flow. However, in this work, c is the concentration per unit volume of potential clogging events such that adding pulsation can change the value of c. Because of the relation between t_{clog} and V_{clog}, the probability of a constriction clogging within a given

volume interval should also be captured by an exponential distribution:[56]

$$\mathcal{P}(V_{clog}) = \frac{1}{\langle V_{clog} \rangle} \exp\left(-\frac{V_{clog}}{\langle V_{clog} \rangle}\right) \tag{4.4}$$

An example of such probability distribution is plotted in figure 4.8(a) for the steady case. We observe that the exponential distribution given by equation (4.4) captures well the volume interval distribution with $\langle V_{clog} \rangle = 102 \pm 14\,\mu$L for the steady case. Note that if instead of considering $\mathcal{P}(V_{clog})$ we report $\mathcal{P}(t_{clog})$ in the present steady case, we obtain $\langle t_{clog} \rangle = 598\,$s, close to the value calculated using equation (4.3), $\langle t_{clog} \rangle = 648\,$s.

We perform a similar analysis for the different pulsatile flows and report the distribution of clogging volume interval when varying the amplitude of pulsation $\delta P/P_0$ in figure 4.8(b), and when varying the frequency f in figure 4.8(c). The inset in both figures show the corresponding average clogging volume $\langle V_{clog} \rangle$, which is related to the probability of clogging of the system.[56] This quantitative analysis demonstrates further that there is a noticeable improvement in clog mitigation at the highest frequency used here (around a factor 2 at $\delta P = 0.5\,P_0$) and that this improvement decreases when flow reversal occurs ($\delta P = 1.25\,P_0$). Besides, higher frequencies can shift the sieving probability by increasing $\langle V_{clog} \rangle$, and that the lowest frequency of $f = 0.001\,$Hz has a negligible effect (inset in figure 4.8(c)). This result is likely due to the period of pulsation, $T_{0.001Hz} = 1000s$, being larger than the mean clogging time for steady flows, $\langle t_{\mathrm{clog}} \rangle_{\mathrm{steady}} \approx 630s$.

The improvement in volume dispensed between two clogging events, and thus a decrease of the probability of clogging, is due to the reorganization of sieved particles and aggregates, as well as some slow reorganization of the filter cakes, as their shear environment changes, preventing channels from clogging or even unclogging channels which had previously become clogged. We highlight these phenomena through direct visualization at the pore scale in the following section.

Pulsatile flow can delay clogging

We have seen that pulsatile flows can improve the operational life of the microfluidic array. To explain these observations, we review the videos for any clogging phenomena which are unique to pulsation. Generally, pulsations can rearrange particles, and this can result in either clogging or unclogging, depending on several factors. We observed directly at the pore-scale three mechanisms that can delay clogging in pulsatile flows, highlighted in figure 4.9(a)-(c). The first two can be observed in all pulsatile flows considered in this study, while the last is only observed when $\delta P \geq P_0$, *i.e.*, for flow reversal.

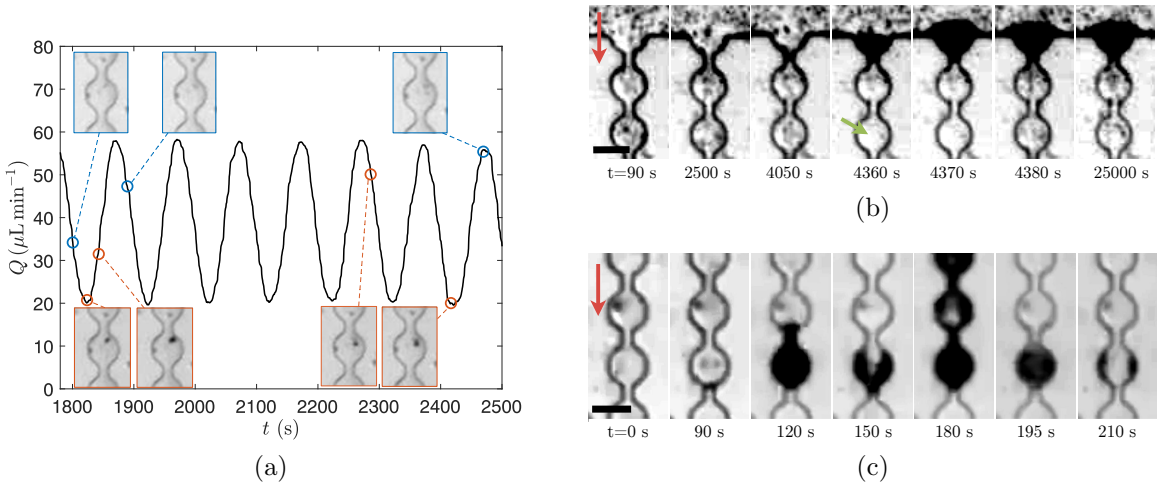

Figure 4.9: Examples of unclogging via pulsatile flows. (a) Deposition and erosion of particles during pulsation. The channel begins as clear. Then particles periodically attach (red) and detach (blue) from the channel walls. (b) Unclogging of a channel without flow reversal, due to the reorganization of the filter cake at the constriction. The constriction becomes clogged at 4360 s when no particles can be seen exiting the constriction (white background shown by the green arrow). The constriction becomes unclogged at 4380 s (grey background), when particles can be seen exiting the constriction again, and remains unclogged for over 20,000 more seconds. (c) Unclogging of a channel during the flow reversal process with $\delta P = 1.25\,P_0$ at $f = 0.1$ Hz. The constriction clogs at $t = 90\,\mathrm{s}$ and the filter cake begins to grow. The flow reversal disperses and rearranges the particles in the filter cake, allowing them to reflow over several periods. The channel eventually becomes unclogged at $t = 210\,\mathrm{s}$, with only a few particles left deposited on the sidewalls. In both figures, the scale bar is $50\,\mu\mathrm{m}$ and the average direction of the flow is indicated by the red arrow.

First, pulsatile flow temporarily increases the flow and thus the shear rate and the ability to detach particles when subject to an elevated shear.[277] The ability to erode deposited particles is illustrated for instance in figure 4.9(a), which overlays clogging images with real-time flow rate measurements over a few periods of oscillations. Particles are periodically deposited at some time and then re-suspended at a later time, maintaining a relatively clear channel when compared to steady flows. Notably, particles tend to re-suspend during high-shear conditions for each period.

The second unclogging mechanism that we observed in our experiments involves the reorganization of the filter cake. The filter cake can compress or expand as the pressure rises and falls, respectively. [289] The pulsations also allow particles in the filter cake to rearrange, likely due to a creep phenomenon.[290] This rearrangement can be large enough to partially unclog a channel, as illustrated by the example in figure 4.9(b). The pictured channel clogs at 4360 s, indicated by the lack of particles exiting the constriction at this time. By 4380 s, particles can be seen exiting the constriction again due to rearrangement of the filter cake. In this case, particles continue to flow through the constriction even 20,000 seconds after unclogging.

The last unclogging mechanism has only been observed with flow reversal ($\delta P > P_0$), and is demonstrated in figure 4.9(c) for $\delta P = 1.25 P_0$ and $f = 0.1\,\mathrm{Hz}$. A channel becomes clogged, and the filter cake begins to grow, as would be observed for any steady and pulsatile flow. However, upon flow reversal, the filter cake is ejected and then rearranged when forward flow resumes. After several periods of rearrangement, the constriction is fully unclogged, and the flow is restored. However, this scenario is observed for a minority of cases for constrictions that clog. The possible unclogging upon flow reversal is likely associated either with the reorganization and breakup of an arch of particles or with the reorientation of a non-spherical aggregate. Once the filter cake becomes large enough, the ejection and reorganization of particles become minimal during the flow reversal, and the

microchannel remains permanently clogged. Higher frequency oscillations may increase the occurrence of this mechanism, as more frequent flow reversal could help prevent filter cakes from becoming too large to eject.

Pulsatile flows can also accelerate clogging in parallel microchannels

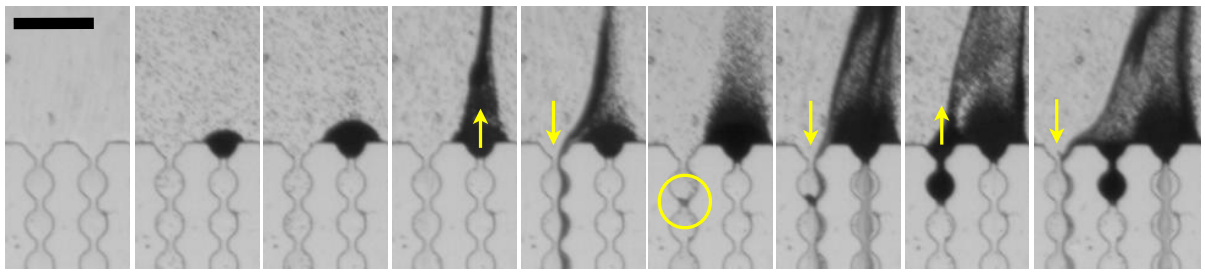

(a)

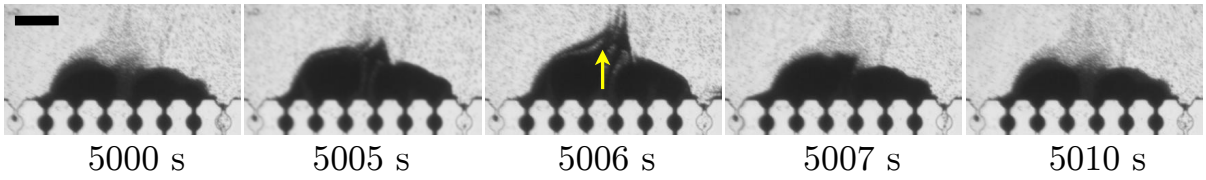

(b)

Figure 4.10: Clog acceleration via flow reversal. (a) A clog forms in the right channel at $t = 180\,\mathrm{s}$ and grows for one period of pulsation with parameters $\delta P = 1.25 P_0$ and $f = 0.1\,\mathrm{Hz}$. When the flow is reversed at $t = 192\,\mathrm{s}$, a dense stream of particles is ejected from the right channel. Once forward flow resumes at $t = 195\,\mathrm{s}$, the dense stream passes through the left channel (yellow arrow), locally depositing particles at a higher rate and clogging the adjacent channel (yellow circle). By $t = 970\,\mathrm{s}$, both channels are clogged and the process continues for the next adjacent channel. (b) This effect of the flow reversal is reduced as the filter cakes become large and several adjacent channels are clogged. In one pulsation, the ejecta for this filter cake is much smaller and does not transfer to adjacent channels. Scale bar is 140 μm in both figures.

In addition to these mechanisms that mitigate clogging with pulsatile flows, we also observe a clogging mechanism that is unique to pulsatile flows with flow reversal. In pulsatile flows without reversal, downstream particles and aggregates cannot travel upstream. With flow reversal, upstream and downstream periodically interchange. This

allows filter cakes to interact with other adjacent microchannels in a unique way. A time-lapse of this behavior is featured in figure 4.10(a) where, during reversal, particles are ejected from the filter cake as a dense cloud ($t = 192\,\mathrm{s}$). When forward flow resumes, many of these particles flow through a nearby open microchannel, taking the path of least hydraulic resistance (and larger local flow rate). This can accelerate the clogging, as it increases the local volume fraction of suspended particles and the number of particles flowing in an open microchannel, possibly also leading to bridging since the local volume fraction increases.[71] Furthermore, if particles aggregate while compacted in the filter cake, large aggregates may be ejected and flow through an adjacent channel. If aggregates are large compared to the pore size, they cause rapid clogging through sieving.[56, 254]

This peculiar dynamics explains our observations at $\delta P = 1.25P_0$ plotted in figure 4.6. Due to particle resuspension during flow reversal, clogging is accelerated when compared to other amplitudes in the early part of the experiment after some filter cakes appear. However, as the experiment progresses, filter cakes grow and merge, significantly reducing the flow rate in both directions. Thus, as filter cakes grow, ejection is reduced, as illustrated in figure 4.10(b) where the dense cloud of particles is limited and cannot be seen entering a nearby channel. This dynamics may explain why the improvement of the flow rate at a given time upon steady after the first 5000 seconds, performing similarly to the other pulsatile experiments at 0.1 Hz since the three clog mitigation mechanisms described above continue to influence the clogging dynamics.

4.1.6 Conclusions

In this work, we experimentally investigate how pulsatile flows can influence the clogging rate of a dilute suspension in an array of parallel microchannels. The previous studies mentioned in Table 1 demonstrated, mainly qualitatively, that pulsatile flow is a

good candidate to delay clogging but often failed to report critical pulsatile parameters or identify the relevant physical mechanisms at play. Our analysis bridges both scales while clearly reporting each pulsatile condition in a systematic investigation. By combining system flow rate measurements with direct visualization at the pore scale, we report several phenomena that mitigate or accelerate clogging and are unique to pulsatile flows. We find that all pulsatile amplitudes investigated increased the throughput over time when compared to steady flow conditions. We use the flow rate measurements to extract the clogging dynamics for each pulsatile condition and define a filter half-life as the average time required to reach a clogging ratio of 0.5, when half of the channels are clogged. In the optimal case for the present configuration, at $\delta P = 0.5P_0$ and $f = 0.1\,\mathrm{Hz}$, we show that pulsatile flows can nearly double the filter half-life. We attribute this to a variety of unclogging mechanisms, which we identified through pore-scale visualization. With pulsation, individual particles and aggregates may periodically detach from the device walls as their shear environment changes, delaying clogging by aggregation. Additionally, the slow rearrangement of particles in a filter cake during pulsation can result in a partial flow restoration. These phenomena are not present in steady flows.

When we consider flow reversal, where $\delta P = 1.25P_0$, we report a unique unclogging mechanism, where sufficient flow reversal can re-suspend particles in a filter cake, unclogging the constriction. Despite this, we observe little improvement in filter half-life when compared to steady flows. This is due to the fact that adjacent channels can influence each other during flow reversal.

While the pulsatile amplitude determines which clogging and unclogging mechanisms are present, the pulsatile frequency determines the probability of these events. In our case, the highest frequency investigated ($f = 0.1\,\mathrm{Hz}$) yields the greatest increase in filter half-life. At the lowest frequency we investigated ($f = 10^{-3}\,\mathrm{Hz}$), performance is indistinguishable from the steady case. Therefore, it is critical that the frequency of

pulsation is compared to the average clogging rate for a given system. If the frequency is too low, pulsation cannot delay clogging. While higher frequencies may achieve further improvement, we are unable to investigate this situation because of the limitation in our system.

This study demonstrates that even relatively weak pulsations may significantly delay clogging. In the specific case of filtration where constrictions are closely arranged in an adjacent configuration, it may be advisable to avoid flow reversal, as we observe minimal improvement in filter half-life despite the increased energy cost of large pulsations. However, in the single-channel case, flow reversal may prove highly beneficial due to its unique ability to erode deposited particle.

Author Contributions

B.D, E.D. and A.S. designed the experiments; B.D. performed experiments; B.D., C.T., E.D., A.S. analyzed the data; E.D. and A.S. supervised the overall project. All authors discussed the results. B.D., E.D., A.S. wrote the initial version of the manuscript. All authors proof checked the manuscript.

Acknowledgements

The authors acknowledge the use of the Microfluidics Laboratory within the California NanoSystems Institute, supported by the University of California, Santa Barbara and the University of California, Office of the President. A portion of this work was performed in the UCSB Nanofabrication Facility, an open access laboratory. ED acknowledges the support from the UCSB Academic Senate Faculty Grant, and AS the partial support from the U.S.-Israel Binational Agricultural Research and Development Fund (BARD) US-5336-21.

4.2 Future Perspective on Pulsatile Clog Mitigation

While pulsatile flows have demonstrated through numerous studies that they can be utilized to delay clogging in specific systems, there is still much to learn about this complex interaction and how to utilize it in existing systems. There are three significant barriers to utilizing pulsation for clog mitigation in industrial or commercial applications.

1. **Clog Prediction** is difficult, because clogging can occur over a wide range of time- and length-scales. How a system clogs depends on many factors, including but not limited to particle size, particle concentration, the average flow rate, and the geometry of the system. Currently, the only way to asses how quickly and by which manner a system clogs is by specifically studying and optimizing that system. In time, we need better models to predict both where and how systems will clog, in order to determine appropriate pulsatile parameters to manage clogging. This may come from a combination of scaled-down experiments in analogous systems (such as those presented in this thesis work), numerical simulations that can predict clogging using the parameters noted above, and validation of these results with large-scale systems.

2. **Efficient methods for generating pulsation** must be developed for a variety of systems. While variable frequency pumps may be used for on-site applications utilizing pipe-flows, many systems are more complex and may require high frequency pulsation, or localized pulsation. For instance, aquifer recharge involves water flowing through porous sediment, rather than a pipe. Incorporating pulsation into a process such as this may come in other forms, such as adding vibrations to the sediment during recharge. Generating local pulsation can be especially difficult for low-Reynolds number systems, where viscous damping prevents many natural

means of oscillation. In these cases, instabilities may be leveraged, such as the oscillation that occurs between two opposed impinging jets.

3. **Exploring the complexity of real systems**, as opposed to controlled suspensions of microparticles in custom microfluidic devices, will be a necessary step in actualizing pulsation as a solution to clogging. Like many other microfluidics-based studies, my experiments focus on low Reynolds (Re) & low Womersley (Wo) number flows, which are highly relevant to filtration and bioengineering applications. However, many applications involve significantly higher flow rates and length-scales, leading to a higher Reynolds number and potentially turbulence. Furthermore, adding pulsation to high-Re flows may yield high-Wo flow profiles, which posses a starkly different shear environment compared to low-Wo flows. Finally, we must also dive into additional suspension complexity in the form of buoyancy, high polydispersity, and even non-Newtonian effects in order to understand how to elegantly manage clogging in real systems.

Recently, I have been trying to better understand how pulsation can affect systems whose clogging is dominated by aggregation, the successive deposition of small particles which eventually grow large enough to restrict the flow. The experiments are similar to the experiments performed in the clogging study presented above, but with a different geometry. Rather than an array of small pores, which can clog by sieving, I am utilizing a much larger channel which cannot clog by sieving or bridging with the suspension I prepare.

Some results from these experiments are included in Fig. 4.11. In this experiment, the flow alternates between steady and pulsatile. A monolayer of particles quickly forms, which experiences minimal erosion. During steady flow, large aggregates grow in the channel and reduce the flow rate. During periods of pulsation, the aggregates are eroded

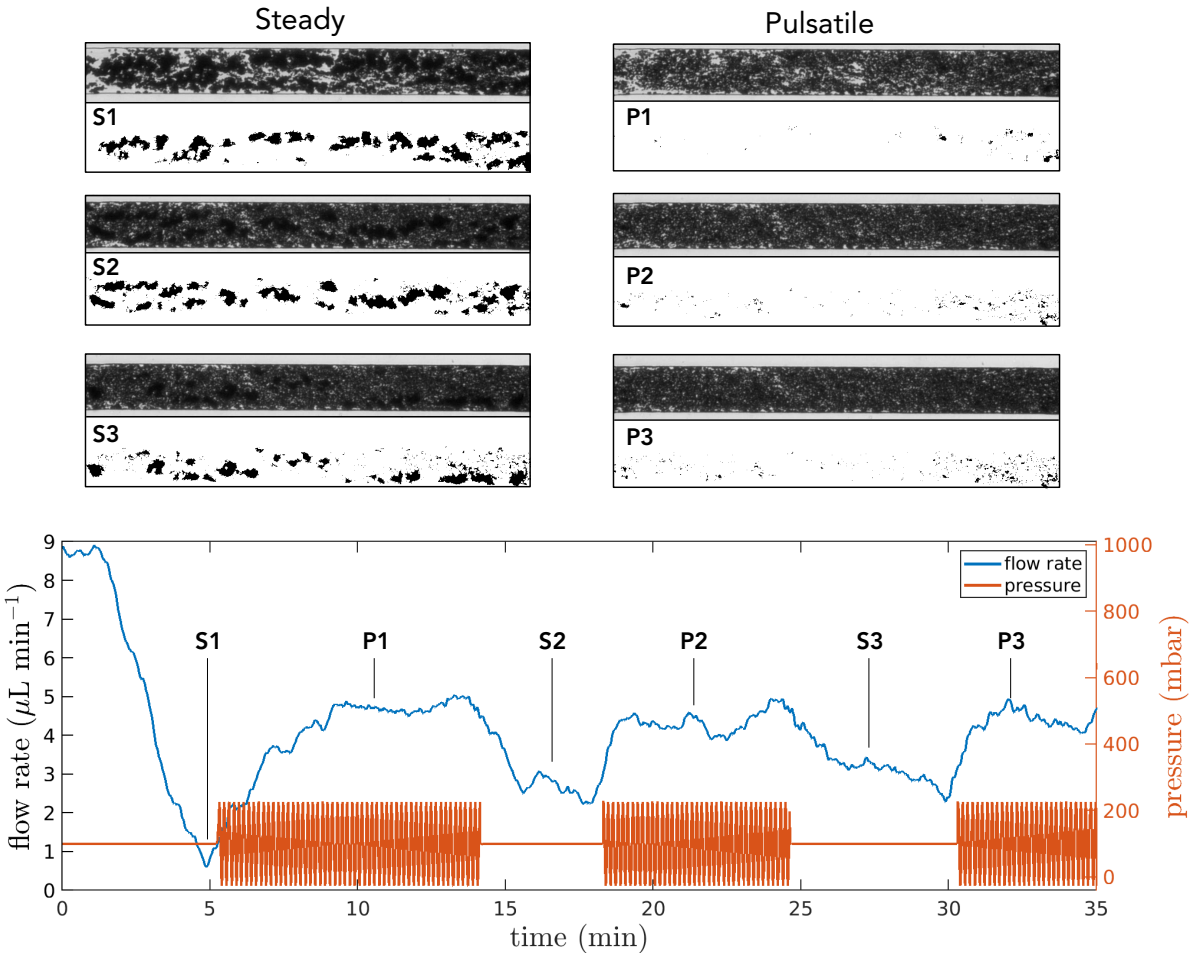

Figure 4.11: Results from an a single clogging experiment, during which I alternate between periods of steady flow, and periods of pulsatile flow. (Above) Images of the deposition channel taken during the experiment and their corresponding threshold images showing large aggregates. The channel has a width of 100 μm, a height of 15 μm, and the particles are 2 μm in diameter. (Below)A plot summarizing pressure and flow rate during the experiment. Images taken during steady (S2, S2, S3) and pulsatile (P1, P2, P3) conditions are indicated on the plot. During steady flow, large aggregates form in the channel, which can be clearly seen in thresholded images. During periods of pulsation, these large aggregates are erorded, leaving only a monolayer of particles, and the flow rate is partially restored.

and the flow rate is partially restored. One explanation could be that aggregates which form under steady flow are relatively stable when their shear environment is constant. However, with pulsation the shear environment changes direction and magnitude, exposing the instability of the aggregates and facilitating their erosion.

Aggregation is a complex process, one which is far from well-understood, yet plays a role in the clogging of many systems. Whether they are bioparticles like bacteria or algae, or inert particles such as fine sediment, the aggregation process binds particles together through Van der Waals forces, often making clogs very difficult to remediate. Therefore, understanding the aggregation process and how it can be shaped by pulsation is a critical goalpost for understanding and preventing clogs.

Chapter 5

Conclusion

Suspension flows are all around us. Depending on their components and relative ratios, suspensions can behave in a variety of complex ways. However, even when a suspension is dilute and the continuous phase is Newtonian, complex behaviours can emerge under confinement —when the flow lengthscale becomes comparable to the suspended particle lengthscale. Without confinement, dilute suspensions behave similarly to pure fluids, since the local inhomogeneities are insignificant and do not affect the bulk flow. With confinement, these inhomogeneities cannot be neglected.

All of the works presented in this thesis focus on different aspects of dilute suspensions when faced with geometric confinement. First, I focus on soft confinement by a capillary meniscus. I use a dip coating platform to probe this in a controllable way. For planar substrates, the resulting film thickness during a dip coating process is governed by the withdraw speed and the fluid properties. However, for cylindrical substrates, I show that the substrate radius also influences the thickness of the coating film. Consequently, this means that the substrate radius also influences the thickness of the stagnation point below the meniscus. Similar to the case for a planar substrate, we determine that the thickness of the stagnation point is approximately triple the thickness of the coating film

far from the reservoir.

When dip coating with suspensions, the stagnation thickness acts like a tunable filter. If the stagnation thickness is smaller than the particle radius, then the particle will be excluded from the coating film and recirculate into the reservoir. If the stagnation thickness is greater than the particle radius, then the particle will pass through the meniscus and be entrained in the coating film. I demonstrate how to use this process for efficient size-based filtration by separating small particles from large particles using a planar substrate. However, with my setup it was difficult to separate particles having radii that differ by less than a factor of 2.5, as this requires very precise velocity control during the withdraw phase for a planar substrate. With a cylindrical substrate, the radius of the substrate offers another parameter for control, which can reduce the need for ultra-precise velocity control.

One major benefit in using dip coating as a filtration platform is the absence of clogging. Traditional filters work similarly, in that they exclude particles which are larger than their pore size. However, the emergence of a filter cake results in the capture of small particles as well, so efficiecny takes a hit. Additionally, as the filter cake grows, so does its hydraulic resistance. With soft confinement (*i.e.* dip coating), there is no filter cake for dilute suspensions. Rather than large particles accumulating at the filtration point, they are recirculated into the bulk flow.

Mitigating clogging becomes a significant challenge with solid confinement —when the confining geometry is a solid surface, such as the pores of a filter or a restriction in a pipe network. As it turns out, clogging is an issue that spans a vast range of industries and application. There are many different techniques to try and prevent or remediate clogging for specific systems, however these techniques are not broadly applicable and all of them come with some cost.

One thing that all suspension flow systems have in common: the flow itself. Particles

are brought to constrictions by the flow, and if they happen to stick anywhere, they immediately feel the shear force exerted by the flow. Sometimes, their attachment force is greater than the shear force they experience, in which case they will remain attached. However, if the shear exceeds their attachment force, they can be resuspended and return to the flow. These conditions can be observed in practice. For many systems, partial clogs can be remediated by utilizing elevated pressures or reversing the flow direction. Both of these techniques drastically change the shear experienced by the stationary particles which are responsible for clogging.

Historically, many groups have passively utilized elevated pressure and flow reversal to mitigate clogging, in the form of pulsatile flows. While steady flows yield a near-steady shear environment, pulsatile flows yield an unsteady shear environment which is constantly changing. Despite numerous reports of clog mitigation via pulsation for a variety of research applications, there are very few studies that report on the independent influence of the pulsatile amplitude and pulsatile frequency —two parameters which are critical when designing systems for pulsatile flows.

Using a microfluidic array, which functionally resembles a filter or porous media, I show pulsation can drastically reduce the rate at which a system clogs, as long as appropriate parameters are chosen. Poor parameter selection may, in fact, accelerate clogging depending on the system in question. Given the additional energy cost and complexity required for designing pulsatile systems, it is important to understand how to choose an appropriate frequency and amplitude.

The pulsatile frequency determines whether or not the timescale of pulsation can keep up with the timescale of clogging. In other words, if the frequency is too low, then the benefits of pulsation cannot be realized. I show this by comparing the period of pulsation ($T = 1/f$) to the average time it takes for a pore to fully clog under steady flow (t_s). In order for pulsation to keep up, $T \ll t_s$, implying that some understanding of clogging

under steady flow is essential when choosing a pulsatile frequency. At least, that is the case for now, as it is not yet feasible to predict how quickly systems will clog without empirical testing.

The pulsatile amplitude determines whether or not the shear fluctuations will be strong enough to shift or erode particles to mitigate clogging. While all amplitudes between 25% and 75% of the mean pressure demonstrate reduced clogging for this microfluidic array, higher amplitudes featuring flow reversal yielded only minor improvements. This is largely due to the resuspension of particles and aggregates with each reversal, increasing their interaction rate with the pore walls and consequently, increasing their probability of attachment.

With these observations, an appropriate strategy to determine pulsatile parameters for a new system goes as follows: First, study the system under steady flow to obtain a sense of t_s, the average clogging time for the system. Use this value to determine an appropriate period of pulsation, which should be significantly less than t_s. Choosing a pulsatile amplitude will require some intuition of the particles responsible for clogging. For non-colloidal particles with minimal cohesion, a small amplitude may be enough. But for colloidal particles, or those exhibiting high cohesion, a much higher amplitude may be required. In either case, some additional observation and tuning can help reach the optimal parameters.

But there is still much to learn. While my experiments utilized purely sinusoidal waveforms, other shapes may offer additional insight into clogging and clog mitigation. For instance, square and sawtooth waves may yield a sharper shear transition compared to sinusoidal shapes. Additionally, asymmetric waveforms may allow some systems to utilize very high pressure fluctuations without introducing flow reversal. Even still, these results will remain largely empirical until a more comprehensive understanding of clogging is obtained; one which can account for particle shape, polydispersity, volume fraction,

zeta potential, and cohesive forces in order to predict clogging probability. Furthermore, these prediction will also depend on system geometry and surface properties. With so much left to uncover, this should be a very exciting time for those who wish to study clogging and clog mitigation!

For anyone who reads this thesis work, please feel free to contact me if you have any questions whatsoever. I very much enjoyed performing all of these experiments and interpreting the results, and welcome any future discussion related to clogging and clog mitigation.

Bibliography

[1] M. Mooney, *The viscosity of a concentrated suspension of spherical particles*, *Journal of Colloid Science* **6** (1951), no. 2 162–170.

[2] P. Coussot, L. Tocquer, C. Lanos, and G. Ovarlez, *Macroscopic vs. local rheology of yield stress fluids*, *Journal of Non-Newtonian Fluid Mechanics* **158** (2009), no. 1 85–90. Visco-plastic fluids: From theory to application.

[3] R. Skalak and P. I. Brnemark, *Deformation of red blood cells in capillaries*, *Science* **164** (1969), no. 3880 717–719, [https://www.science.org/doi/pdf/10.1126/science.164.3880.717].

[4] S. Palma and H. Lhuissier, *Dip-coating with a particulate suspension*, *J. Fluid Mech.* **869** (2019).

[5] A. Sauret, A. Gans, B. Colnet, G. Saingier, M. Z. Bazant, and E. Dressaire, *Capillary filtering of particles during dip coating*, *Phys. Rev. Fluids* **4** (2019), no. 5 54303.

[6] L. E. Scriven, *Physics and applications of dip coating and spin coating*, *Mater. Res. Soc.* **121** (1988).

[7] A. Gans, E. Dressaire, B. Colnet, G. Saingier, M. Z. Bazant, and A. Sauret, *Dip-coating of suspensions*, *Soft matter* **15** (2019), no. 2 252–261.

[8] S. J. Weinstein and K. J. Ruschak, *Coating flows*, *Annu. Rev. Fluid Mech.* **36** (2004) 29–53.

[9] D. Quéré, *Fluid coating on a fiber*, *Annu. Rev. Fluid Mech.* **31** (1999), no. 1 347–384.

[10] E. Rio and F. Boulogne, *Withdrawing a solid from a bath: How much liquid is coated?*, *Adv. Colloid Interface Sci.* **247** (2017) 100–114.

[11] L. Landau and B. Levich, *Dragging of a liquid by a moving plate*, *Acta Physicochimica URSS* **17** (1942) 42–54.

[12] B. Derjaguin and A. Titievskaya, *Experimental study of liquid film thickness left on a solid wall after receeding meniscus*, *Dokl. Akad. Nauk USSR* **50** (1945) 307–310.

[13] X. Gu, P. A. Trusty, E. G. Butler, and C. B. Ponton, *Deposition of zirconia sols on woven fibre preforms using a dip-coating technique*, *J. Eur. Ceram.* **20** (2000), no. 6 675–684.

[14] W. Wang and Y. Ku, *The light transmission and distribution in an optical fiber coated with TiO2 particles*, *Chemosphere* **50** (2003), no. 8 999–1006.

[15] K. Jost, C. R. Perez, J. K. McDonough, V. Presser, M. Heon, G. Dion, and Y. Gogotsi, *Carbon coated textiles for flexible energy storage*, *Energy Environ. Sci.* **4** (2011), no. 12 5060–5067.

[16] X. Wu, I. Wyman, G. Zhang, J. Lin, Z. Liu, Y. Wang, and H. Hu, *Preparation of superamphiphobic polymer-based coatings via spray-and dip-coating strategies*, *Prog. Org. Coat.* **90** (2016) 463–471.

[17] G. Tao, A. F. Abouraddy, A. M. Stolyarov, and Y. Fink, *Multimaterial fibers*, in *Lab-on-fiber technology*, pp. 1–26. Springer, 2015.

[18] B. M. Dincau, M. Z. Bazant, E. Dressaire, and A. Sauret, *Capillary Sorting of Particles by Dip Coating*, *Physical Review Applied* **12** (jul, 2019) 11001.

[19] F. Boyer, E. Guazzelli, and O. Pouliquen, *Unifying suspension and granular rheology*, *Phys. Rev. Lett.* **107** (2011) 188301.

[20] E. Guazzelli and J. F. Morris, *A Physical Introduction to Suspension Dynamics*. Cambridge University Press, 2011.

[21] É. Guazzelli and O. Pouliquen, *Rheology of dense granular suspensions*, *J. Fluid Mech.* **852** (2018).

[22] R. J. Furbank and J. F. Morris, *An experimental study of particle effects on drop formation*, *Phys. Fluids* **16** (2004), no. 5 1777–1790.

[23] C. Bonnoit, T. Bertrand, E. Clément, and A. Lindner, *Accelerated drop detachment in granular suspensions*, *Phys. Fluids* **24** (2012) 43304.

[24] C. McIlroy and O. G. Harlen, *Modelling capillary break-up of particulate suspensions*, *Phys. Fluids* **26** (2014), no. 3 33101.

[25] A. Lindner, J. E. Fiscina, and C. Wagner, *Single particles accelerate final stages of capillary break-up*, *EPL (Europhysics Letters)* **110** (2015), no. 6 64002.

[26] J. Château, E. Guazzelli, and H. Lhuissier, *Pinch-off of a viscous suspension thread*, *J. Fluid Mech.* **852** (2018) 178–198.

[27] M. Hameed and J. F. Morris, *Breakup of a liquid jet containing solid particles: A singularity approach*, *SIAM J. Appl. Math* **70** (2009), no. 3 885–900.

[28] S. D. Hoath, W.-K. Hsiao, I. M. Hutchings, and T. R. Tuladhar, *Jetted mixtures of particle suspensions and resins*, *Phys. Fluids* **26** (2014), no. 10 101701.

[29] J. Château and H. Lhuissier, *Breakup of a particulate suspension jet*, *Phys. Rev. Fluids* **4(1)** (2019) 12001.

[30] P. S. Raux, A. Troger, P. Jop, and A. Sauret, *Spreading and fragmentation of particle-laden liquid sheets*, *Phys. Rev. Fluids* **5** (2020), no. 4 44004.

[31] M. Zhao, M. Oléron, A. Pelosse, L. Limat, E. Guazzelli, and M. Roché, *Spreading of granular suspensions on a solid surface*, *Phys. Rev. Res.* **2** (2020), no. 2 22031.

[32] M. Ghosh, F. Fan, and K. J. Stebe, *Spontaneous Pattern Formation by Dip Coating of Colloidal Suspensions on Homogeneous Surfaces*, *Langmuir* **23** (2007), no. 4 2180–2183.

[33] C. E. Colosqui, J. F. Morris, and H. A. Stone, *Hydrodynamically driven colloidal assembly in dip coating*, *Phys. Rev. Lett.* **110** (2013), no. 18 188302.

[34] F. S. Goucher and H. Ward, *A problem in viscosity*, *Philos. Mag.* **44** (1922), no. 6 1002.

[35] D. A. White and J. A. Tallmadge, *A theory of withdrawal of cylinders from liquid baths*, *AIChE J.* **12** (1966), no. 2 333–339.

[36] F. P. Bretherton, *The motion of long bubbles in tubes*, *J. Fluid Mech.* **10** (1961), no. 2 166–188.

[37] M. Maleki, M. Reyssat, F. Restagno, D. Quéré, and C. Clanet, *Landau–Levich menisci*, *J. Colloid Interface Sci.* **354** (2011), no. 1 359–363.

[38] A. Q. Shen, B. Gleason, G. H. McKinley, and H. A. Stone, *Fiber coating with surfactant solutions*, *Phys. Fluids* **14** (2002), no. 11 4055–4068.

[39] S. Popinet, *An accurate adaptive solver for surface-tension-driven interfacial flows*, *J. Comput. Phys.* **228** (2009), no. 16 5838–5866.

[40] S. Popinet, *Numerical models of surface tension*, *Annu. Rev. Fluid Mech.* **50** (2018) 49–75.

[41] J. D. Schwarzkopf, M. Sommerfeld, C. T. Crowe, and Y. Tsuji, *Multiphase flows with droplets and particles*. CRC press, 2011.

[42] J. J. Stickel and R. L. Powell, *Fluid mechanics and rheology of dense suspensions*, *Annu. Rev. Fluid Mech.* **37** (2005) 129–149.

[43] W. R. Bowen and F. Jenner, *Theoretical descriptions of membrane filtration of colloids and fine particles: an assessment and review*, *Advances in Colloid and Interface Science* **56** (1995) 141–200.

[44] L. Svarovsky, *Solid-liquid separation*. Elsevier, 2000.

[45] S. M. Badenes, T. G. Fernandes, C. A. V. Rodrigues, M. M. Diogo, and J. M. S. Cabral, *Microcarrier-based platforms for in vitro expansion and differentiation of human pluripotent stem cells in bioreactor culture systems*, *Journal of biotechnology* **234** (2016) 71–82.

[46] A. Lenshof and T. Laurell, *Continuous separation of cells and particles in microfluidic systems*, *Chemical Society Reviews* **39** (2010), no. 3 1203.

[47] B. M. Dincau, Y. Lee, J.-H. Kim, and W.-H. Yeo, *Recent Advances in Nanoparticle Concentration and Their Application in Viral Detection Using Integrated Sensors*, *Sensors* **17** (oct, 2017) 2316.

[48] R. W. Baker, *Membrane technology and applications*. John Wiley & Sons, 2012.

[49] D. Urfer, P. M. Huck, S. D. J. Booth, and B. M. Coffey, *Biological filtration for BOM and particle removal: a critical review*, *JournalAmerican Water Works Association* **89** (1997), no. 12 83–98.

[50] D. Mark, S. Haeberle, G. Roth, F. von Stetten, and R. Zengerle, *Microfluidic lab-on-a-chip platforms: requirements, characteristics and applications*, *Chemical Society Reviews* **39** (2010), no. 3 1153.

[51] D. T. Chiu, A. J. DeMello, D. D. Carlo, P. S. Doyle, C. Hansen, R. M. Maceiczyk, and R. C. R. Wootton, *Small but Perfectly Formed? Successes, Challenges, and Opportunities for Microfluidics in the Chemical and Biological Sciences*, *Chem* **2** (feb, 2017) 201–223.

[52] J. Zhang, S. Yan, D. Yuan, G. Alici, N.-T. Nguyen, M. E. Warkiani, and W. Li, *Fundamentals and applications of inertial microfluidics: A review*, *Lab on a Chip* **16** (2016), no. 1 10–34.

[53] H. M. Wyss, D. L. Blair, J. F. Morris, H. A. Stone, and D. A. Weitz, *Mechanism for clogging of microchannels*, *Physical Review E* **74** (dec, 2006).

[54] C. Henry, J.-P. Minier, and G. Lefèvre, *Towards a description of particulate fouling: From single particle deposition to clogging*, *Advances in colloid and interface science* **185** (2012) 34–76.

[55] G. C. Agbangla, É. Climent, and P. Bacchin, *Experimental investigation of pore clogging by microparticles: Evidence for a critical flux density of particle yielding arches and deposits*, *Separation and purification technology* **101** (2012) 42–48.

[56] A. Sauret, E. C. Barney, A. Perro, E. Villermaux, H. A. Stone, and E. Dressaire, *Clogging by sieving in microchannels: Application to the detection of contaminants in colloidal suspensions*, *Applied Physics Letters* **105** (2014), no. 7 74101.

[57] G. C. Agbangla, P. Bacchin, and E. Climent, *Collective dynamics of flowing colloids during pore clogging*, *Soft Matter* **10** (2014), no. 33 6303–6315.

[58] E. Dressaire and A. Sauret, *Clogging of microfluidic systems*, *Soft Matter* **13** (2017), no. 1 37–48.

[59] A. Sauret, K. Somszor, E. Villermaux, and E. Dressaire, *Growth of clogs in parallel microchannels*, *Physical Review Fluids* **3** (oct, 2018).

[60] S. Fiedler, S. G. Shirley, T. Schnelle, and G. Fuhr, *Dielectrophoretic sorting of particles and cells in a microsystem*, *Analytical chemistry* **70** (1998), no. 9 1909–1915.

[61] D. Holmes and H. Morgan, *Cell positioning and sorting using dielectrophoresis*, in *European Cells and materials*, vol. 4, pp. 120–122, 2002.

[62] K. Grujic, O. G. Hellesø, J. P. Hole, and J. S. Wilkinson, *Sorting of polystyrene microspheres using a Y-branched optical waveguide*, *Optics Express* **13** (2005), no. 1 1–7.

[63] P. Sajeesh and A. K. Sen, *Particle separation and sorting in microfluidic devices: a review*, *Microfluidics and nanofluidics* **17** (nov, 2014) 1–52.

[64] Y. E. Yu, S. Khodaparast, and H. A. Stone, *Separation of particles by size from a suspension using the motion of a confined bubble*, *Applied Physics Letters* **112** (apr, 2018) 181604.

[65] B. B. Stogin, L. Gockowski, H. Feldstein, H. Claure, J. Wang, and T.-S. Wong, *Free-standing liquid membranes as unusual particle separators*, *Science advances* **4** (aug, 2018).

[66] B. J. Shean and J. J. Cilliers, *A review of froth flotation control*, *International Journal of Mineral Processing* **100** (2011), no. 3-4 57–71.

[67] J. C. T. Kao and A. E. Hosoi, *Spinodal decomposition in particle-laden Landau-Levich flow*, *Phys. Fluids* **24** (2012), no. 4 41701.

[68] S. Khodaparast, F. Boulogne, C. Poulard, and H. A. Stone, *Water-based peeling of thin hydrophobic films*, *Physical review letters* **119** (2017), no. 15 154502.

[69] I. E. Zarraga, D. A. Hill, and D. T. Leighton Jr, *The characterization of the total stress of concentrated suspensions of noncolloidal spheres in Newtonian fluids*, *J. Rheol.* **44** (2000), no. 2 185–220.

[70] C. Duchêne, V. Filipe, S. Huille, and A. Lindner, *Clogging of microfluidic constrictions by monoclonal antibody aggregates: Role of aggregate shape and deformability*, *Soft matter* **16** (2020), no. 4 921–928.

[71] A. Marin, H. Lhuissier, M. Rossi, and C. J. Kähler, *Clogging in constricted suspension flows*, *Physical Review E* **97** (feb, 2018).

[72] J. R. Valdes and J. C. Santamarina, *Clogging: bridge formation and vibration-based destabilization*, *Canadian Geotechnical Journal* **45** (2008), no. 2 177–184, [https://doi.org/10.1139/T07-088].

[73] B. Mustin and B. Stoeber, *Single layer deposition of polystyrene particles onto planar polydimethylsiloxane substrates*, *Langmuir* **32** (2016), no. 1 88–101.

[74] R. Arvalo and I. Zuriguel, *Clogging of granular materials in silos: effect of gravity and outlet size*, *Soft Matter* **12** (2016) 123–130.

[75] S. Khodaparast, M. K. Kim, J. E. Silpe, and H. A. Stone, *Bubble-Driven Detachment of Bacteria from Confined Microgeometries*, *Environmental Science & Technology* **51** (feb, 2017) 1340–1347.

[76] B. Dincau, C. Tang, E. Dressaire, and A. Sauret, *Clog mitigation in a microfluidic array via pulsatile flows*, *Soft Matter* **18** (2022) 1767–1778.

[77] N. Yogarajah and S. S. H. Tsai, *Detection of trace arsenic in drinking water: challenges and opportunities for microfluidics*, *Environmental Science: Water Research & Technology* **1** (2015), no. 4 426–447.

[78] L. KANG, *Microfluidics for drug discovery and development: From target selection to product lifecycle management*, *Drug Discovery Today* **13** (jan, 2008) 1–13.

[79] X. Mao and T. J. Huang, *Microfluidic diagnostics for the developing world*, *Lab on a Chip* **12** (2012), no. 8 1412.

[80] P. S. Dittrich and A. Manz, *Lab-on-a-chip: microfluidics in drug discovery*, *Nature Reviews Drug Discovery* **5** (2006), no. 3 210–218.

[81] E. Bassous, H. H. Taub, and L. Kuhn, *Ink jet printing nozzle arrays etched in silicon*, *Applied Physics Letters* **31** (jul, 1977) 135–137.

[82] C. W. S. IV, C. D. Reyes, and G. P. López, *Microfluidic cell sorting: a review of the advances in the separation of cells from debulking to rare cell isolation*, *Lab on a Chip* **15** (2015), no. 5 1230–1249.

[83] B. Zhao, X. Cui, W. Ren, F. Xu, M. Liu, and Z.-G. Ye, *A Controllable and Integrated Pump-enabled Microfluidic Chip and Its Application in Droplets Generating*, *Scientific Reports* **7** (sep, 2017).

[84] G. Luka, A. Ahmadi, H. Najjaran, E. Alocilja, M. DeRosa, K. Wolthers, A. Malki, H. Aziz, A. Althani, and M. Hoorfar, *Microfluidics Integrated Biosensors: A Leading Technology towards Lab-on-a-Chip and Sensing Applications*, *Sensors* **15** (dec, 2015) 30011–30031.

[85] R. Seemann, M. Brinkmann, T. Pfohl, and S. Herminghaus, *Droplet based microfluidics*, *Reports on Progress in Physics* **75** (dec, 2011) 16601.

[86] G. M. Walker and D. J. Beebe, *A passive pumping method for microfluidic devices*, *Lab on a Chip* **2** (2002), no. 3 131.

[87] D. J. Laser and J. G. Santiago, *A review of micropumps*, *Journal of Micromechanics and Microengineering* **14** (apr, 2004) R35———R64.

[88] Y.-N. Wang and L.-M. Fu, *Micropumps and biomedical applications –a review*, *Microelectronic Engineering* **195** (aug, 2018) 121–138.

[89] R. J. Meagher, Y. K. Light, and A. K. Singh, *Rapid, continuous purification of proteins in a microfluidic device using genetically-engineered partition tags*, *Lab on a Chip* **8** (2008), no. 4 527.

[90] M. Sonker, V. Sahore, and A. T. Woolley, *Recent advances in microfluidic sample preparation and separation techniques for molecular biomarker analysis: A critical review*, *Analytica Chimica Acta* **986** (sep, 2017) 1–11.

[91] T. M. Squires and S. R. Quake, *Microfluidics: Fluid physics at the nanoliter scale*, *Rev. Mod. Phys.* **77** (oct, 2005) 977–1026.

[92] J. Wang, V. G. J. Rodgers, P. Brisk, and W. H. Grover, *Instantaneous simulation of fluids and particles in complex microfluidic devices*, *PLOS ONE* **12** (dec, 2017) e0189429.

[93] D. Di Carlo, D. Irimia, R. G. Tompkins, and M. Toner, *Continuous inertial focusing, ordering, and separation of particles in microchannels*, *Proceedings of the National Academy of Sciences* **104** (nov, 2007) 18892–18897.

[94] J. Cruz, S. H. Zadeh, T. Graells, M. Andersson, J. Malmström, Z. G. Wu, and K. Hjort, *High pressure inertial focusing for separating and concentrating bacteria at high throughput*, *Journal of Micromechanics and Microengineering* **27** (jun, 2017) 84001.

[95] E.-C. Yeh, C.-C. Fu, L. Hu, R. Thakur, J. Feng, and L. P. Lee, *Self-powered integrated microfluidic point-of-care low-cost enabling (SIMPLE) chip*, *Science Advances* **3** (mar, 2017) e1501645.

[96] G. Cai, L. Xue, H. Zhang, and J. Lin, *A Review on Micromixers*, *Micromachines* **8** (sep, 2017) 274.

[97] M. Abolhasani and K. F. Jensen, *Oscillatory multiphase flow strategy for chemistry and biology*, *Lab on a Chip* **16** (2016), no. 15 2775–2784.

[98] K. Ward and Z. H. Fan, *Mixing in microfluidic devices and enhancement methods*, *Journal of Micromechanics and Microengineering* **25** (aug, 2015) 94001.

[99] P. Zhu and L. Wang, *Passive and active droplet generation with microfluidics: a review*, *Lab on a Chip* **17** (2017), no. 1 34–75.

[100] D. Cheng, Y. Yu, C. Han, M. Cao, G. Yang, J. Liu, X. Chen, and Z. Peng, *A simple microdevice for single cell capture, array, release, and fast staining using oscillatory method*, *Biomicrofluidics* **12** (may, 2018) 34105.

[101] N. Mehendale, O. Sharma, S. Pandey, and D. Paul, *Clogging-free continuous operation with whole blood in a radial pillar device (RAPID)*, *Biomedical Microdevices* **20** (aug, 2018).

[102] Y. Yoon, S. Kim, J. Lee, J. Choi, R.-K. Kim, S.-B. S.-J. S.-B. S.-J. S.-B. Lee, O. Sul, and S.-B. S.-J. S.-B. S.-J. S.-B. Lee, *Clogging-free microfluidics for continuous size-based separation of microparticles*, *Scientific Reports* **6** (may, 2016).

[103] C. G. Caro, *The Mechanics of the Circulation*. Cambridge University Press, 2011.

[104] S. Vogel, *Life in Moving Fluids 2nd Ed.* Princeton University Press, 1994.

[105] C. F. Dewey Jr., S. R. Bussolari, M. A. Gimbrone Jr., and P. F. Davies, *The Dynamic Response of Vascular Endothelial Cells to Fluid Shear Stress*, *Journal of Biomechanical Engineering* **103** (aug, 1981) 177–185.

[106] C. T. Hung, S. R. Pollack, T. M. Reilly, and C. T. Brighton, *Real-time calcium response of cultured bone cells to fluid flow.*, *Clinical orthopaedics and related research* (1995), no. 313 256–269.

[107] Y. Liu and J.-H. Tay, *Metabolic response of biofilm to shear stress in fixed-film culture*, *Journal of applied microbiology* **90** (2001), no. 3 337–342.

[108] J. R. Womersley, *Method for the calculation of velocity, rate of flow and viscous drag in arteries when the pressure gradient is known*, *The Journal of Physiology* **127** (mar, 1955) 553–563.

[109] J. R. Womersley, *Oscillatory Flow in Arteries: the Constrained Elastic Tube as a Model of Arterial Flow and Pulse Transmission*, *Physics in Medicine and Biology* **2** (oct, 1957) 178–187.

[110] C. J. Morris and F. K. Forster, *Oscillatory flow in microchannels*, *Experiments in Fluids* **36** (jun, 2004) 928–937.

[111] F. Sharipov and D. Kalempa, *Oscillatory Couette flow at arbitrary oscillation frequency over the whole range of the Knudsen number*, *Microfluidics and Nanofluidics* **4** (jun, 2007) 363–374.

[112] Y. Lee, D.-M. Kim, Z. Li, D.-E. Kim, and S.-J. Kim, *Pulsatile plasma filtration and cell-free DNA amplification using a water-head-driven point-of-care testing chip*, *Lab on a Chip* **18** (2018), no. 6 915–922.

[113] J. Shao, L. Wu, J. Wu, Y. Zheng, H. Zhao, Q. Jin, and J. Zhao, *Integrated microfluidic chip for endothelial cells culture and analysis exposed to a pulsatile and oscillatory shear stress*, *Lab on a Chip* **9** (2009), no. 21 3118.

[114] B. Mosadegh, C.-H. Kuo, Y.-C. Tung, Y.-s. Torisawa, T. Bersano-Begey, H. Tavana, and S. Takayama, *Integrated elastomeric components for autonomous regulation of sequential and oscillatory flow switching in microfluidic devices*, *Nature Physics* **6** (apr, 2010) 433–437.

[115] V. B. Dang and S.-J. Kim, *Water-head-driven microfluidic oscillators for autonomous control of periodic flows and generation of aqueous two-phase system droplets*, *Lab on a Chip* **17** (2017), no. 2 286–292.

[116] S.-J. Kim, R. Yokokawa, S. Cai Lesher-Perez, and S. Takayama, *Multiple independent autonomous hydraulic oscillators driven by a common gravity head*, *Nature Communications* **6** (nov, 2015) 7301.

[117] E. W. Simões, R. Furlan, R. E. B. Leminski, M. R. Gongora-Rubio, M. T. Pereira, N. I. Morimoto, and J. J. S. Avilés, *Microfluidic oscillator for gas flow control and measurement*, *Flow Measurement and Instrumentation* **16** (mar, 2005) 7–12.

[118] P. N. Duncan, T. V. Nguyen, and E. E. Hui, *Pneumatic oscillator circuits for timing and control of integrated microfluidics*, *Proceedings of the National Academy of Sciences* **110** (nov, 2013) 18104–18109.

[119] R. Yoshida, H. Ichijo, T. Hakuta, and T. Yamaguchi, *Self-oscillating swelling and deswelling of polymer gels*, *Macromolecular Rapid Communications* **16** (apr, 1995) 305–310.

[120] G. Paschew, J. Schreiter, A. Voigt, C. Pini, J. P. Chávez, M. Allerdißen, U. Marschner, S. Siegmund, R. Schüffny, F. Jülicher, and A. Richter, *Autonomous Chemical Oscillator Circuit Based on Bidirectional Chemical-Microfluidic Coupling*, *Advanced Materials Technologies* **1** (apr, 2016) 1600005.

[121] S.-C. Chan, C.-R. Chen, and C.-H. Liu, *A bubble-activated micropump with high-frequency flow reversal*, *Sensors and Actuators A: Physical* **163** (oct, 2010) 501–509.

[122] J.-H. Tsai and L. Lin, *Active microfluidic mixer and gas bubble filter driven by thermal bubble micropump*, *Sensors and Actuators A: Physical* **97-98** (apr, 2002) 665–671.

[123] B. Liu, J. Sun, D. Li, J. Zhe, and K. W. Oh, *A high flow rate thermal bubble-driven micropump with induction heating*, *Microfluidics and Nanofluidics* **20** (nov, 2016).

[124] L.-S. Jang, S.-H. Chao, M. R. Holl, and D. R. Meldrum, *Microfluidic circulatory flows induced by resonant vibration of diaphragms*, *Sensors and Actuators A: Physical* **122** (jul, 2005) 141–148.

[125] J. Xu and D. Attinger, *Piezoelectric Actuation in Multiphase Microfluidics*, in *Encyclopedia of Microfluidics and Nanofluidics*, pp. 1–10. Springer US, 2013.

[126] J. Kedzierski, S. Berry, and B. Abedian, *New Generation of Digital Microfluidic Devices*, *Journal of Microelectromechanical Systems* **18** (aug, 2009) 845–851.

[127] F. Mugele and J.-C. Baret, *Electrowetting: from basics to applications*, *Journal of Physics: Condensed Matter* (2005).

[128] A. Klingner, S. Herminghaus, and F. Mugele, *Self-excited oscillatory dynamics of capillary bridges in electric fields*, *Applied Physics Letters* **82** (jun, 2003) 4187–4189.

[129] F. Mugele, J.-C. Baret, and D. Steinhauser, *Microfluidic mixing through electrowetting-induced droplet oscillations*, *Applied Physics Letters* **88** (may, 2006) 204106.

[130] K. Bengtsson, J. Christoffersson, C.-F. Mandenius, and N. D. Robinson, *A clip-on electroosmotic pump for oscillating flow in microfluidic cell culture devices*, *Microfluidics and Nanofluidics* **22** (feb, 2018).

[131] B. J. Kirby, *Micro- And Nanoscale Fluid Mechanics*. Cambridge University Press, 2010.

[132] G. Ramon, Y. Agnon, and C. Dosoretz, *Solute dispersion in oscillating electro-osmotic flow with boundary mass exchange*, *Microfluidics and Nanofluidics* **10** (jun, 2010) 97–106.

[133] J. C. Misra, S. Chandra, G. C. Shit, and P. K. Kundu, *Electroosmotic oscillatory flow of micropolar fluid in microchannels: application to dynamics of blood flow in microfluidic devices*, *Applied Mathematics and Mechanics* **35** (may, 2014) 749–766.

[134] M. Peralta, J. Arcos, F. Méndez, and O. Bautista, *Oscillatory electroosmotic flow in a parallel-plate microchannel under asymmetric zeta potentials*, *Fluid Dynamics Research* **49** (may, 2017) 35514.

[135] I. Medina, M. Toledo, F. Méndez, and O. Bautista, *Pulsatile electroosmotic flow in a microchannel with asymmetric wall zeta potentials and its effect on mass transport enhancement and mixing*, *Chemical Engineering Science* **184** (jul, 2018) 259–272.

[136] J. H. Kim, T. Y. Jeon, T. M. Choi, T. S. Shim, S.-H. Kim, and S.-M. Yang, *Droplet Microfluidics for Producing Functional Microparticles*, *Langmuir* **30** (nov, 2013) 1473–1488.

[137] T. Kong, J. Wu, M. To, K. Wai Kwok Yeung, H. Cheung Shum, and L. Wang, *Droplet based microfluidic fabrication of designer microparticles for encapsulation applications*, *Biomicrofluidics* **6** (sep, 2012) 34104.

[138] R. K. Shah, H. C. Shum, A. C. Rowat, D. Lee, J. J. Agresti, A. S. Utada, L.-Y. Chu, J.-W. Kim, A. Fernandez-Nieves, C. J. Martinez, and D. A. Weitz, *Designer emulsions using microfluidics*, *Materials Today* **11** (apr, 2008) 18–27.

[139] N. Shembekar, C. Chaipan, R. Utharala, and C. A. Merten, *Droplet-based microfluidics in drug discovery, transcriptomics and high-throughput molecular genetics*, *Lab on a Chip* **16** (2016), no. 8 1314–1331.

[140] T. S. Kaminski and P. Garstecki, *Controlled droplet microfluidic systems for multistep chemical and biological assays*, *Chemical Society Reviews* **46** (2017), no. 20 6210–6226.

[141] T. P. Lagus and J. F. Edd, *High-throughput co-encapsulation of self-ordered cell trains: cell pair interactions in microdroplets*, *RSC Advances* **3** (2013), no. 43 20512.

[142] A. M. Klein, L. Mazutis, I. Akartuna, N. Tallapragada, A. Veres, V. Li, L. Peshkin, D. A. Weitz, and M. W. Kirschner, *Droplet Barcoding for Single-Cell Transcriptomics Applied to Embryonic Stem Cells*, *Cell* **161** (may, 2015) 1187–1201.

[143] S. Köster, F. E. Angilè, H. Duan, J. J. Agresti, A. Wintner, C. Schmitz, A. C. Rowat, C. A. Merten, D. Pisignano, A. D. Griffiths, and D. A. Weitz, *Drop-based microfluidic devices for encapsulation of single cells*, *Lab on a Chip* **8** (2008), no. 7 1110.

[144] J. Clausell-Tormos, D. Lieber, J.-C. Baret, A. El-Harrak, O. J. Miller, L. Frenz, J. Blouwolff, K. J. Humphry, S. Köster, H. Duan, C. Holtze, D. A. Weitz, A. D. Griffiths, and C. A. Merten, *Droplet-Based Microfluidic Platforms for the Encapsulation and Screening of Mammalian Cells and Multicellular Organisms*, *Chemistry & Biology* **15** (may, 2008) 427–437.

[145] S.-Y. Teh, R. Lin, L.-H. Hung, and A. P. Lee, *Droplet microfluidics*, *Lab on a Chip* **8** (2008), no. 2 198.

[146] D. R. Link, E. Grasland-Mongrain, A. Duri, F. Sarrazin, Z. Cheng, G. Cristobal, M. Marquez, and D. A. Weitz, *Electric Control of Droplets in Microfluidic Devices*, *Angewandte Chemie International Edition* **45** (apr, 2006) 2556–2560.

[147] Z. Li, S. Y. Mak, A. Sauret, and H. C. Shum, *Syringe-pump-induced fluctuation in all-aqueous microfluidic system implications for flow rate accuracy*, *Lab on a Chip* **14** (2014), no. 4 744–749.

[148] A. Sauret and H. Cheung Shum, *Forced generation of simple and double emulsions in all-aqueous systems*, *Applied Physics Letters* **100** (2012), no. 15 154106.

[149] A. S. Utada, A. Fernandez-Nieves, H. A. Stone, and D. A. Weitz, *Dripping to Jetting Transitions in Coflowing Liquid Streams*, *Physical Review Letters* **99** (aug, 2007) 94502.

[150] Z. Zhang, T. Kong, C. Zhou, and L. Wang, *Engineering the Flow of Liquid Two-Phase Systems by Passive Noise Control*, *Physical Review Applied* **9** (feb, 2018) 24036.

[151] A. Khoshnevis, S. S. H. Tsai, and E. Esmaeilzadeh, *Electric field induced sheeting and breakup of dielectric liquid jets*, *Physics of Fluids* **26** (jan, 2014) 12103.

[152] S. D. Geschiere, I. Ziemecka, V. van Steijn, G. J. M. Koper, J. H. van Esch, and M. T. Kreutzer, *Slow growth of the Rayleigh-Plateau instability in aqueous two phase systems*, *Biomicrofluidics* **6** (2012), no. 2 22007.

[153] C. Li, Y. Zhang, and C. Yehuda, *Individual based modeling of Pseudomonas aeruginosa biofilm with three detachment mechanisms*, *RSC Advances* **5** (2015), no. 96 79001–79010.

[154] S. Hardt and T. Hahn, *Microfluidics with aqueous two-phase systems*, *Lab on a Chip* **12** (2012), no. 3 434–442.

[155] Y. Song, A. Sauret, and H. Cheung Shum, *All-aqueous multiphase microfluidics*, *Biomicrofluidics* **7** (2013), no. 6 61301.

[156] B.-U. Moon, S. G. Jones, D. K. Hwang, and S. S. H. Tsai, *Microfluidic generation of aqueous two-phase system (ATPS) droplets by controlled pulsating inlet pressures*, *Lab on a Chip* **15** (2015), no. 11 2437–2444.

[157] I. Ziemecka, V. van Steijn, G. J. M. Koper, M. Rosso, A. M. Brizard, J. H. van Esch, and M. T. Kreutzer, *Monodisperse hydrogel microspheres by forced droplet formation in aqueous two-phase systems*, *Lab on a Chip* **11** (2011), no. 4 620–624.

[158] A. Sauret, C. Spandagos, and H. C. Shum, *Fluctuation-induced dynamics of multiphase liquid jets with ultra-low interfacial tension*, *Lab on a Chip* **12** (2012), no. 18 3380–3386.

[159] H. C. Shum, J. Varnell, and D. A. Weitz, *Microfluidic fabrication of water-in-water (w/w) jets and emulsions*, *Biomicrofluidics* **6** (2012), no. 1 12808.

[160] P. Zhu, X. Tang, Y. Tian, and L. Wang, *Pinch-off of microfluidic droplets with oscillatory velocity of inner phase flow*, *Scientific reports* **6** (2016) 31436.

[161] P. Zhu, X. Tang, and L. Wang, *Droplet generation in co-flow microfluidic channels with vibration*, *Microfluidics and Nanofluidics* **20** (feb, 2016).

[162] P. Zhu and L. Wang, *Droplet pinch-off with pressure fluctuations*, *Chemical Engineering Science* **196** (mar, 2019) 333–343.

[163] C. Zhou, P. Zhu, Y. Tian, X. Tang, R. Shi, and L. Wang, *Microfluidic generation of aqueous two-phase-system (ATPS) droplets by oil-droplet choppers*, *Lab on a Chip* **17** (2017), no. 19 3310–3317.

[164] S. Y. Mak, Y. Chao, S. Rahman, and H. C. Shum, *Droplet Formation by Rupture of Vibration-Induced Interfacial Fingers*, *Langmuir* **34** (nov, 2017) 926–932.

[165] K. Chaudhury, S. Mandal, and S. Chakraborty, *Droplet migration characteristics in confined oscillatory microflows*, *Physical Review E* **93** (feb, 2016).

[166] J. M. Ottino and S. Wiggins, *Introduction: mixing in microfluidics*, *Philosophical Transactions of the Royal Society of London. Series A: Mathematical, Physical and Engineering Sciences* **362** (may, 2004) 923–935.

[167] Y. K. Suh and S. Kang, *A Review on Mixing in Microfluidics*, *Micromachines* **1** (sep, 2010) 82–111.

[168] Z. Li and S.-J. Kim, *Pulsatile micromixing using water-head-driven microfluidic oscillators*, *Chemical Engineering Journal* **313** (apr, 2017) 1364–1369.

[169] R. A. Truesdell, P. V. Vorobieff, L. A. Sklar, and A. A. Mammoli, *Mixing of a continuous flow of two fluids due to unsteady flow*, *Physical Review E* **67** (jun, 2003).

[170] J. W. Wu, H. M. Xia, Y. Y. Zhang, and P. Zhu, *Microfluidic mixing through oscillatory transverse perturbations*, *Modern Physics Letters B* **32** (may, 2018) 1840030.

[171] A. Afzal and K.-Y. Kim, *Convergent –divergent micromixer coupled with pulsatile flow*, *Sensors and Actuators B: Chemical* **211** (may, 2015) 198–205.

[172] F. R. Phelan, N. R. Hughes, and J. A. Pathak, *Chaotic mixing in microfluidic devices driven by oscillatory cross flow*, *Physics of Fluids* **20** (feb, 2008) 23101.

[173] Z. B. Stone and H. A. Stone, *Imaging and quantifying mixing in a model droplet micromixer*, *Physics of Fluids* **17** (jun, 2005) 63103.

[174] H. Kinoshita, S. Kaneda, T. Fujii, and M. Oshima, *Three-dimensional measurement and visualization of internal flow of a moving droplet using confocal micro-PIV*, *Lab Chip* **7** (2007), no. 3 338–346.

[175] F. Sarrazin, L. Prat, N. D. Miceli, G. Cristobal, D. R. Link, and D. A. Weitz, *Mixing characterization inside microdroplets engineered on a microcoalescer*, *Chemical Engineering Science* **62** (feb, 2007) 1042–1048.

[176] Y. W. Kim and J. Y. Yoo, *Transport of solid particles in microfluidic channels*, *Optics and Lasers in Engineering* **50** (jan, 2012) 87–98.

[177] Y.-L. Chen, M. D. Graham, J. J. de Pablo, K. Jo, and D. C. Schwartz, *DNA Molecules in Microfluidic Oscillatory Flow*, *Macromolecules* **38** (jul, 2005) 6680–6687.

[178] C. Liu and G. Hu, *High-Throughput Particle Manipulation Based on Hydrodynamic Effects in Microchannels*, *Micromachines* **8** (mar, 2017) 73.

[179] S. M. McFaul, B. K. Lin, and H. Ma, *Cell separation based on size and deformability using microfluidic funnel ratchets*, *Lab on a Chip* **12** (2012), no. 13 2369.

[180] Y. Yoon, J. Lee, M. Ra, H. Gwon, S. Lee, M. Y. Kim, K.-C. Yoo, O. Sul, C. G. Kim, W.-Y. Kim, J.-G. Park, S.-J. Lee, Y. Y. Lee, H. S. Choi, and S.-B. Lee, *Continuous Separation of Circulating Tumor Cells from Whole Blood Using a Slanted Weir Microfluidic Device*, *Cancers* **11** (feb, 2019) 200.

[181] Z. Zhang, J. Xu, B. Hong, and X. Chen, *The effects of 3D channel geometry on CTC passing pressure towards deformability-based cancer cell separation*, *Lab Chip* **14** (2014), no. 14 2576–2584.

[182] J. S. Kuo, Y. Zhao, P. G. Schiro, L. Ng, D. S. W. Lim, J. P. Shelby, and D. T. Chiu, *Deformability considerations in filtration of biological cells*, *Lab on a Chip* **10** (2010), no. 7 837.

[183] E. S. Park, C. Jin, Q. Guo, R. R. Ang, S. P. Duffy, K. Matthews, A. Azad, H. Abdi, T. Todenhöfer, J. Bazov, K. N. Chi, P. C. Black, and H. Ma, *Continuous Flow Deformability-Based Separation of Circulating Tumor Cells Using Microfluidic Ratchets*, *Small* **12** (apr, 2016) 1909–1919.

[184] J. Lee, S. E. Mena, and M. A. Burns, *Micro-Particle Operations Using Asymmetric Traps*, *Scientific Reports* **9** (feb, 2019).

[185] D. Di Carlo, *Inertial microfluidics*, *Lab Chip* **9** (2009) 3038–3046.

[186] B. R. Mutlu, J. F. Edd, and M. Toner, *Oscillatory inertial focusing in infinite microchannels*, *Proceedings of the National Academy of Sciences* **115** (jul, 2018) 7682–7687.

[187] C. Dietsche, B. R. Mutlu, J. F. Edd, P. Koumoutsakos, and M. Toner, *Dynamic particle ordering in oscillatory inertial microfluidics*, *Microfluidics and Nanofluidics* **23** (may, 2019).

[188] B. Dersoir, A. B. Schofield, M. R. de Saint Vincent, and H. Tabuteau, *Dynamics of pore fouling by colloidal particles at the particle level*, *Journal of Membrane Science* **573** (mar, 2019) 411–424.

[189] Y. Cheng, X. Ye, Z. Ma, S. Xie, and W. Wang, *High-throughput and clogging-free microfluidic filtration platform for on-chip cell separation from undiluted whole blood*, *Biomicrofluidics* **10** (jan, 2016) 14118.

[190] J. Lee, Z. Estlack, H. Somaweera, X. Wang, C. M. R. Lacerda, and J. Kim, *A microfluidic cardiac flow profile generator for studying the effect of shear stress on valvular endothelial cells*, *Lab on a Chip* **18** (2018), no. 19 2946–2954.

[191] E. K. Sackmann, A. L. Fulton, and D. J. Beebe, *The present and future role of microfluidics in biomedical research*, *Nature* **507** (mar, 2014) 181–189.

[192] C. Situma, M. Hashimoto, and S. A. Soper, *Merging microfluidics with microarray-based bioassays*, *Biomolecular engineering* **23** (2006), no. 5 213–231.

[193] F. Su, K. Chakrabarty, and R. B. Fair, *Microfluidics-based biochips: technology issues, implementation platforms, and design-automation challenges*, *IEEE Transactions on computer-aided design of integrated circuits and systems* **25** (2006), no. 2 211–223.

[194] S. K. Hartwell and K. Grudpan, *Flow based immuno/bioassay and trends in micro-immuno/biosensors*, *Microchimica Acta* **169** (2010), no. 3-4 201–220.

[195] C. Hahn and M. A. Schwartz, *Mechanotransduction in vascular physiology and atherogenesis*, *Nature Reviews Molecular Cell Biology* **10** (jan, 2009) 53–62.

[196] W. Zheng, B. Jiang, D. Wang, W. Zhang, Z. Wang, and X. Jiang, *A microfluidic flow-stretch chip for investigating blood vessel biomechanics*, *Lab on a Chip* **12** (2012), no. 18 3441.

[197] S. Chien, *Mechanotransduction and endothelial cell homeostasis: the wisdom of the cell*, *American Journal of Physiology-Heart and Circulatory Physiology* **292** (mar, 2007) H1209———H1224.

[198] H. H. Lipowsky, S. Kovalcheck, and B. W. Zweifach, *The distribution of blood rheological parameters in the microvasculature of cat mesentery.*, *Circulation Research* **43** (nov, 1978) 738–749.

[199] S. C. Herbert H. Lipowsky Shunichi Usami, *In Vivo and Measurements of Apparent and Viscosity and Microvessel Hematocrit in the Mesentery and of the Cat*, *MICROVASCULAR RESEARCH* (1980).

[200] N. Wang, H. Miao, Y.-S. Li, P. Zhang, J. H. Haga, Y. Hu, A. Young, S. Yuan, P. Nguyen, C.-C. Wu, and S. Chien, *Shear stress regulation of Krüppel-like factor 2 expression is flow pattern-specific*, *Biochemical and Biophysical Research Communications* **341** (mar, 2006) 1244–1251.

[201] D. Guo, S. Chien, and J. Y.-J. Shyy, *Regulation of Endothelial Cell Cycle by Laminar Versus Oscillatory Flow*, *Circulation Research* **100** (mar, 2007) 564–571.

[202] J. J. Chiu, D. L. Wang, S. Chein, R. Skalak, and S. Usami, *Effects of Disturbed Flow on Endothelial Cells*, *Journal of Biomechanical Engineering* (1998), no. reattach-.

[203] C. W. Ni, H. Qiu, and H. Jo, *MicroRNA-663 upregulated by oscillatory shear stress plays a role in inflammatory response of endothelial cells*, *American Journal of Physiology-Heart and Circulatory Physiology* **300** (may, 2011) H1762———H1769.

[204] F. Wang, Z. Wang, J. Pu, X. Xie, X. Gao, Y. Gu, S. Chen, and J. Zhang, *Oscillating flow promotes inflammation through the TLR2–TAK1–IKK2 signalling pathway in human umbilical vein endothelial cell (HUVECs)*, *Life Sciences* **224** (may, 2019) 212–221.

[205] S. C. M. Yu, *Steady and pulsatile Flow studies in Abdominal Aortic Aneurysm models using Particle Image Velocimetry*, *International Journal of Heat and Fluid Flow* (2000).

[206] J. Ribas, H. Sadeghi, A. Manbachi, J. Leijten, K. Brinegar, Y. S. Zhang, L. Ferreira, and A. Khademhosseini, *Cardiovascular Organ-on-a-Chip Platforms for Drug Discovery and Development*, *Applied In Vitro Toxicology* **2** (jun, 2016) 82–96.

[207] K. Nakamori, M. Odawara, T. Nakajima, T. Mizutani, and K. Tsubota, *Blinking is controlled primarily by ocular surface conditions*, *American journal of ophthalmology* **124** (1997), no. 1 24–30.

[208] U. Hampel, F. Garreis, F. Burgemeister, N. Eßel, and F. Paulsen, *Effect of intermittent shear stress on corneal epithelial cells using an in vitro flow culture model*, *The Ocular Surface* **16** (jul, 2018) 341–351.

[209] D. S. Weigle, D. J. Koerker, and C. J. Goodner, *Pulsatile glucagon delivery enhances glucose production by perifused rat hepatocytes*, *American Journal of Physiology-Endocrinology and Metabolism* **247** (oct, 1984) E564—-E568.

[210] G. Brabant, K. Prank, and C. Schofl, *Pulsatile patterns in hormone secretion*, *Trends in Endocrinology & Metabolism* **3** (jul, 1992) 183–190.

[211] A. Goldbeter and M. J. Berridge, *Biochemical Oscillations And Cellular Rhythms*. Cambridge University Press, Cambridge, 1996.

[212] A. Jovic, B. Howell, and S. Takayama, *Timing is everything: using fluidics to understand the role of temporal dynamics in cellular systems*, *Microfluidics and Nanofluidics* **6** (jun, 2009) 717–729.

[213] M. M. M. Pool, V. E. A. Post, and C. T. Simmons, *Effects of tidal fluctuations and spatial heterogeneity on mixing and spreading in spatially heterogeneous coastal aquifers*, *Water Resources Research* **51** (mar, 2015) 1570–1585.

[214] D. C. Miller, M. J. Bock, and E. J. Turner, *Deposit and suspension feeding in oscillatory flows and sediment fluxes*, *Journal of Marine Research* **50** (aug, 1992) 489–520.

[215] R. Ghosh, G. A. Buxton, O. B. Usta, A. C. Balazs, and A. Alexeev, *Designing Oscillating Cilia That Capture or Release Microscopic Particles*, *Langmuir* **26** (feb, 2010) 2963–2968.

[216] J. Han and C. S. Peskin, *Spontaneous oscillation and fluid –structure interaction of cilia*, *Proceedings of the National Academy of Sciences* **115** (apr, 2018) 4417–4422.

[217] S. Uppaluri, N. Heddergott, E. Stellamanns, S. Herminghaus, A. Zöttl, H. Stark, M. Engstler, and T. Pfohl, *Flow Loading Induces Oscillatory Trajectories in a Bloodstream Parasite*, *Biophysical Journal* **103** (sep, 2012) 1162–1169.

[218] J. Elgeti, R. G. Winkler, and G. Gompper, *Physics of microswimmers$textemdashsingle particle motion and collective behavior: a review*, *Reports on Progress in Physics* **78** (apr, 2015) 56601.

[219] J. W. Haycock, *3D cell culture: a review of current approaches and techniques*, in *3D cell culture*, pp. 1–15. Springer, 2011.

[220] M. Ni, W. H. Tong, D. Choudhury, N. A. A. Rahim, C. Iliescu, and H. Yu, *Cell culture on MEMS platforms: a review*, *International journal of molecular sciences* **10** (2009), no. 12 5411–5441.

[221] L. C. Espinha, D. A. Hoey, P. R. Fernandes, H. C. Rodrigues, and C. R. Jacobs, *Oscillatory fluid flow influences primary cilia and microtubule mechanics*, *Cytoskeleton* **71** (jul, 2014) 435–445.

[222] C. R. White and J. A. Frangos, *The shear stress of it all: the cell membrane and mechanochemical transduction*, *Philosophical Transactions of the Royal Society B: Biological Sciences* **362** (aug, 2007) 1459–1467.

[223] P. H. Krebsbach, S. A. Kuznetsov, P. Bianco, and P. G. Robey, *Bone Marrow Stromal Cells: Characterization and Clinical Application*, *Critical Reviews in Oral Biology & Medicine* **10** (apr, 1999) 165–181.

[224] Y. J. Li, N. N. Batra, L. You, S. C. Meier, I. A. Coe, C. E. Yellowley, and C. R. Jacobs, *Oscillatory fluid flow affects human marrow stromal cell proliferation and differentia tion*, *Journal of Orthopaedic and Research* (2004).

[225] Y. S. Morsi, W. W. Yang, A. Owida, and C. S. Wong, *Development of a novel pulsatile bioreactor for tissue culture*, *Journal of Artificial Organs* **10** (jun, 2007) 109–114.

[226] B. A. Nasseri, I. Pomerantseva, M. R. Kaazempur-Mofrad, F. W. H. Sutherland, T. Perry, E. Ochoa, C. A. Thompson, J. E. Mayer, S. N. Oesterle, and J. P. Vacanti, *Dynamic Rotational Seeding and Cell Culture System for Vascular Tube Formation*, *Tissue Engineering* **9** (apr, 2003) 291–299.

[227] K. Dumont, J. Yperman, E. Verbeken, P. Segers, B. Meuris, S. Vandenberghe, W. Flameng, and P. R. Verdonck, *Design of a New Pulsatile Bioreactor for Tissue Engineered Aortic Heart Valve Formation*, *Artificial Organs* **26** (aug, 2002) 710–714.

[228] D. Du, K. S. Furukawa, and T. Ushida, *3D culture of osteoblast-like cells by unidirectional or oscillatory flow for bone tissue engineering*, *Biotechnology and Bioengineering* **102** (apr, 2009) 1670–1678.

[229] N. L. of Enteric Pathogens, *The polymerase chain reaction: An overview and development of diagnostic PCR protocols at the LCDC*, *The Canadian journal of infectious diseases = Journal canadien des maladies infectieuses* **2** (1991), no. 22529715 89–91.

[230] P. Markoulatos, N. Siafakas, and M. Moncany, *Multiplex polymerase chain reaction: A practical approach*, *Journal of Clinical Laboratory Analysis* **16** (2002), no. 1 47–51.

[231] C. Zhang and D. Xing, *Miniaturized PCR chips for nucleic acid amplification and analysis: latest advances and future trends*, *Nucleic Acids Research* **35** (jun, 2007) 4223–4237.

[232] M. U. Kopp, *Chemical Amplification: Continuous-Flow PCR on a Chip*, *Science* **280** (may, 1998) 1046–1048.

[233] H. Wang, C. Zhang, and D. Xing, *Simultaneous detection of Salmonella enterica, Escherichia coli O157:H7, and Listeria monocytogenes using oscillatory-flow multiplex PCR*, *Microchimica Acta* **173** (mar, 2011) 503–512.

[234] C. Zhang, H. Wang, and D. Xing, *Multichannel oscillatory-flow multiplex PCR microfluidics for high-throughput and fast detection of foodborne bacterial pathogens*, *Biomedical Microdevices* **13** (jun, 2011) 885–897.

[235] W. Wang, Z.-X. Li, R. Luo, S.-H. Lü, A.-D. Xu, and Y.-J. Yang, *Droplet-based micro oscillating-flow PCR chip*, *Journal of Micromechanics and Microengineering* **15** (may, 2005) 1369–1377.

[236] H.-Y. WANG, C.-S. ZHANG, and Y.-Y. LI, *Rapid Detection of Tobacco Mosaic Virus from Crude Samples on an Oscillatory-flow Reverse Transcription-Polymerase Chain Reaction Microfluidics*, *Chinese Journal of Analytical Chemistry* **37** (sep, 2009) 1286–1290.

[237] J. Nie, Y. Zhao, and N. Peng, *Multichannel oscillatory-flow PCR micro-fluidic chip with controllable temperature gradient*, *Microsystem Technologies* **21** (jan, 2014) 41–48.

[238] K. Vijayakumar, S. Gulati, A. J. DeMello, and J. B. Edel, *Rapid cell extraction in aqueous two-phase microdroplet systems*, *Chemical Science* **1** (2010), no. 4 447.

[239] J. P. Frampton, D. Lai, H. Sriram, and S. Takayama, *Precisely targeted delivery of cells and biomolecules within microchannels using aqueous two-phase systems*, *Biomedical Microdevices* **13** (jul, 2011) 1043–1051.

[240] C. E. Owens and A. J. Hart, *High-precision modular microfluidics by micromilling of interlocking injection-molded blocks*, *Lab on a Chip* **18** (2018), no. 6 890–901.

[241] Q. Ji, J. M. Zhang, Y. Liu, X. Li, P. Lv, D. Jin, and H. Duan, *A Modular Microfluidic Device via Multimaterial 3D Printing for Emulsion Generation*, *Scientific Reports* **8** (mar, 2018).

[242] Y.-Q. Fan, H.-L. Wang, J.-J. Gao, Ke-XinLiu, D.-P. Chai, and Y.-J. Zhang, *Applications of Modular Microfluidics Technology*, *Chinese Journal of Analytical Chemistry* **46** (dec, 2018) 1863–1871.

[243] D. Mohanty, J. K. Patnaik, S. Mohanty, S. K. Satpathy, B. S. Das, and S. K. Mishra, *Vascular Clogging, Mononuclear Cell Margination, and Enhanced Vascular Permeability in the Pathogenesis of Human Cerebral Malaria*, *The American Journal of Tropical Medicine and Hygiene* **51** (nov, 1994) 642–647.

[244] T. Ye, H. Shi, N. Phan-Thien, and C. T. Lim, *The key events of thrombus formation: platelet adhesion and aggregation*, *Biomechanics and Modeling in Mechanobiology* **19** (jun, 2020) 943–955.

[245] A. Kia, H. S. Wong, and C. R. Cheeseman, *Clogging in permeable concrete: A review*, *Journal of Environmental Management* **193** (may, 2017) 221–233.

[246] R. Katznelson, *Clogging of groundwater recharge basins by cyanobacterial mats*, *FEMS Microbiology Ecology* **5** (1989), no. 4 231–242.

[247] H. Y. Jeong, S.-C. Jun, J.-Y. Cheon, and M. Park, *A review on clogging mechanisms and managements in aquifer storage and recovery (ASR) applications*, *Geosciences Journal* **22** (aug, 2018) 667–679.

[248] S. Bounoua, S. Tomas, J. Labille, B. Molle, J. Granier, P. Haldenwang, and S. N. Izzati, *Understanding physical clogging in drip irrigation: in situ, in-lab and numerical approaches*, *Irrigation Science* **34** (7, 2016) 327–342.

[249] N. Ait-Mouheb, J. Schillings, J. Al-Muhammad, R. Bendoula, S. Tomas, M. Amielh, and F. Anselmet, *Impact of hydrodynamics on clay particle deposition and biofilm development in a labyrinth-channel dripper*, *Irrigation Science* **37** (1, 2019) 1–10.

[250] V. Kashyap, A. Al-Bayati, S. M. Sajadi, P. Irajizad, S. H. Wang, and H. Ghasemi, *A flexible anti-clogging graphite film for scalable solar desalination by heat localization*, *Journal of Materials Chemistry A* **5** (2017), no. 29 15227–15234.

[251] T. K. Giri, C. Choudhary, Ajazuddin, A. Alexander, H. Badwaik, and D. K. Tripathi, *Prospects of pharmaceuticals and biopharmaceuticals loaded microparticles prepared by double emulsion technique for controlled delivery*, *Saudi Pharmaceutical Journal* **21** (4, 2013) 125–141.

[252] A. C Silva, C. M Lopes, J. MS Lobo, and M. H Amaral, *Delivery systems for biopharmaceuticals. Part I: Nanoparticles and microparticles*, *Current pharmaceutical biotechnology* **16** (2015), no. 11 940–954.

[253] A. Al Harraq and B. Bharti, *Microplastics through the Lens of Colloid Science*, *ACS Environmental Au* (9, 2021) acsenvironau.1c00016.

[254] N. Delouche, A. B. Schofield, and H. Tabuteau, *Dynamics of progressive pore clogging by colloidal aggregates*, *Soft Matter* **16** (2020), no. 43 9899–9907.

[255] N. Delouche, J. van Doorn, T. Kodger, A. Schofield, J. Sprakel, and H. Tabuteau, *The contribution of colloidal aggregates to the clogging dynamics at the pore scale*, *Journal of Membrane Science* **635** (10, 2021) 119509.

[256] M. Souzy, I. Zuriguel, and A. Marin, *Transition from clogging to continuous flow in constricted particle suspensions*, *Physical Review E* **101** (6, 2020) 060901.

[257] C.-P. Hsu, H. E. Baysal, G. Wirenborn, G. Mrtensson, L. Prahl Wittberg, and L. Isa, *Roughness-dependent clogging of particle suspensions flowing into a constriction*, *Soft Matter* **17** (2021) 7252–7259.

[258] C. Bielinski, O. Aouane, J. Harting, and B. Kaoui, *Squeezing multiple soft particles into a constriction: transition to clogging*, *Physical Review E* **104** (2021), no. 6 065101.

[259] B. Dersoir, M. R. de Saint Vincent, M. Abkarian, and H. Tabuteau, *Clogging of a single pore by colloidal particles*, *Microfluidics and Nanofluidics* **19** (oct, 2015) 953–961.

[260] B. Dersoir, A. B. Schofield, and H. Tabuteau, *Clogging transition induced by self filtration in a slit pore*, *Soft matter* **13** (2017), no. 10 2054–2066.

[261] N. Bizmark, J. Schneider, R. D. Priestley, and S. S. Datta, *Multiscale dynamics of colloidal deposition and erosion in porous media*, *Science advances* **6** (2020), no. 46 eabc2530.

[262] R. Jackson and M. Kay, *Use of pulse irrigation for reducing clogging problems in trickle emitters*, *Journal of Agricultural Engineering Research* **37** (may, 1987) 223–227.

[263] A. F. Bichara, *Redevelopment of clogged recharge wells*, *Journal of Irrigation and Drainage Engineering* **114** (1988), no. 2 343–350.

[264] L. Zhang, P. Wu, D. Zhu, and C. Zheng, *Effect of pulsating pressure on labyrinth emitter clogging*, *Irrigation Science* **35** (jul, 2017) 267–274.

[265] A. Kastl, E. Bar-Zeev, M. Spinnler, and T. Sattelmayer, *Impact of pulsating flows on particle deposition in forward osmosis with spacers*, *Journal of Membrane Science* (2021) 119444.

[266] D. Aljuboury, P. Palaniandy, H. Abdul Aziz, and S. Feroz, *Treatment of petroleum wastewater by conventional and new technologies-a review*, *Glob. Nest J* **19** (2017), no. 3 439–452.

[267] J. Hoslett, T. M. Massara, S. Malamis, D. Ahmad, I. van den Boogaert, E. Katsou, B. Ahmad, H. Ghazal, S. Simons, L. Wrobel, *et. al.*, *Surface water filtration using granular media and membranes: A review*, *Science of the Total Environment* **639** (2018) 1268–1282.

[268] S. Hube, M. Eskafi, K. F. Hrafnkelsdóttir, B. Bjarnadóttir, M. Á. Bjarnadóttir, S. Axelsdóttir, and B. Wu, *Direct membrane filtration for wastewater treatment and resource recovery: A review*, *Science of the Total Environment* **710** (2020) 136375.

[269] M. P. Sikka and M. Mondal, *A critical review on cleanroom filtration*, *Research Journal of Textile and Apparel* (2021).

[270] T. P. Trooien, A. Mahbub, and F. R. Lamm, *Filtration and maintenance consideration for SDI systems*, *Kansas State University Agricultural Experiment Stations and Cooperative Extension Service, Manhattan, KS* (1998).

[271] M. R. Goyal, V. K. Chavan, and V. K. Tripathi, *Principles and Management of Clogging in Micro Irrigation*. Apple Academic Press, 2015.

[272] C. Bertelli, S. Courtois, M. Rosikiewicz, P. Piriou, S. Aeby, S. Robert, J.-F. Loret, and G. Greub, *Reduced chlorine in drinking water distribution systems impacts bacterial biodiversity in biofilms*, *Frontiers in microbiology* **9** (2018) 2520.

[273] R. Einav, K. Harussi, and D. Perry, *The footprint of the desalination processes on the environment*, *Desalination* **152** (2003), no. 1 141–154.

[274] K. Drescher, Y. Shen, B. L. Bassler, and H. A. Stone, *Biofilm streamers cause catastrophic disruption of flow with consequences for environmental and medical systems*, *Proceedings of the National Academy of Sciences* **110** (3, 2013) 4345–4350.

[275] N. I. Lebovka, *Aggregation of charged colloidal particles*, *Advances in Polymer Science* **255** (2014) 57–96.

[276] M. Trofa, G. D'Avino, and P. L. Maffettone, *Numerical simulation of clogging in a microchannel with planar contraction*, *Physics of Fluids* **33** (8, 2021) 083320.

[277] J. Schwarze, M. Grunze, M. Karahka, and H. Kreuzer, *Attachment and Detachment of Particles from a Surface under Shear Flow*, *The Journal of Physical Chemistry C* **123** (4, 2019) 8153–8159.

[278] T. Zsirai, P. Buzatu, P. Aerts, and S. Judd, *Efficacy of relaxation, backflushing, chemical cleaning and clogging removal for an immersed hollow fibre membrane bioreactor*, *Water research* **46** (2012), no. 14 4499–4507.

[279] J. Lohaus, F. Stockmeier, P. Surray, J. Lölsberg, and M. Wessling, *What are the microscopic events during membrane backwashing?*, *Journal of Membrane Science* **602** (2020) 117886.

[280] B. Dincau, E. Dressaire, and A. Sauret, *Pulsatile Flow in Microfluidic Systems*, *Small* (oct, 2019) 1904032.

[281] C. M. Cejas, F. Monti, M. Truchet, J.-P. Burnouf, and P. Tabeling, *Particle Deposition Kinetics of Colloidal Suspensions in Microchannels at High Ionic Strength*, *Langmuir* **33** (7, 2017) 6471–6480.

[282] J. Mewis and N. J. Wagner, *Colloidal suspension rheology*. Cambridge university press, 2012.

[283] M. Matsui, N. Murasaki, K. Fujibayashi, Peng You Bao, and Y. Kishimoto, *Electrification of pure water flowing down a trough set up with a resin sheet*, *Journal of Electrostatics* **31** (11, 1993) 1–10.

[284] K. Yatsuzuka, Y. Higashiyama, and K. Asano, *Electrification of polymer surface caused by sliding ultrapure water*, *IEEE Transactions on Industry Applications* **32** (1996), no. 4 825–831.

[285] M. Özdinç Çarpinliolu and M. Yaşar Gündodu, *A critical review on pulsatile pipe flow studies directing towards future research topics*, *Flow Measurement and Instrumentation* **12** (6, 2001) 163–174.

[286] T. Gervais, J. El-Ali, A. Günther, and K. F. Jensen, *Flow-induced deformation of shallow microfluidic channels*, *Lab on a Chip* **6** (2006), no. 4 500–507.

[287] B. S. Hardy, K. Uechi, J. Zhen, and H. P. Kavehpour, *The deformation of flexible pdms microchannels under a pressure driven flow*, *Lab on a Chip* **9** (2009), no. 7 935–938.

[288] Z. Zhang, C. Drapaca, X. Chen, and J. Xu, *Droplet squeezing through a narrow constriction: Minimum impulse and critical velocity*, *Physics of Fluids* **29** (2017), no. 7 072102.

[289] E. Iritani, N. Katagiri, and G. Inagaki, *Compression and expansion properties of filter cake accompanied with step change in applied pressure in membrane filtration*, *Separation and Purification Technology* **198** (6, 2018) 3–9.

[290] M. Houssais, C. Maldarelli, and J. F. Morris, *Athermal sediment creep triggered by porous flow*, *Physical Review Fluids* **6** (2021), no. 1 L012301.